Modeling and Detection of Delaminations in Laminated Plates

by

David Prosper

Licenciado en Ingeniería Mecánica
Escuela Técnica Superior de Ingenieros Industriales de Bilbao, Spain, June 1994
Master of Science in Civil and Environmental Engineering
Massachusetts Institute of Technology, June 1998

SUBMITTED TO THE DEPARTMENT OF CIVIL AND ENVIRONMENTAL ENGINEERING IN PARTIAL FULFILLMENT OF THE REQUIREMENTS FOR THE DEGREE OF

DOCTOR OF PHILOSOPHY IN STRUCTURES AND MATERIALS
AT THE
MASSACHUSETTS INSTITUTE OF TECHNOLOGY
JUNE 2001

Author.....
Department of Civil and Environmental Engineering
May 4, 2001

Certified by.....
Eduardo Kausel
Professor of Civil and Environmental Engineering
Thesis Supervisor

Accepted by.....
Oral Buyukozturk
Chairman
Departmental Committee on Graduate Students

Modeling and Detection of Delaminations in Laminated Plates

by
David Prosper

Submitted to the Department of Civil and Environmental Engineering on May 4, 2001 in partial fulfillment of the requirements for the degree of Doctor of Philosophy in Structures and Materials

Abstract

The main topic of this thesis is the analysis and detection of delaminations in plate-like structural systems, such as concrete walls, large diameter pipes, slabs and decks.

The first three chapters deal primarily with the numerical 2D modeling of delaminated plates. In the first chapter, we present the *Traction Boundary Element Method* (TBEM) that is the tool we use to model scattering of waves by cracks in elastic media. A critical step in the TBEM is the evaluation of integrals with hypersingular kernels; we propose a novel approach to evaluate analytically these integrals for the plane-strain cases (anti-plane and in-plane). Finally, to test the TBEM and the analytical integrals, we study the 2-D scattering of plane waves by a single crack in an unbounded elastic medium; results compare nicely with previous pseudo-analytical solutions.

The second and third chapters deal with the computation of Green's functions (singular solutions) for homogeneous and laminated plates, to be used in combination with the TBEM. In the second chapter, we present some classical modal solutions for anti-plane waves in a homogeneous plate and in two-layer plate, and in-plane waves in a homogeneous plate with mixed boundary conditions. In the third chapter, we present the Thin Layer Method (TLM), which is a powerful numerical tool for the computation of singular solutions in layered plates. Inasmuch the TLM has already been the subject of comprehensive studies, we focus here in its performance to model the near field and stresses for line loads and dipoles; areas of significant interest for the combination of the TLM and the TBEM that have been yet been explored. We carry out convergence analyses of the method for these cases of interest.

The second part of the thesis focuses on the detection of delaminations. The combination of the TBEM and the TLM gives us a powerful tool to predict the response of plates with known properties and delaminations (the so-called forward model). We use this tool to model numerous configurations and study how the size and location of a delamination do affect the response of the plate. The fourth chapter addresses the standard indirect Non Destructive Evaluation techniques, namely the *Impact-echo Method and the Sounding Method*. We carry out parametric analyses for how the size and depth of a delamination affect the frequency response of the plate. We draw conclusions as to the limits of these methods in detecting delaminations and estimating their sizes and locations. In the fifth chapter, we use array-processing techniques, widely used in other areas such as

seismology and telecommunications, to unravel the wave field of delaminated plates. We demonstrate that delaminations have a significant impact in the wave field, and that the decomposition of the propagating field into wave-guide modes can be used for the detection and characterization of delaminations.

In the last chapter, we review the numerical evaluation of wavenumber integrals, and propose a new approach applicable to layered plates.

Thesis Supervisor: Eduardo Kausel
Title: Professor of Civil and Environmental Engineering

Acknowledgements

This dissertation is really the effort of many people whose love, support and faith in me made its completion possible. Special recognition is thus due to them.

First, I would like to thank my advisor Eduardo for all his support and help during all these years; his invaluable advice and guidance were the actual driving force behind my work. His attentions and those of his wife, Cecilia, to my wife, my children and me since our first arrival to MIT are most appreciated; we will always be indebted to them.

My gratitude goes also to all the students, professors and staff that I have met at MIT, especially to my thesis committee and to Cynthia and Jesse, who make our students' life all that much easier.

I am most grateful to Neva and Arnoldo, and Tina and Paul for their most generous attentions to us. Their warm friendship made our years in Boston a most enriching experience, and we shall always remember fondly the wonderful times together. To my many friends at MIT, Mark, Luis, Gonzalo, Joonsang, Abel, Yee Hui and Maw Der, Belen and Pablo, Emma and Abel, Pilar and Larry, Sole and Eduardo, Malena and Rafa, Heidi and Saku, Maite and Adrián, Ines and Miguel, it was my pleasure and privilege to have met you all. I hope that God will give us plenty of opportunities to meet once more in some corner of the world, and to relive the wonderful times we had together in Boston.

I gratefully acknowledge the financial support for my research from the Washington Sanitary Suburban Commission and especially thank John, Paul and Dick, for all that they have taught me while my research was in progress.

I am truly thankful to my parents, brothers and sisters, for their endless love, support and unquestionable faith in me, which proved essential to me during these years. They were always in my thoughts and my heart. I pray that some day I shall be as good a father and a brother as they have been to me.

Last but not least, I owe much praise and gratitude to my wife, Cristina, who unfailingly supported and encouraged me throughout these years. She gave me the strength I needed to carry out my work from beginning to end. Indeed, she always cared for my person and stood behind my efforts, lovingly caring for our children, and not stopping even once to think about herself.

To

my wife Cristina
my children Lola and David
and my parents

I could not have done it
without your love

Table of Contents

Motivation for modeling cracks in laminated media

The analysis of scattering of waves in laminated plates with internal cracks parallel to the layering, also known as delaminations, is of great interest in the application of Non-Destructive-Evaluation (NDE) techniques. The development of delaminations is a frequent pathology in plate-like structural systems such as wall, pipes, decks, slabs and tunnel linings. Such delaminations can grow significantly in size before manifesting themselves on the surface, and thus remain largely invisible from the exterior. These defects can significantly affect the structural performance of the systems in which they arise, and may eventually lead to costly failures. Hence, early detection of incipient defects could result in significant savings in the maintenance of these structures, and can play a key role in the management of such systems.

Proper analysis of laminated plates with cracks, although indispensable to fully understand the dynamic response of these systems, can be a complex and lengthy process. To avoid this complexity, standard NDE techniques rely on very simple models to explain the wave propagation phenomena in plates. As a result, these techniques have a limited ability in detecting structural defects. In addition, most structural assessment entail time-consuming examinations of local conditions, which involve costly and lengthy exploration times.

Given the lack of accurate and reliable forward models, the first part of this thesis focuses on the advanced analysis of delaminations in layered media. In the three chapters that make up the first part of this thesis, we present the tools needed to build a simple, but accurate and efficient, numerical tool for the 2-D modeling of delaminated plates. This type of forward modeling tool can be a valuable aids to the analyst, because it allows assessing the condition of real life structural systems via acoustic NDE techniques.

Chapter 1 :

Scattering of elastic waves by cracks: the Traction Boundary Integral Method

Introduction

The scattering of elastic waves by cracks, voids and inclusions is of interest to several disciplines such as fracture mechanics, seismology and non-destructive evaluation, and has been treated extensively through the years. Of particular interest is the study of interface cracks and delaminations within composite structural systems, such as reinforced fiber and layered plates. For simple geometries and boundary conditions, various analytical solutions have been proposed; for more complicated problems, numerical techniques such as Finite Elements (FEM), Finite Difference (FDM) and Boundary Integral (BIEM) are the only viable ways to evaluate the diffraction of waves. Among these methods, the BIEM presents several clear advantages in the analysis of homogeneous unbounded systems; most significant among these is the implicit treatment of the conditions at infinity (i.e. radiation and boundedness) and the moderate number of degrees of freedom.

Though a crack can be thought of as the limiting state of a flat cavity in which the thickness goes to zero, the conventional direct BIEM degenerates for the flat crack, and is no longer a valid basis for numerical modeling[1]; thus, an alternative formulation is needed. Early modeling approaches to crack problems relied on a replacement of the crack by an *open notch*. This approach is of limited use, however, because while the numerical conditioning improves with crack surface separation, the fidelity with which the crack can be modeled is less than satisfactory. Another early approach is that of *multi-region modeling*, introduced by Lachat[2] and Watson. This method consists in introducing fictitious boundaries to make the conventional BIEM work. This method entails, however, a significant penalty in computational time.

The last two decades have seen much progress in crack research, most of it centered around the concept of the *Traction Boundary Integral Equation Method* (TBIEM). A substantial portion of this research comes from the field of Fracture Mechanics, within which the work of T. A. Cruse stands out as a leading contribution. Indeed, Cruse's papers seem to contain the first attempts at using the TBIEM for crack problems in elastic bodies. Significant contributions were also made in the field of Wave Propagation.

Sládek & Sládek[3,4], and Takakuda[5] are among the first authors to attempt a general formulation of the crack problem focused on the analysis of diffraction of elastic waves. In these works, the former combined the BIE and the Laplace Transform, while the latter developed an integro-differential equation for the steady-state case. Subsequently, Niwa and Hirose[6] formulated the general, steady state diffraction of waves by a crack in a half space by means of Green's functions combined with single and double layer potentials.

Most of the work in the literature of BIEM relies on the so-called *fundamental singular solution* for the infinite space, also known as the *Stokes state*. The rationale behind this choice is that the Stokes functions are fast and easily computed. By contrast, fundamental solutions for other systems, such as half-spaces or plates, are computationally expensive, even if they should be more generally applicable. The choice of the Stokes functions, however, imposes severe limitations on the degree of heterogeneity that systems can exhibit. The reason is that the Stokes functions are based on a homogeneous medium, so all material transitions, including external boundaries, must be discretized with boundary elements. As a result, the number of nodes required (and thus the size of the problem) becomes often intractably large. The current availability of effective analytical expressions for layered systems, such as the Green's functions of Kausel[7] and Kausel & Peek[8] based on the *Thin Layer Method* (TLM), helps circumvent this important limitation and opens new possibilities in the use of BIEM for laminated plates and layered soils.

In this chapter, we develop a BIE for a crack problem starting from the *dynamic reciprocal theorem*, and express the final equation in terms of dipoles *(dynamic doublets)* that lie at the heart of the formulation for layered plates. Thereafter, we use this BIE to analyze the diffraction of plane elastic waves by a plane crack in an unbounded, two-dimensional homogeneous medium. In the chapters that follow, we combine the Green's function based on the Thin Layer Method (TLM) with this BIE, and asses the diffraction of elastic waves in layered plates with cracks.

Integral theorems

Let R be a regular region with boundary B and time interval T. Consider also the displacement vector $\mathbf{u}(\mathbf{x},t)$ and the symmetric, second-order stress tensor $\mathbf{T}(\mathbf{x},t)$, both of which are defined in $R\times T$, such that $\mathbf{u}\in C^{2,2}(R\times T)$. We call the pair $[\mathbf{u},\mathbf{T}]$ an elastodynamic state in $R\times T$, if they satisfy[9]

$$\begin{aligned} t_{lk,l}+\rho f_k &= \rho\ddot{u}_k \\ t_{kl} &= \rho\left(c_P^2-2c_S^2\right)u_{m,m}\delta_{kl}+\rho c_S^2\left(u_{k,l}+u_{l,k}\right) \end{aligned} \tag{1.1}$$

with the displacement and stress fields **u, T** resulting from a body force density **f** acting throughout a body with mass density ρ, dilatational wave speed c_P and shear wave speed c_S. In addition, if $\mathbf{u}=0$ on $R\times T^-$ we call the pair $[\mathbf{u},\mathbf{T}]$ an elastodynamic state with a quiescent past (i.e. an initial value problem, or alternatively, a propagation problem).

The *dynamic reciprocal theorem* states that for *any* two elastodynamic states $[\mathbf{u},\mathbf{T}]$ and $[\mathbf{u}',\mathbf{T}']$ with initial conditions $\mathbf{u}(\mathbf{x},0)=\mathbf{u}_0,\dot{\mathbf{u}}(\mathbf{x},0)=\mathbf{v}_0$ and $\mathbf{u}'(\mathbf{x},0)=\mathbf{u}_0',\dot{\mathbf{u}}'(\mathbf{x},0)=\mathbf{v}_0'$ defined on $R\times T$, the following relationship holds:

$$\int_B \mathbf{t}_\mathbf{n} * \mathbf{u}' ds + \int_R \rho\{\mathbf{f}*\mathbf{u}'+\mathbf{v}_0\mathbf{u}'+\mathbf{u}_0\dot{\mathbf{u}}'\}dv = \int_B \mathbf{t}_\mathbf{n}' * \mathbf{u} ds + \int_R \rho\{\mathbf{f}'*\mathbf{u}+\mathbf{v}_0'\mathbf{u}+\mathbf{u}_0'\dot{\mathbf{u}}\}dv \tag{1.2}$$

The operation * denotes time convolution, $\mathbf{t}_\mathbf{n}=\mathbf{T}\cdot\mathbf{n}$ are the external tractions acting on B, and **n** is the normal vector to the boundary at the integration point. The elastodynamic states $[\mathbf{u},\mathbf{T}]$ and $[\mathbf{u}',\mathbf{T}']$ are often referred to as the *real* (or actual) state and the *virtual* (or imagined, or ideal) state, respectively. It should be understood that these two states are completely independent of one another.

Consider a region R with a single crack whose boundary B consists of the external boundaries of R, B_E, plus the surface delimiting the crack, B_C. We consider as real state the field $[\mathbf{u},\mathbf{T}]$ that results from the actual, applied loads acting on the medium

containing the crack, and as virtual state the fundamental singular solution for R without the crack. We denote the virtual state as $[\mathbf{g},\mathbf{h}]^{(j)}(\mathbf{x},\boldsymbol{\xi})$, which provides the displacements and stresses at an observation station $\mathbf{x}$ due to a unit point load applied at the source location $\boldsymbol{\xi}$ in the direction of x_j. This fundamental solution satisfies both the differential equation and the boundary conditions on B_E. Moreover, we only consider basic Dirichlet-Neumann boundary conditions, that is, either displacements or tractions must vanish at B_E. This assumption simplifies the integral representations by confining the integrals to B_C.

Substitution of these two states into (1.2) yields the integral representation for displacements at any point within R, also known as *Love's Integral Identity*

$$u_k(\boldsymbol{\xi}) = \int_{B_C} \left\{ \mathbf{t}_\mathbf{n} * \mathbf{g}^{(k)} - \mathbf{h}_\mathbf{n}{}^{(k)} * \mathbf{u} \right\} ds + \int_R \rho \mathbf{f} * \mathbf{g}^{(k)} dv + IC \tag{1.3}$$

To transform the integral representation for an interior point into a BIE, we must take the evaluation point $\boldsymbol{\xi}$ to the surface. In the literature on the BIEM, we find several ways of accomplishing this limiting process (for a complete description, see for instance chapter 2 in Paris & Cañas[10]). All of these assume $\mathbf{u}$ to be Hölder-continuous at the boundary point, that is, when $\boldsymbol{\xi} \to \boldsymbol{\xi}_B \mid \boldsymbol{\xi}_B \in B_C$, the following inequality holds:

$$\left|\mathbf{u}(\boldsymbol{\xi}) - \mathbf{u}(\boldsymbol{\xi}_B)\right| \le k \left|\boldsymbol{\xi} - \boldsymbol{\xi}_B\right|^\alpha, \text{ for some constants } k, \alpha > 0 \tag{1.4}$$

This guarantees that $\mathbf{u}$ can be expanded in Taylor series as $\mathbf{u}(\boldsymbol{\xi}) = \mathbf{u}(\boldsymbol{\xi}_B) + O\left(\left|\boldsymbol{\xi} - \boldsymbol{\xi}_B\right|^\alpha\right)$.

The final expression for the standard BIE is

$$\varepsilon(\boldsymbol{\xi}) u_k(\boldsymbol{\xi}) = \int_{B_C} \left\{ \mathbf{t}_\mathbf{n} * \mathbf{g}^{(k)} - \mathbf{h}_\mathbf{n}{}^{(k)} * \mathbf{u} \right\} ds + \int_R \rho \mathbf{f} * \mathbf{g}^{(k)} dv + IC$$

$$\varepsilon(\boldsymbol{\xi}) = \lim_{r \to 0} \int_{S_r} \mathbf{h}_\mathbf{n}{}^{(k)} ds = \begin{cases} 1 & \boldsymbol{\xi} \in R \\ 0.5 & \boldsymbol{\xi} \in B_C \text{ (for } B_C \text{ smooth)} \\ 0 & \boldsymbol{\xi} \notin R \cup B_C \end{cases} \tag{1.5}$$

The coefficient $\varepsilon(\xi)$ on the left that weights the displacement at the singularity depends only on the geometry of B in the vicinity of the evaluation point; for non-smooth boundaries, this coefficient can be computed with either the static or the dynamic solution, because the behavior of both of these at the singularity itself (but not elsewhere) is the same.

We can easily obtain an integral representation for stresses from (1.3) by applying the traction operator[11].

$$t_{kl}(\xi) = \int_{B_C} \left\{ \mathbf{t}_n * \bar{\mathbf{g}} - \bar{\mathbf{h}}_n * \mathbf{u} \right\} ds + \int_R \rho \mathbf{f} * \bar{\mathbf{g}} dv + IC \tag{1.6}$$

Repeating the same limiting process as above, we obtain the BIE for stresses as

$$a(\xi) u_k(\xi) + \varepsilon(\xi) t_{kl}(\xi) = \int_{B_C} \left\{ \mathbf{t}_n * \bar{\mathbf{g}} - \bar{\mathbf{h}}_n * \mathbf{u} \right\} ds + \int_R \rho \mathbf{f} * \bar{\mathbf{g}} dv + IC \tag{1.7}$$

In the above expressions

$$\begin{aligned} \bar{\mathbf{g}} &= \lambda \frac{\partial \mathbf{g}^{(m)}}{\partial \xi_m}(\mathbf{x},\xi)\delta_{kl} + \mu \left[\frac{\partial \mathbf{g}^{(k)}}{\partial \xi_l}(\mathbf{x},\xi) + \frac{\partial \mathbf{g}^{(l)}}{\partial \xi_k}(\mathbf{x},\xi) \right] \\ \bar{\mathbf{h}} &= \lambda \frac{\partial \mathbf{h}^{(m)}}{\partial \xi_m}(\mathbf{x},\xi)\delta_{kl} + \mu \left[\frac{\partial \mathbf{h}^{(k)}}{\partial \xi_l}(\mathbf{x},\xi) + \frac{\partial \mathbf{h}^{(l)}}{\partial \xi_k}(\mathbf{x},\xi) \right] \end{aligned} \tag{1.8}$$

with $\lambda = \rho\left(c_P^2 - 2c_S^2\right)$ and $\mu = \rho c_S^2$ being the *Lame* constants. If the boundary is smooth, $\varepsilon(\xi \in B_C) = 0.5$. The coefficient $a(\xi)$, first noted by Guiggiani[12], depends on the curvature of the boundary; it is zero for piecewise straight (flat) boundaries, but this is not necessarily the case for smoothly curved ones. A more complete description of the limiting process and of the free terms can be found in Guiggiani.

In the analysis of cracks, which correspond to the *second problem of elastodynamics* (i.e. tractions prescribed on the boundary), it is actually the BIE for stresses that is useful.

It is important to note that the integral representation for displacements (1.3) and stresses (1.6) are exact representations of the original problem cast in the form of partial differential equations. No approximations have been made, so solutions to the integral

representations satisfy also the original differential equations[13]. For zero initial conditions, they transform straightforwardly into the Fourier domain, yielding the well-known *Somigliana identity* and the *Somigliana stress identity*, respectively.

BIE for the crack problem

The integral representation for stresses for a body with a flat crack of zero width is given by

$$t_{kl}(\xi) = \int_{B_C^+} \left\{ \mathbf{t}_\mathbf{n} * \bar{\mathbf{g}} - \bar{\mathbf{h}}_\mathbf{n} * \mathbf{u} \right\} ds + \int_{B_C^-} \left\{ \mathbf{t}_\mathbf{n} * \bar{\mathbf{g}} - \bar{\mathbf{h}}_\mathbf{n} * \mathbf{u} \right\} ds + \int_R \rho \mathbf{f} * \bar{\mathbf{g}} dv \tag{1.9}$$

Applying the boundary condition, $\mathbf{t}_\mathbf{n}(x \in B_C) = 0$, we obtain the BIE for the flat crack problem

$$\boxed{-\int_{B_C^+} \bar{\mathbf{h}}_\mathbf{n} * \left\{ \mathbf{u}^+ - \mathbf{u}^- \right\} ds + \int_R \rho \mathbf{f} * \bar{\mathbf{g}} dv = 0} \tag{1.10}$$

Solving from this expression for the jump of displacements at the crack $\left\{ \mathbf{u}^+ - \mathbf{u}^- \right\}$, we can then proceed to compute the total field of displacements with the help of equation (1.3). For zero stress on the surface crack, the displacements are

$$\boxed{u_k(\xi) = \int_{B_C^+} -\mathbf{h}_\mathbf{n}^{(k)} * \left\{ \mathbf{u}^+ - \mathbf{u}^- \right\} ds + \int_R \rho \mathbf{f} * \mathbf{g}^{(k)} dv} \tag{1.11}$$

The volume integrals, can be further transformed into

$$\int_R \rho \mathbf{f} * \mathbf{g}^{(k)} dv = \int_R \rho_\mathbf{x} f_i * g_i^{(k)}(\mathbf{x}, \xi) dv = \int_R \rho_\mathbf{x} f_i * g_k^{(i)}(\xi, \mathbf{x}) dv \tag{1.12}$$

and

$$\begin{aligned} \int_R \rho \mathbf{f} * \bar{\mathbf{g}} dv &= \int_R \rho_\mathbf{x} f_i * \left\{ \lambda_\xi \frac{\partial g_i^{(m)}}{\partial \xi_m}(\mathbf{x}, \xi) \delta_{kl} + \rho_\xi c_{2\xi}^2 \left[\frac{\partial g_i^{(k)}}{\partial \xi_l}(\mathbf{x}, \xi) + \frac{\partial g_i^{(l)}}{\partial \xi_k}(\mathbf{x}, \xi) \right] \right\} dv \\ &= \int_R \rho_\mathbf{x} f_i * \left\{ \lambda_\xi \frac{\partial g_m^{(i)}}{\partial \xi_m}(\xi, \mathbf{x}) \delta_{kl} + \rho_\xi c_{2\xi}^2 \left[\frac{\partial g_k^{(i)}}{\partial \xi_l}(\xi, \mathbf{x}) + \frac{\partial g_l^{(i)}}{\partial \xi_k}(\xi, \mathbf{x}) \right] \right\} dv \\ &= \int_R \rho_\mathbf{x} f_i * t_{kl}^{(i)}(\xi, \mathbf{x}) dv \end{aligned} \tag{1.13}$$

These are, respectively, the incident displacement field and the incident stresses on B_C, $\left[\mathbf{u}^{\mathbf{I}}, \mathbf{t}^{\mathbf{I}}\right]$.

Plane-strain BIE

The solution of wave scattering problems for plane-strain conditions can provide important insights into the far more complex problem in three dimensions, which is the reason we consider them here. In a nutshell, there are two types of plane-strain problems, namely the *anti-plane* case and the *in-plane* case.

In the anti-plane case, there is only one component of displacement and stress that matters and the problem involves only equivoluminal (i.e. shear) waves; the equation parallels that of the scalar (i.e. acoustic) wave problem. With reference to Figure 1-1, we have in this case

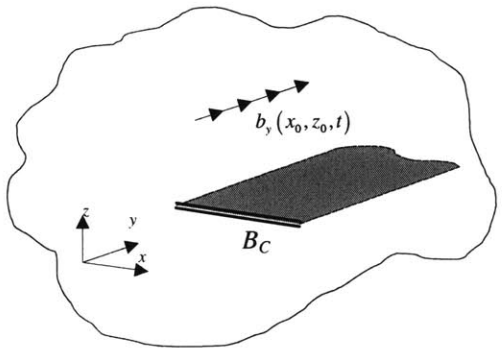

Figure 1-1: Slit of infinite length and finite width subject to anti-plane loads

$$t_{zy}^{\mathbf{I}}(\xi) = \int_{B_C^+} \rho c_2^2 \frac{\partial h_{zy}^{(y)}}{\partial \xi_z}(\mathbf{x}, \xi) * \left\{u_y^+ - u_y^-\right\} dx \tag{1.14}$$

$$u_y(\xi) = u_y^{\mathbf{I}}(\xi) - \int_{B_C^+} h_{zy}^{(y)}(\mathbf{x}, \xi) * \left\{u_y^+ - u_y^-\right\} dx \tag{1.15}$$

By contrast, in the in-plane problem, there exist two components of displacement (particles move within the plane), and there exist three components of stresses that result from both irrotational (P) and equivoluminal (S) waves. Except for very special situations, these two types of waves are fully coupled. In this case, we have

$$
\begin{aligned}
t_{zx}^{\mathbf{I}}(\xi) &= \int_{B_C^+} \rho c_2^2 \left[\frac{\partial h_{zx}^{(z)}}{\partial \xi_x}(\mathbf{x},\xi) + \frac{\partial h_{zx}^{(x)}}{\partial \xi_z}(\mathbf{x},\xi) \right] * \left\{ u_x^+ - u_x^- \right\} dx + \\
&\quad \int_{B_C^+} \rho c_2^2 \left[\frac{\partial h_{zz}^{(z)}}{\partial \xi_x}(\mathbf{x},\xi) + \frac{\partial h_{zz}^{(x)}}{\partial \xi_z}(\mathbf{x},\xi) \right] * \left\{ u_z^+ - u_z^- \right\} dx \\
t_{zz}^{\mathbf{I}}(\xi) &= \int_{B_C^+} \left[\left(\lambda + 2\rho c_2^2\right) \frac{\partial h_{zx}^{(z)}}{\partial \xi_z}(\mathbf{x},\xi) + \lambda \frac{\partial h_{zx}^{(x)}}{\partial \xi_x}(\mathbf{x},\xi) \right] * \left\{ u_x^+ - u_x^- \right\} dx + \\
&\quad \int_{B_C^+} \left[\left(\lambda + 2\rho c_2^2\right) \frac{\partial h_{zz}^{(z)}}{\partial \xi_z}(\mathbf{x},\xi) + \lambda \frac{\partial h_{zz}^{(x)}}{\partial \xi_x}(\mathbf{x},\xi) \right] * \left\{ u_z^+ - u_z^- \right\} dx
\end{aligned}
\tag{1.16}
$$

$$
\begin{aligned}
u_x(\xi) &= u_x^{\mathbf{I}}(\xi) - \int_{B_C^+} \left[h_{zx}^{(x)}(\mathbf{x},\xi) * \left\{ u_x^+ - u_x^- \right\} + h_{zz}^{(x)}(\mathbf{x},\xi) * \left\{ u_z^+ - u_z^- \right\} \right] dx \\
u_z(\xi) &= u_z^{\mathbf{I}}(\xi) - \int_{B_C^+} \left[h_{zx}^{(z)}(\mathbf{x},\xi) * \left\{ u_x^+ - u_x^- \right\} + h_{zz}^{(z)}(\mathbf{x},\xi) * \left\{ u_z^+ - u_z^- \right\} \right] dx
\end{aligned}
\tag{1.17}
$$

Numerical solution of the BIE

When using the Green's functions computed via the TLM, it is possible to solve the BIE in closed form. However, the required integrals are rather involved, which renders their direct evaluation extremely tedious and ineffective. On the other hand, for most other situations, including the case where the *Stokes state* is used, the BIE has no known solution. For this reason, the numerical approach is the most appropriate way to solve the BIE, whatever the fundamental solutions used,

A common strategy consists in discretizing the unknown field variables on the boundary $[\mathbf{u},\mathbf{T}]$ in a fashion that parallels that used for FEM. This process transforms the BIE into an algebraic equation that can easily be solved. The idea is to subdivide the boundary into segments that define the so-called boundary elements (BE). Within each element, a discrete number of nodes are chosen, and it is assumed that the field variables within the element are completely defined by their values at the nodes via appropriate interpolation functions. In the simplest approach, a single node at the centroid of the element is taken and the field variables are assumed to be constant within the element. For more accurate results and faster convergence, linear or quadratic isoparametric elements are more appropriate. In the standard formulation, the nodes can be either all internal to the BE

(discontinuous or non-conforming BE) or some can be shared between elements (edge nodes). The hypersingular integrals in the traction BIEM, however, require C^1 continuity[14], which precludes the use of shared nodes.

The displacements and tractions for any point P within a BE are

$$\begin{aligned} u_i(\mathbf{x}) &= \mathbf{N}(\mathbf{x})\cdot\mathbf{U}_i \\ t_i(\mathbf{x}) &= \mathbf{N}(\mathbf{x})\cdot\mathbf{T}_i \end{aligned} \tag{1.18}$$

In these expressions, $\mathbf{U}_i$ and $\mathbf{T}_i$ are column-vectors containing the displacements and tractions on the nodes of the BE, and $\mathbf{N}$ is a row vector with the interpolation functions used to obtain the field variables at any interior point in the BE from their nodal values. Note that $\mathbf{N}$ depends only on the relative location of the point P to the nodes of the BE.

Considering for simplicity the anti-plane case, substitution of the expansion (1.19) into equations (1.14) and (1.15) gives

$$t^{\mathbf{I}}_{zy}(\xi) = \left[\int_{B_C^+} \rho c_2^2 \frac{\partial h^{(y)}_{zy}}{\partial \xi_z}(\mathbf{x},\xi)\mathbf{N}(\mathbf{x})\,dx \right] * \left\{ \mathbf{U}_y^+ - \mathbf{U}_y^- \right\} \tag{1.20}$$

$$u_y(\xi) = u^{\mathbf{I}}_y(\xi) - \left[\int_{B_C^+} h^{(y)}_{zy}(\mathbf{x},\xi)\mathbf{N}(\mathbf{x},\xi)\,dx \right] * \left\{ \mathbf{U}_y^+ - \mathbf{U}_y^- \right\} \tag{1.21}$$

Applying (1.20) at the N nodes on the boundary of the crack, we obtain a system of N equations with N unknowns $\left\{ \mathbf{U}_y^+ - \mathbf{U}_y^- \right\}$. The discretization process extracts the unknowns from the integrands, so we can evaluate the matrix of coefficients and solve for $\left\{ \mathbf{U}_y^+ - \mathbf{U}_y^- \right\}$.

Griffith crack (2D finite width crack)

So far, we have presented a BIE formulation for the analysis of the diffraction of elastic waves by cracks together with a numerical scheme for solving it. Our final goal is to study the scattering due to cracks in layered plates. Inasmuch as the interpretation of such a complex problem can be difficult, it is desirable to first test the BIE formulation

and the discretization scheme under simpler conditions, such as a crack in an infinite space. Such a test is taken up in this section.

Mal[15] studied analytically the diffraction of waves by a slit of infinite length and finite width in a full space, a problem that is often referred to as a *Griffith crack.* As this problem does not involve any boundaries other than those of the crack, the diffracted field is due to the crack only, so its solution has an easier interpretation than that of a plate.

First, we discuss the issue of the singular integrals that arise in the application of the BIEM. For the standard formulation of the BIE in 2-D, Tadeu[16,17] gives the result of analytical integration for constant, linear and quadratic elements, both for the anti-plane and the in-plane case. Here, we go one step further and present analytical expressions for the integrals involved in modeling a crack with constant elements; these integrals entail one more order of singularity than those in a conventional BIEM.

Fundamental solutions in a full space

The *fundamental singular solutions*, or *Green's functions*, are the basic elements in the application of integral formulation to elastodynamic problems. On the one hand, the analysis of voids and inclusions requires knowledge of the displacements and stresses caused by point loads. On the other, the analysis of crack problems requires the response functions due to dipoles. For this reason, we present below the fundamental solutions required for full homogeneous media.

Harmonic anti-plane (SH) line load in the full space

The displacement field in an elastic, homogeneous infinite medium caused by a unit SH line load that is parallel to the y-axis is

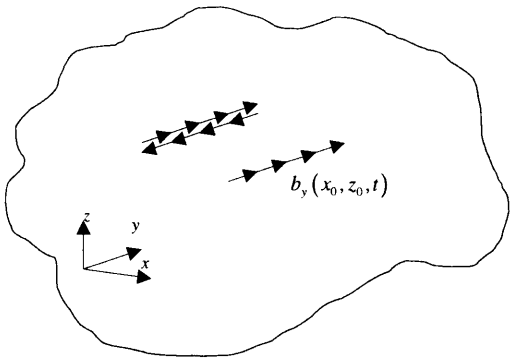

Figure 1-2: Anti-plane line load and dipole

$$\boxed{G_y^{(y)}(r,\omega) = \frac{\mathrm{i}}{4\mu} H_0^{(2)}(k_S r)} \tag{1.22}$$

In this expression, $r = \sqrt{(x-x_0)^2 + (z-z_0)^2}$ is the distance between the source and the receiver, $\mathrm{i} = \sqrt{-1}$, μ is the shear modulus, $k_S = \omega / c_S$ is the S-wavenumber where ω is the angular frequency and $c_S = \sqrt{\mu/\rho}$ is the S-wave velocity, ρ is the mass density and $H_0^{(2)}(\cdot)$ is the second Hankel function of order zero. The need for this kind of Hankel function derives from the positive sign used for the exponential in the temporal Fourier Transform

$$f(t) = \frac{1}{2\pi} \int F(\omega) e^{\mathrm{i}\omega t} d\omega \tag{1.23}$$

Should we have used the negative sign instead, this would have necessitated the use of the first Hankel function, $H_0^{(1)}(\cdot)$.

Differentiating to obtain the strains and applying the medium's constitutive law, we obtain the stresses

$$\boxed{H_{iy}^{(y)} = \tau_{iy}^{(y)} = -\frac{\mathrm{i}k_S}{4} \cos\theta_i H_1^{(2)}(k_S r)} \tag{1.24}$$

where $\cos\theta_i = (x_i - x_{i0})/r \quad (i = x, z)$.

Harmonic in-plane (SV-P) line load in the full space

The displacement field associated with an elastic, homogeneous, infinite medium subjected to a unit in-plane line load contained in the x-z plane, is

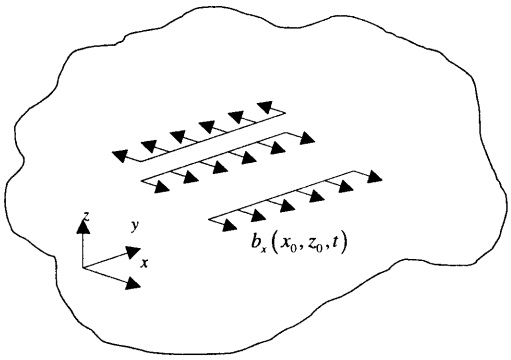

Figure 1-3: In-plane line load and dipole

$$\boxed{G_i^j(r,\omega) = \frac{\mathrm{i}}{4\mu}\left(\psi\delta_{ij} + \chi\cos\theta_i\cos\theta_j\right)} \tag{1.25}$$

$$\boxed{\begin{aligned}\psi &= \frac{1}{k_S r}\left[H_1^{(2)}(k_S r) - \frac{c_S}{c_P}H_1^{(2)}(k_P r)\right] - H_0^{(2)}(k_S r)\\ \chi &= \left(\frac{c_S}{c_P}\right)^2 H_2^{(2)}(k_P r) - H_2^{(2)}(k_S r)\end{aligned}} \tag{1.26}$$

The super-index j indicates the direction of the load, $(j = x, z)$, $c_P = c_S\sqrt{2(1-\nu)/(1-2\nu)}$ is the P-wave velocity, ν is Poisson's ratio, $k_P = \omega/c_P$ the P-wavenumber and the remaining symbols are as defined above.

Differentiation of equation (1.25) gives the strain field

$$\begin{aligned}\varepsilon_{ik}^{(j)} &= \frac{1}{2}\left\{G_{i,k}^{(j)} + G_{k,i}^{(j)}\right\}\\ &= \frac{\mathrm{i}}{4\mu}\left\{\begin{aligned}&\frac{1}{2}\frac{\partial\psi}{\partial r}\left[\delta_{ij}\cos\theta_k + \delta_{kj}\cos\theta_i\right] + \left[\frac{\partial\chi}{\partial r} - 2\frac{\chi}{r}\right]\cos\theta_i\cos\theta_j\cos\theta_k\\ &+\frac{\chi}{r}\left[\delta_{ik}\cos\theta_j + \frac{1}{2}\left(\delta_{jk}\cos\theta_i + \delta_{ji}\cos\theta_k\right)\right]\end{aligned}\right\}\end{aligned} \tag{1.27}$$

Defining

$$\chi_n(r) = k_S^{n-2}\left[\left(\frac{c_S}{c_P}\right)^n H_n^{(2)}(k_P r) - H_n^{(2)}(k_S r)\right] \tag{1.28}$$

and noting that

$$\begin{aligned} \chi &= \chi_2 \\ \frac{\partial \psi}{\partial r} &= \frac{\chi_2}{r} + k_S H_1^{(2)}(k_S r) \\ \frac{\partial \chi_2}{\partial r} &= 2\frac{\chi_2}{r} - \chi_3 \end{aligned} \tag{1.29}$$

we can rewrite equation (1.27) in the more compact form

$$\boxed{\varepsilon_{ik}^{(j)} = \frac{\mathrm{i}}{4\mu}\left\{\begin{array}{l} -\chi_3 \cos\theta_i \cos\theta_j \cos\theta_k + \dfrac{\chi_2}{r}\left[\delta_{ik}\cos\theta_j + \delta_{jk}\cos\theta_i + \delta_{ij}\cos\theta_k\right] \\ \dfrac{1}{2}\left[k_S H_1^{(2)}(k_S r)\right]\left[\delta_{ij}\cos\theta_k + \delta_{kj}\cos\theta_i\right] \end{array}\right\}} \tag{1.30}$$

Application of the constitutive law gives the stresses

$$\boxed{H_{ik}^{(j)} = \tau_{ik}^{(j)} = \lambda\varepsilon_{mm}^{(j)}\delta_{il} + 2\mu\varepsilon_{ik}^{(j)} = \rho\left(c_P^2 - 2c_S^2\right)\varepsilon_{mm}^{(j)}\delta_{ik} + 2\rho c_S^2\varepsilon_{ik}^{(j)}} \tag{1.31}$$

where

$$\boxed{\varepsilon_{mm}^{(j)} = \varepsilon_{xx}^{(j)} + \varepsilon_{zz}^{(j)} = \frac{\mathrm{i}}{4\mu}\left\{-\chi_3 + 4\frac{\chi_2}{r} + k_S H_1^{(2)}(k_S r)\right\}\cos\theta_j} \tag{1.32}$$

Green's function for line dipoles

The *Green's function* for a dipole, also referred to as *dynamic doublet*, may easily be obtained from the singular load case[18]. Let $\mathbf{g}(\mathbf{r},\mathbf{r}_0)$ be the Green's function for a line load applied at $\mathbf{r}_0$, and consider two loads of equal magnitude P and opposite direction at some small distance $2a$ apart. Define **a** to be the vector connecting the point midway between the two loads to one of these. These forces cause a displacement field

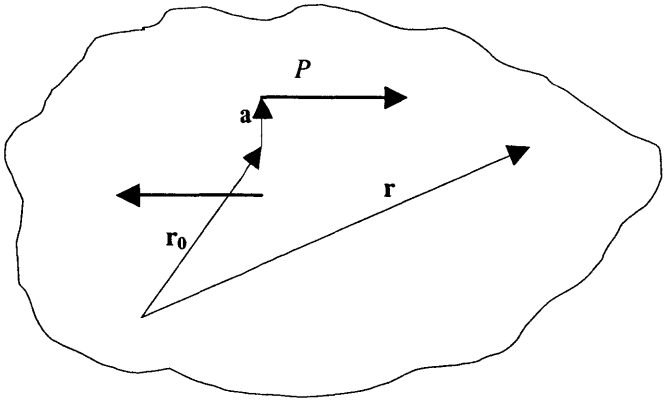

Figure 1-4: Dynamic doublet or dipole

$$\mathbf{u} = P\left[\mathbf{g}(\mathbf{r},\mathbf{r}_0+\mathbf{a})-\mathbf{g}(\mathbf{r},\mathbf{r}_0-\mathbf{a})\right] \tag{1.33}$$

The expansion in Taylor series of the Green's function is

$$\mathbf{g}(\mathbf{r},\mathbf{r}_0\pm\mathbf{a}) = \mathbf{g}(\mathbf{r},\mathbf{r}_0)\pm\mathbf{a}\nabla_0\mathbf{g}+O\left(a^2\right) \tag{1.34}$$

In this expression, the sub-index in the gradient operator highlights the fact that it entails differentiation with respect to the dipole position, and not the field point. Substituting this expansion into equation (1.33) and defining the strength M of the dipole $M = 2Pa$, we obtain in the limit $a \to 0$

$$\mathbf{u} = M\hat{\mathbf{a}}\nabla_0\mathbf{g} \tag{1.35}$$

This final expression constitutes the Green's functions for line dipoles in a full space.

Harmonic anti-plane (SH) line dipole in the full space

The Green's function for the full space depends only on the relative position to the load, not its absolute position. Thus, differentiation with respect to the load position equals the negative of differentiation with respect to the field point. Bearing this in mind, the Green's function for an SH line dipole in the full space may be obtained as

$$\mathbf{u} = \hat{\mathbf{a}}\cdot\nabla\mathbf{g}_0 = -\hat{\mathbf{a}}\cdot\nabla\mathbf{g} \tag{1.36}$$

Expanding equation (1.36), the displacement field due to a dipole with axis parallel to x_k is

$$\boxed{u_y^{(y)k} = -G_{y,k}^{(y)} = \frac{ik_S}{4\mu}\cos\theta_k H_1^{(2)}(k_S r)} \tag{1.37}$$

The stresses are

$$\boxed{H_{iy}^{(y)k} = \tau_{iy}^{(y)k} = \frac{ik_S}{4}\left\{\delta_{ik}\frac{H_1^{(2)}(k_S r)}{r} - k_S\cos\theta_i\cos\theta_k H_2^{(2)}(k_S r)\right\}} \tag{1.38}$$

Harmonic in-plane (SV-P) line dipole in the full space

From equation (1.36), the displacements in the direction "x_i" due to a dipole with forces parallel to "x_j" and axis parallel to "x_k" are

$$u_i^{(j)k} = -G_{i,k}^{(j)} = -\frac{i}{4\mu}\left\{\begin{array}{l}\cos\theta_k\left[\delta_{ij}\dfrac{\partial\psi}{\partial r} + \dfrac{\partial\chi}{\partial r}\cos\theta_i\cos\theta_j - 2\dfrac{\chi}{r}\cos\theta_i\cos\theta_j\right] \\ +\dfrac{\chi}{r}\left[\delta_{ik}\cos\theta_j + \delta_{jk}\cos\theta_i\right]\end{array}\right\} \tag{1.39}$$

Substitution of equations (1.28) and (1.29) into (1.39) gives the more compact expression

$$\boxed{u_i^{(j)k} = \frac{i}{4\mu}\left\{\begin{array}{l}\chi_3\cos\theta_i\cos\theta_j\cos\theta_k - \delta_{ij}\cos\theta_k k_S H_1^{(2)}(k_S r) \\ -\dfrac{\chi_2}{r}\left[\delta_{ij}\cos\theta_k + \delta_{ik}\cos\theta_j + \delta_{jk}\cos\theta_i\right]\end{array}\right\}} \tag{1.40}$$

Differentiation of the dipole *Green's function* gives

$$u_{i,l}^{(j)k} = -\frac{i}{4\mu}\left\{\begin{array}{l}\chi_4\cos\theta_i\cos\theta_j\cos\theta_k\cos\theta_l + \dfrac{\chi_2}{r^2}\left[\delta_{ij}\delta_{kl} + \delta_{ik}\delta_{jl} + \delta_{il}\delta_{jk}\right] \\ -\dfrac{\chi_3}{r}\left[\begin{array}{l}\delta_{ij}\cos\theta_k\cos\theta_l + \delta_{ik}\cos\theta_j\cos\theta_l + \delta_{il}\cos\theta_j\cos\theta_k \\ +\delta_{jk}\cos\theta_i\cos\theta_l + \delta_{jl}\cos\theta_i\cos\theta_k + \delta_{kl}\cos\theta_i\cos\theta_j\end{array}\right] \\ -k_S^2 H_2^{(2)}(k_S r)\delta_{ij}\cos\theta_k\cos\theta_l + k_S\dfrac{H_1^{(2)}(k_S r)}{r}\delta_{ij}\delta_{kl}\end{array}\right\} \tag{1.41}$$

From here, strains are easily computed as

$$\boxed{\begin{aligned}\varepsilon_{il}^{(j)k} &= \frac{1}{2}\left\{u_{i,l}^{(j)k} + u_{l,i}^{(j)k}\right\} \\ &= -\frac{\mathrm{i}}{4\mu}\left\{\begin{array}{l}\chi_4 \cos\theta_i \cos\theta_j \cos\theta_k \cos\theta_l + \dfrac{\chi_2}{r^2}\left[\delta_{ij}\delta_{kl} + \delta_{ik}\delta_{jl} + \delta_{il}\delta_{jk}\right] \\ -\dfrac{\chi_3}{r}\left[\begin{array}{l}\delta_{ij}\cos\theta_k\cos\theta_l + \delta_{ik}\cos\theta_j\cos\theta_l + \delta_{il}\cos\theta_j\cos\theta_k \\ +\delta_{jk}\cos\theta_i\cos\theta_l + \delta_{jl}\cos\theta_i\cos\theta_k + \delta_{kl}\cos\theta_i\cos\theta_j\end{array}\right] \\ -\dfrac{1}{2}k_S^2 H_2^{(2)}\left(k_S r\right)\left[\delta_{ij}\cos\theta_k\cos\theta_l + \delta_{lj}\cos\theta_k\cos\theta_i\right] \\ +\dfrac{1}{2}k_S\dfrac{H_1^{(2)}\left(k_S r\right)}{r}\left[\delta_{ij}\delta_{kl} + \delta_{lj}\delta_{ki}\right]\end{array}\right\}\end{aligned}} \tag{1.42}$$

Finally, the stresses are given by

$$\boxed{H_{il}^{(j)k} = \tau_{il}^{(j)k} = \lambda\varepsilon_{mm}^{(j)k}\delta_{il} + 2\mu\varepsilon_{il}^{(j)k} = \rho\left(c_P^2 - 2c_S^2\right)\varepsilon_{mm}^{(j)k}\delta_{il} + 2\rho c_S^2\varepsilon_{il}^{(j)k}} \tag{1.43}$$

where

$$\boxed{\varepsilon_{mm}^{(j)k} = -\frac{\mathrm{i}}{4\mu}\left\{\cos\theta_j\cos\theta_k\left[\chi_4 - 6\frac{\chi_3}{r} - k_S^2 H_2^{(2)}\left(k_S r\right)\right] - \delta_{jk}\left[\frac{\chi_3}{r} - 4\frac{\chi_2}{r^2} - k_S\frac{1}{r}H_1^{(2)}\left(k_S r\right)\right]\right\}} \tag{1.44}$$

Analytical evaluation of the Singular Integrals

The next step is to evaluate the integrals of the fundamental solutions weighted by the interpolation functions, as shown in equation (1.20). These integrals provide the matrix of coefficients that are needed to solve for the jump (i.e. discontinuity) in displacements at the crack.

When the integral extends along an element other than the loaded element so that the integrand does not contain a singularity, numerical quadrature is the simplest and easiest way to go. In this work, we shall use a five-point Gauss-Legendre rule whenever numerical quadrature is called for.

For the loaded element, however, the integrand becomes infinite at the point of application of the load, at which point the integral is singular, although it is still integrable. Indeed, the existence of a singular integral depends on the behavior of the integrand in the neighborhood of the singular point. In particular, since the right hand side of the integral representation given in equation (1.10) is a finite physical quantity, the boundary integrals on the left should be finite too. That is, it can be argued on physical grounds that the limit of the integral representation must exist.

In the system of equations to solve, the diagonal terms that correspond to the singular integrals are dominant; thus, the accuracy of the BIE solution depends strongly on an accurate evaluation of these terms. Tadeu [16,17] gives closed-form solutions for the singular integrals that appear in the standard 2D BIE, namely the ones derived from the *Somigliana identity*, for constant, linear or quadratic BE. In this work, we present closed-form solutions for the singular integrals involved in the 2D BIE crack problem with constant elements, whose integrands involve one more order of singularity that those in Tadeu's work.

Singular Integrals for the Anti-plane case

For a constant BE contained in the *x*-*y* plane, the integrals in equation (1.21) and (1.20) becomes

$$I_1 = \int_{-L/2}^{L/2} H_{zy}^{(y)} dx = -\frac{ik_S}{4} \int_{-L/2}^{L/2} \cos\theta_Z H_1^{(2)}(k_S r)\, dx$$
$$I_2 = \int_{-L/2}^{L/2} H_{zy}^{(y)z} dx = \frac{ik_S}{4} \int_{-L/2}^{L/2} \left\{ \frac{H_1^{(2)}(k_S r)}{r} - k_S \cos\theta_Z^2 H_2^{(2)}(k_S r) \right\} dx \tag{1.45}$$

For a loaded BE, the first integrand at the origin is undetermined, while the second integrand is the sum of a singular term plus an undetermined one. Thus, to evaluate these integrals, we proceed indirectly by isolating a semi-cylinder just above the BE and considering its dynamic equilibrium.

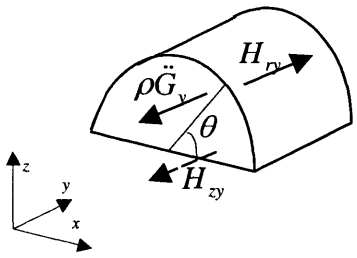

Figure 1-5: Dynamic equilibrium on top of load

$$\int_{S_{BE}} H_{zy} dS = \int_{S_R} H_{ry} dS - \int_V \rho \ddot{G}_y dV \tag{1.46}$$

Both integrands to the right of the equal sign in equation (1.46) are well behaved, and can be evaluated directly.

For the line load, we have

$$\begin{aligned}
\iiint_V \rho\ddot{G}_y dV &= -\rho\omega^2 \int_0^{\pi}\int_0^{L/2} G_y r dr d\theta = -\rho\omega^2 \frac{\mathrm{i}}{4\mu} \int_0^{L/2} H_0^{(2)}(k_S r) r dr \int_0^{\pi} d\theta \\
&= \frac{\mathrm{i}\pi}{4}\left[2\mathrm{i}/\pi - (k_S L/2) H_1^{(2)}(k_S L/2)\right] \\
\int_{S_R} H_{ry} dS &= \mu \int_0^{\pi} (L/2) \frac{\partial G_y}{\partial r} d\theta = -\frac{\mathrm{i}}{4} \int_0^{\pi} (k_S L/2) H_1^{(2)}(k_S L/2) d\theta \\
&= -\frac{\mathrm{i}\pi}{4} (k_S L/2) H_1^{(2)}(k_S L/2)
\end{aligned} \tag{1.47}$$

while for the dipole

$$\begin{aligned}
\iiint_V \rho\ddot{G}_y dV &= -\rho\omega^2 \int_0^{\pi}\int_0^{L/2} G_y r dr d\theta = -\rho\omega^2 \frac{\mathrm{i}k_S}{4\mu} \int_0^{L/2} H_1^{(2)}(k_S r) r dr \int_0^{\pi} \sin\theta d\theta \\
&= \frac{\mathrm{i}k_S^2}{2}\left[(L/2) H_0^{(2)}(k_S L/2) - \int_0^{L/2} H_0^{(2)}(k_S r) dr\right] \\
\int_{S_R} H_{ry} dS &= \mu \int_0^{\pi} (L/2) \frac{\partial G_y}{\partial r} d\theta = \frac{\mathrm{i}}{4} \int_0^{\pi} (k_S L/2) \left.\frac{\partial H_1^{(2)}(k_S r)}{\partial r}\right|_{r=L/2} \sin\theta d\theta \\
&= \frac{\mathrm{i}k_S^2}{2}\left[(L/2) H_0^{(2)}(k_S L/2) - H_1^{(2)}(k_S L/2)/k_S\right]
\end{aligned} \tag{1.48}$$

Substituting into (1.46), we finally have

$$\boxed{\begin{aligned} I_1 &= \frac{1}{2} \\ I_2 &= \frac{ik_S^2}{2}\left[\int_0^{L/2} H_0^{(2)}(k_S r)\,dr - H_1^{(2)}(k_S L/2)/k_S\right] \end{aligned}} \tag{1.49}$$

The integral $\int_0^{L/2} H_0^{(2)}(k_S r)\,dr$ follows directly from Abramowitz[19]

$$\begin{aligned} \int_0^{L/2} H_0^{(2)}(k_S r)\,dr &= \frac{1}{k_S}\int_0^{k_S L/2} H_0^{(2)}(\xi)\,d\xi \\ &= \frac{L}{2}H_0^{(2)}(k_S r) + \frac{\pi L}{4}\left[H_1^{(2)}(k_S r)S_0(k_S r) - H_0^{(2)}(k_S r)S_1(k_S r)\right] \end{aligned} \tag{1.50}$$

in which S_0 and S_1 are *Struve* functions.

Singular Integrals for the in-plane case

To evaluate the singular integrals for the in-plane case, we use the same indirect approach described above. Below we show the final results for the integrals corresponding to line dipoles. For line loads, the result is trivial, being equal to ½ or 0 depending on whether the load acts in the same direction as the stress or perpendicular to it.

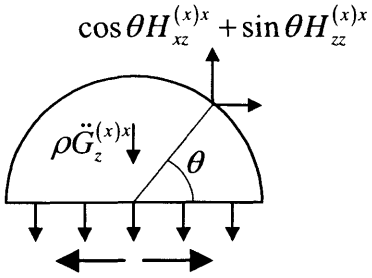

$$\int_{S_{BE}} H_{zx}^{(x)x} dS = 0$$

$$\int_{S_{BE}} H_{zz}^{(x)x} dS = -\frac{i}{2}\left\{\frac{4}{L}\chi_2\left(\frac{L}{2}\right)+\left[1-2\frac{c_S^2}{c_P^2}\right]k_P H_1^{(2)}\left(k_p L/2\right)\right\}$$

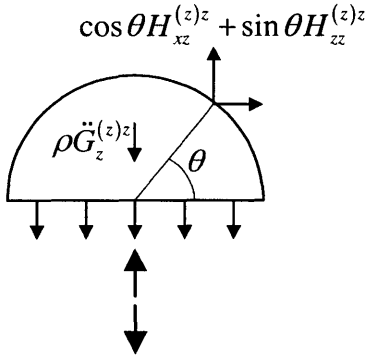

$$\int_{S_{BE}} H_{zx}^{(z)z} dS = 0$$

$$\int_{S_{BE}} H_{zz}^{(z)z} dS = \frac{i}{2}\left\{\begin{array}{l}\frac{4}{L}\chi_2\left(\frac{L}{2}\right)+k_P H_1^{(2)}\left(k_p L/2\right)\\ -k_P^2\int_0^{L/2} H_0^{(2)}\left(k_P r\right)dr\end{array}\right\}$$

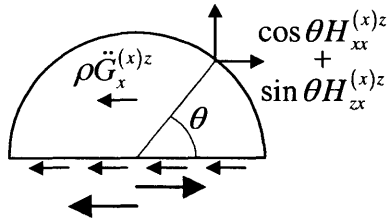

$$\int_{S_{BE}} H_{zx}^{(x)z} dS = -\frac{i}{2}\left\{\begin{array}{l}\frac{4}{L}\chi_2\left(\frac{L}{2}\right)-k_S H_1^{(2)}\left(k_S L/2\right)\\ +k_S^2\int_0^{L/2} H_0^{(2)}\left(k_S r\right)dr\end{array}\right\}$$

$$\int_{S_{BE}} H_{zz}^{(x)z} dS = 0$$

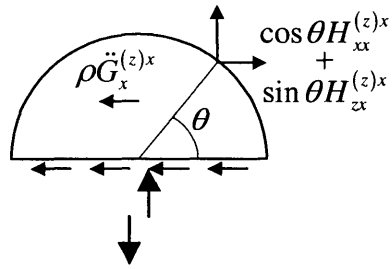

$$\int_{S_{BE}} H_{zx}^{(z)x} dS = -\frac{i}{2}\left\{\frac{4}{L}\chi_2\left(\frac{L}{2}\right)+k_S H_1^{(2)}\left(k_S L/2\right)\right\}$$

$$\int_{S_{BE}} H_{zz}^{(z)x} dS = 0$$

Results

Next, we present some results for the 2D analysis of the diffraction of plane waves by a single crack in an unbounded homogeneous medium.

The first group of figures (Figure 1-6 to Figure 1-10) gives the absolute value of the jump of displacements between opposite surfaces of the crack, often called the Crack Opening Displacement (COD), for incident harmonic plane waves at various angles as a function of the distance to the center of the crack. We consider separately anti-plane and dilatational incident fields. For all cases, the crack extends between $x = \pm 1$ for a total width of two, and the CODs are normalized by the static COD at the center of the crack. Therefore, the curves represent how much the dynamic response differs from the static one. We use a Poisson's ratio of 0.25 for the in-plane problem.

The curves on these figures include results for shear wavelengths that range from half to almost four times the width of the crack (shear wavenumbers from 6 to 0.8). The dynamic response grows initially with the frequency, to reach maximum values for wavelengths of the order of three or four times the crack length, and then decreases rapidly to levels below the static response. We include results for two different discretizations, and show that the coarse discretization of 25 BE compares very well with a fine discretization of 320 BE.

Figure 1-6 and Figure 1-7 correspond to the case of perpendicular incidence, and the response is symmetric with respect to the center of the crack. Our results compare well with those presented by Mal[15] (Figure 3 and 4 in Mal's paper), even for the coarse discretization. Figure 1-8 to Figure 1-10 show how the angle of incidence causes a redistribution of maximum CODs towards the crack end that is further from the incident field.

The second group of figures (Figure 1-11 to Figure 1-15) shows snapshots from numerical simulations of transient plane waves impinging on a flat crack. We consider waves propagating in an elastic medium with shear speed of 2.0 m/ms and Poisson's ratio of 0.25, incident on a single crack 0.2 m wide at 90° (normal incidence), 45° and 0°.

We apply the TBEM in the frequency domain and use the *Exponential Window Method*[20] to transform the solution to the time domain. For this purpose, we consider 513 frequencies, a frequency step of 0.2 kHz and a imaginary component of frequency of 0.15 kHz.

The time shape of the incident wave is that of a *Ricker* wavelet in all cases. This curve presents a main positive lobe in between of two minor negatives lobes and its definition in the frequency domain is

$$R(\omega) = 2At_0\sqrt{\pi}\left(0.5\omega t_0\right)^2 e^{-(0.5\omega t_0)^2} e^{-i\omega t_S} \tag{1.51}$$

where A is the amplitude, πt_0 is the characteristic (dominant) period of the Ricker wavelet and t_S is the time at which the wavelet takes its maximum value.

Figure 1-11 and Figure 1-12 show the scattering for anti-plane waves incident at 90° and 45°; an anti-plane wave traveling parallel to the crack (incidence at 0°) is not scattered by the crack. We choose a 3D representation to better show the motion of the particles, that is perpendicular to the plane containing the points were the outputs are computed, and the opening of the crack.

In these figures, we can clearly see the crack opening at the arrival of the wave, how the energy is reflected back and how, soon after surpassing the crack, the gap in the wave front starts to fill again. After the incident wave has passed, some energy is trapped in the crack, in the form of small waves propagating from end to end of it.

Figure 1-13 to Figure 1-15 show the scattering of a dilatational plane wave. In these cases, there are two components of motion and we present 2D representation showing the actual particles displaced from their equilibrium position. The actual motion is scaled so that it can be seen easily. In addition, the color of the particles lightens with distance to their respective equilibrium positions.

Because of coupling of distortional and dilatational waves at free surfaces, dilatational waves traveling parallel to the crack are scattered in the form of distortional waves propagating at angle (Figure 1-15).

In addition to the energy reflection and the crack opening, we can observe in all this three figures the conversion of part of the dilatational wave into distorsional waves at the free surface of the crack. After the incident wave surpass the crack, the converted energy appears as waves traveling at a slower velocity.

In all the analyses, we use elements with a single node at their center point (constant BE).

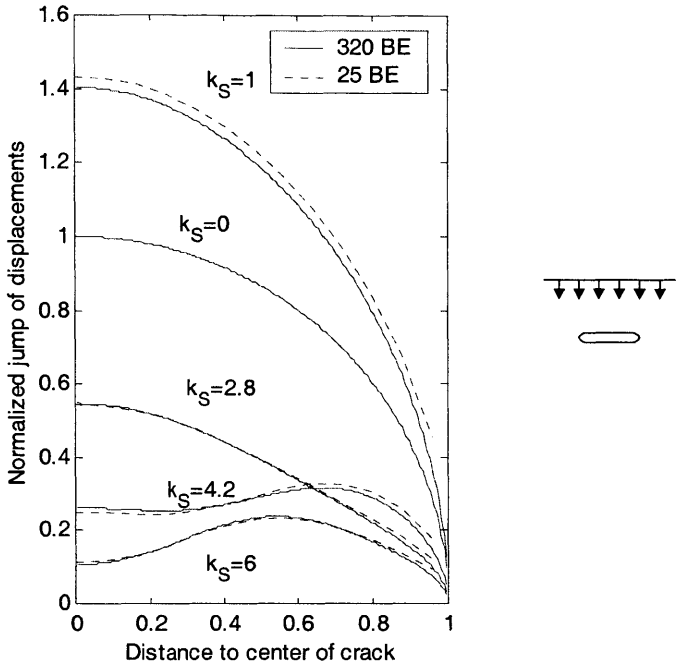

Figure 1-6: Jump of displacements at crack for SH plane wave incident at 90°

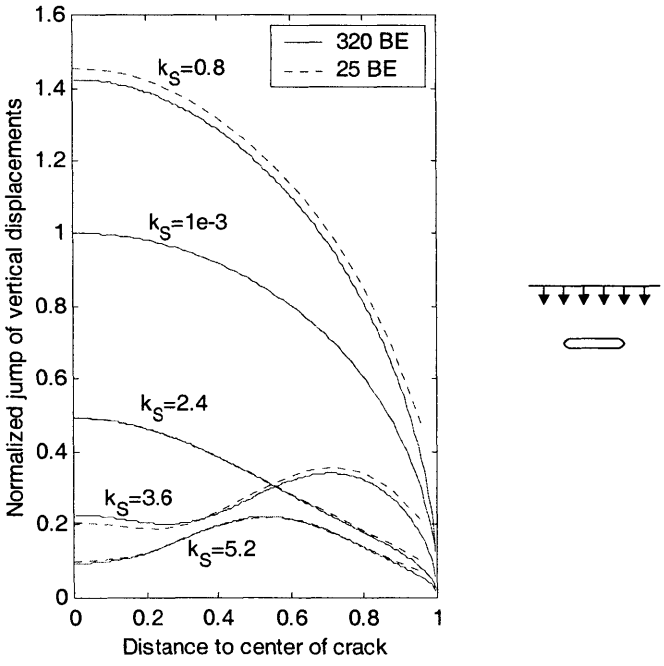

Figure 1-7: Jump of vertical displacements at crack for P plane wave incident at 90°

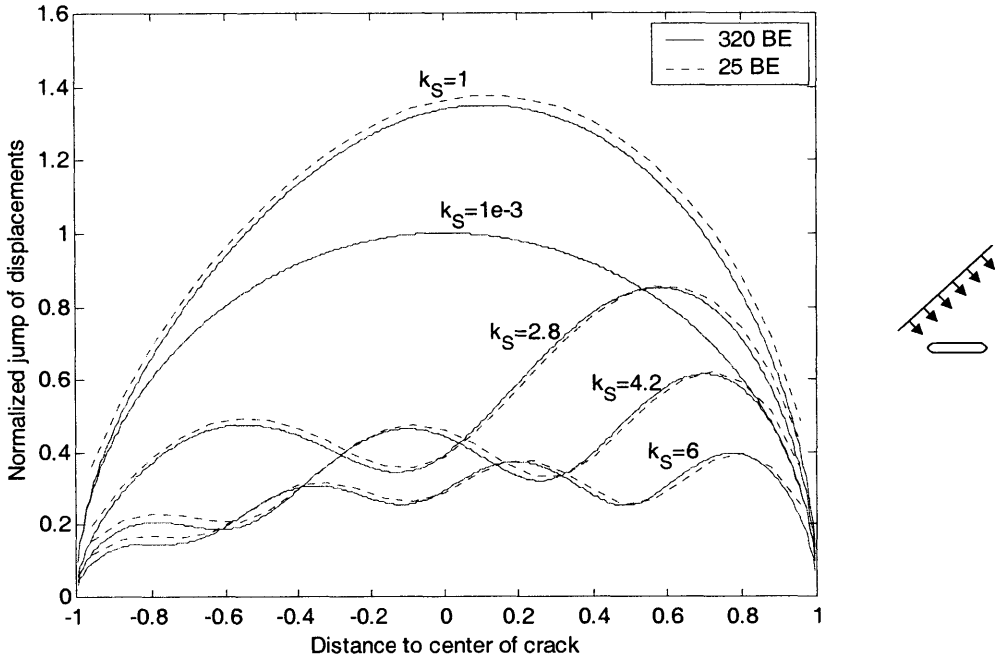

Figure 1-8: Jump of displacements at crack for SH plane wave incident at 45°

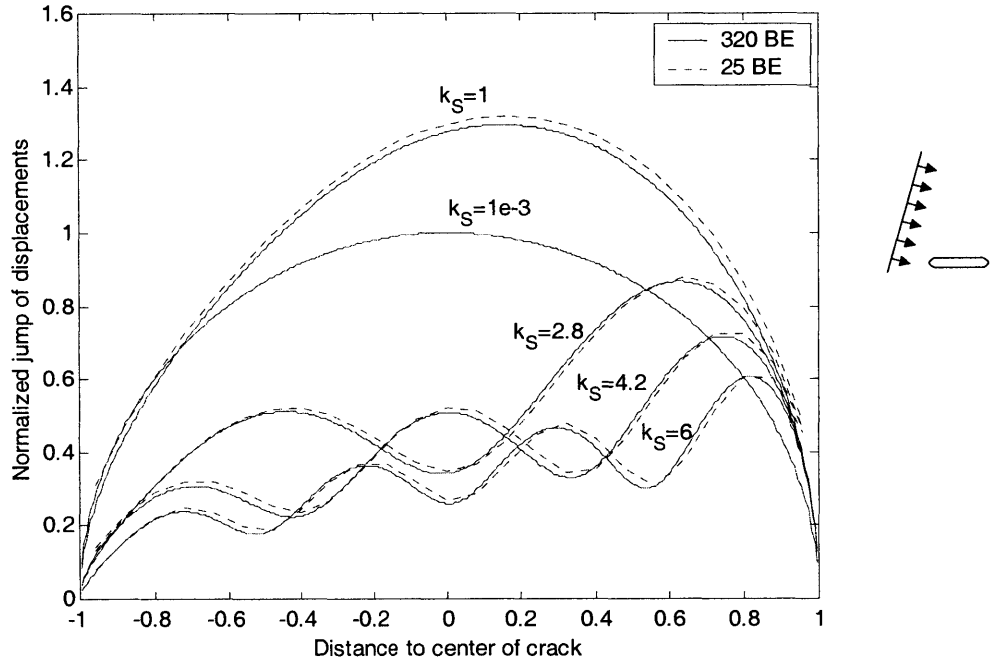

Figure 1-9: Jump of displacements at crack for SH plane wave incident at 5°

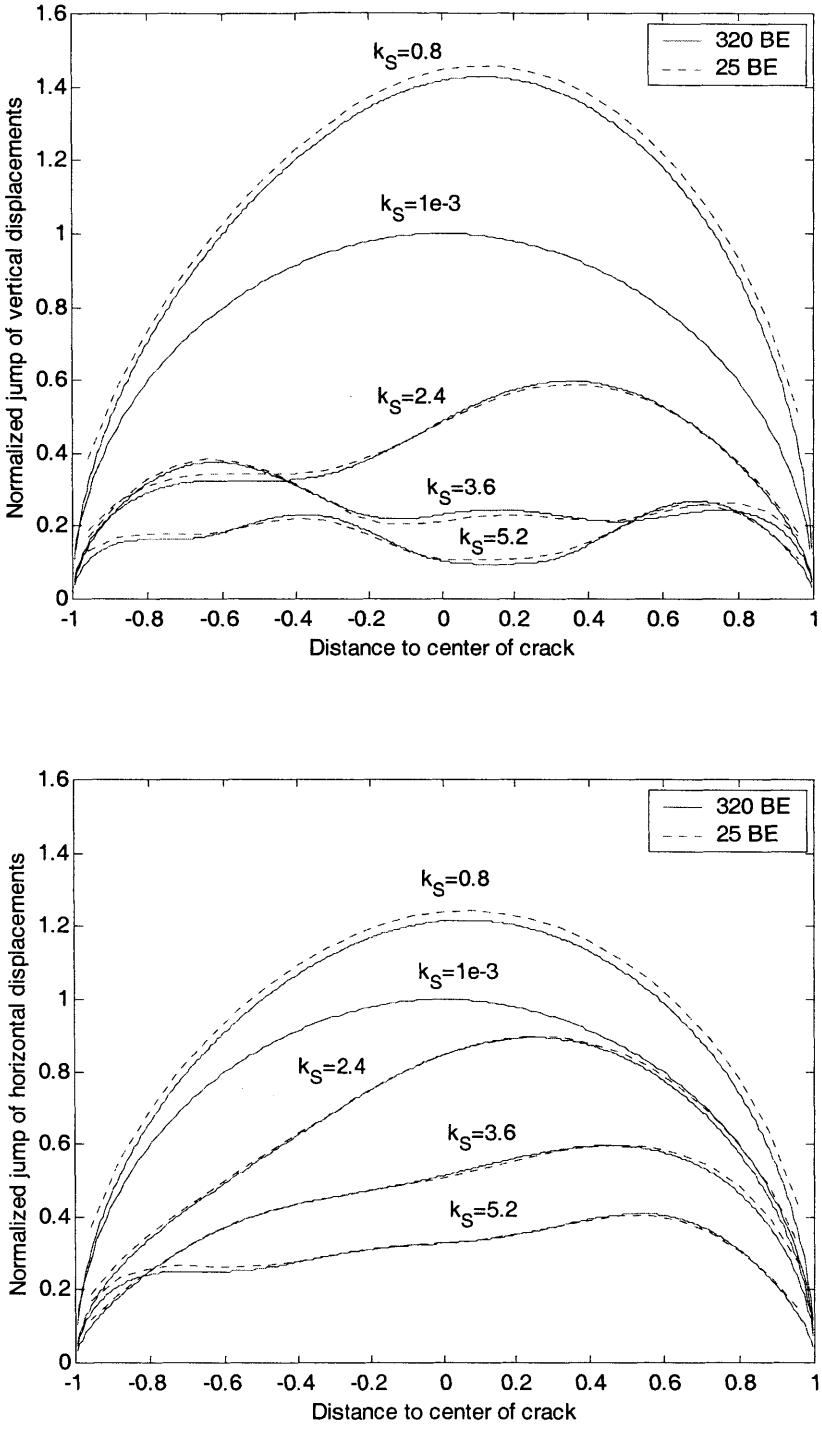

Figure 1-10: Jump of displacements at crack for P plane wave incident at 45°

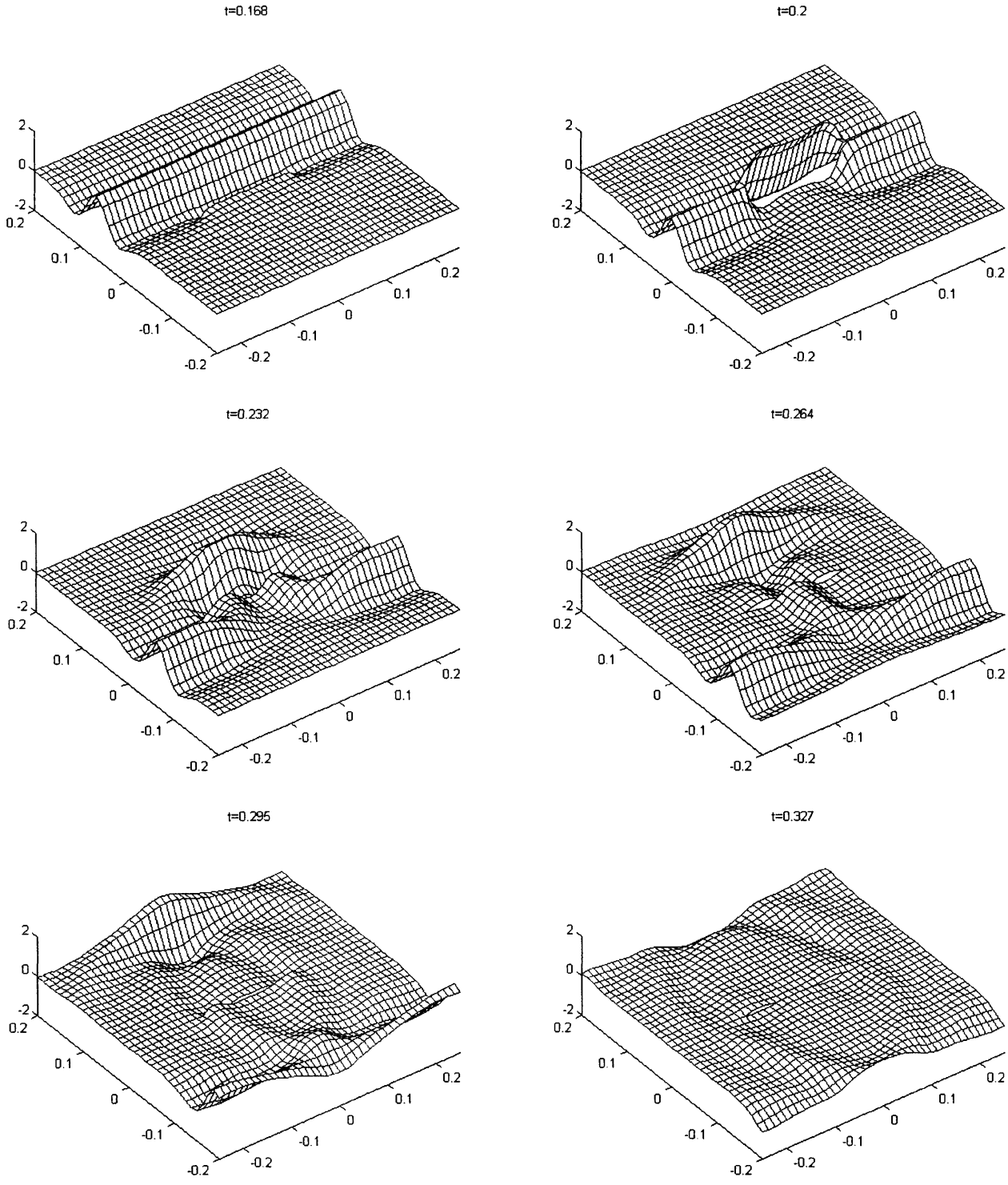

Figure 1-11: SH plane wave incident at 90°

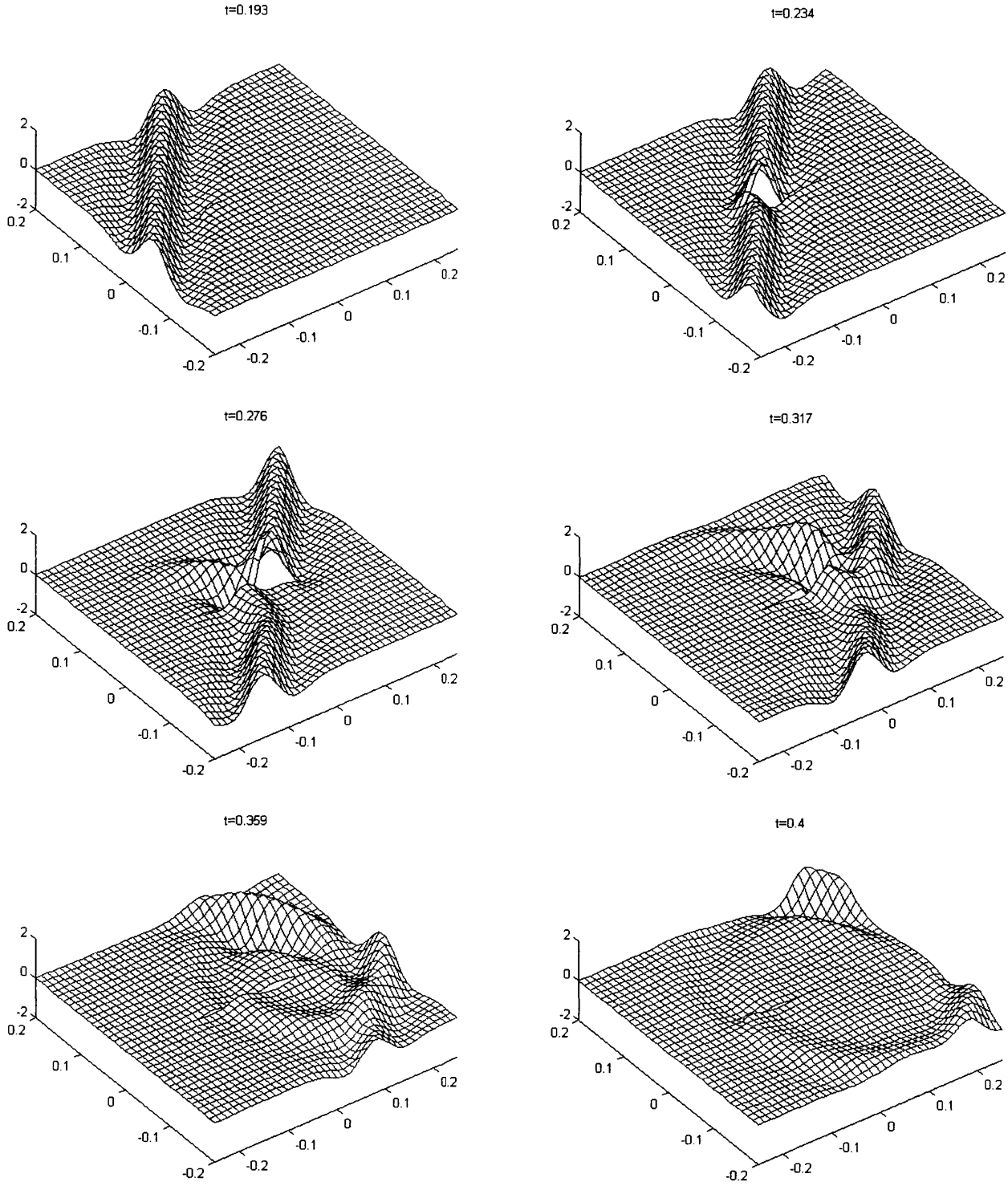

Figure 1-12: SH plane wave incident at 45°

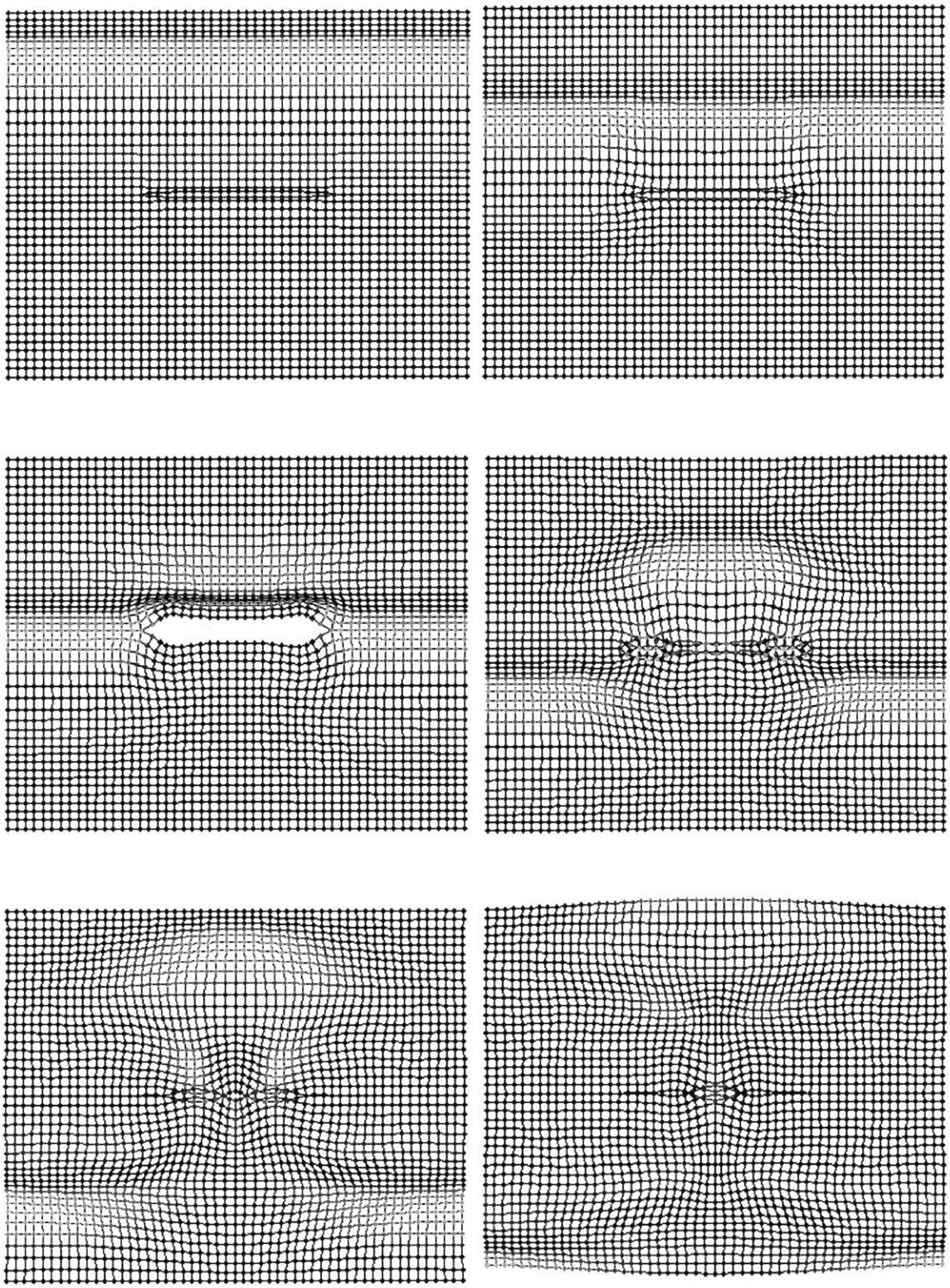

Figure 1-13: P plane wave incident at 90°

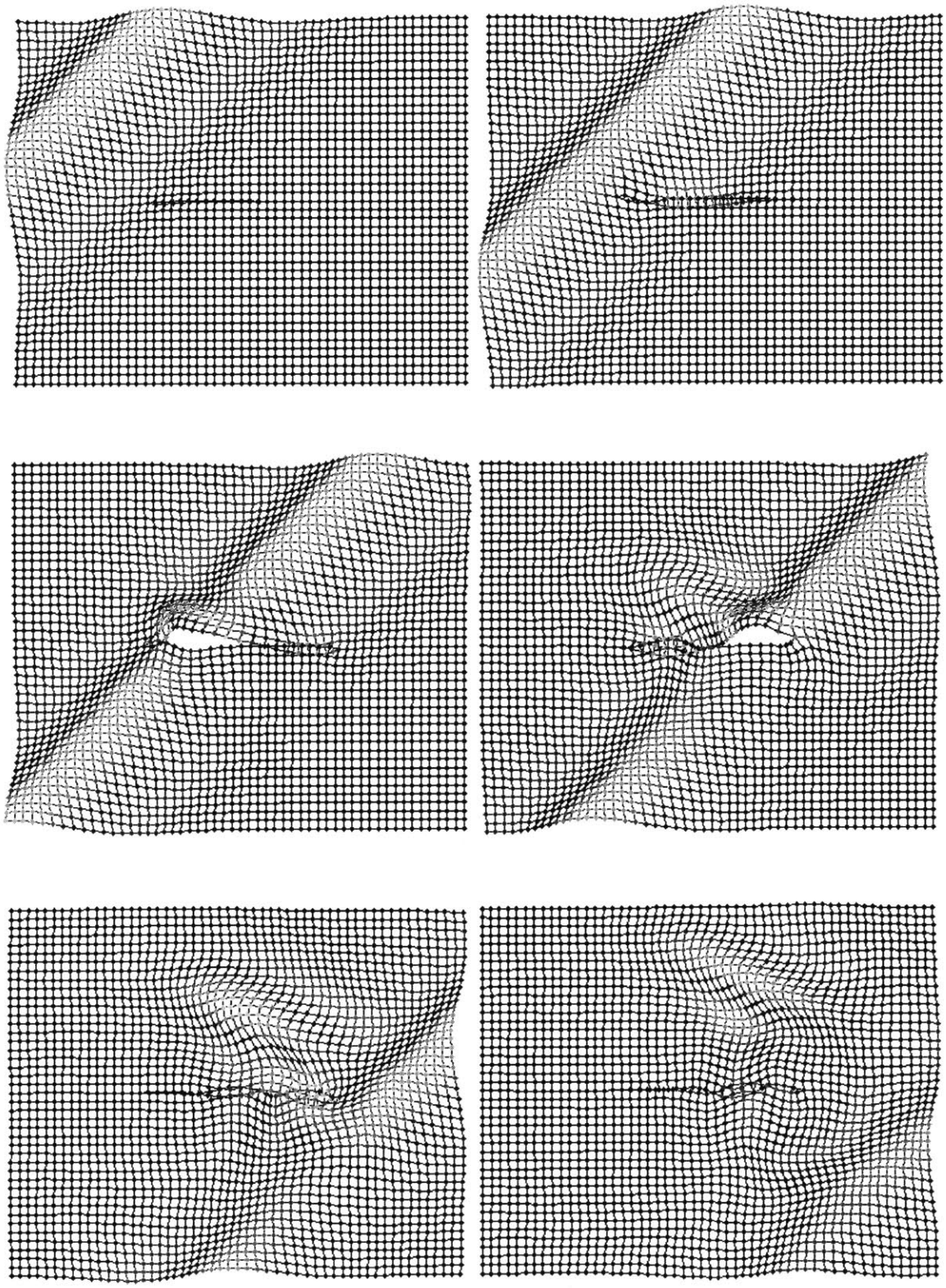

Figure 1-14: P plane wave incident at 45°

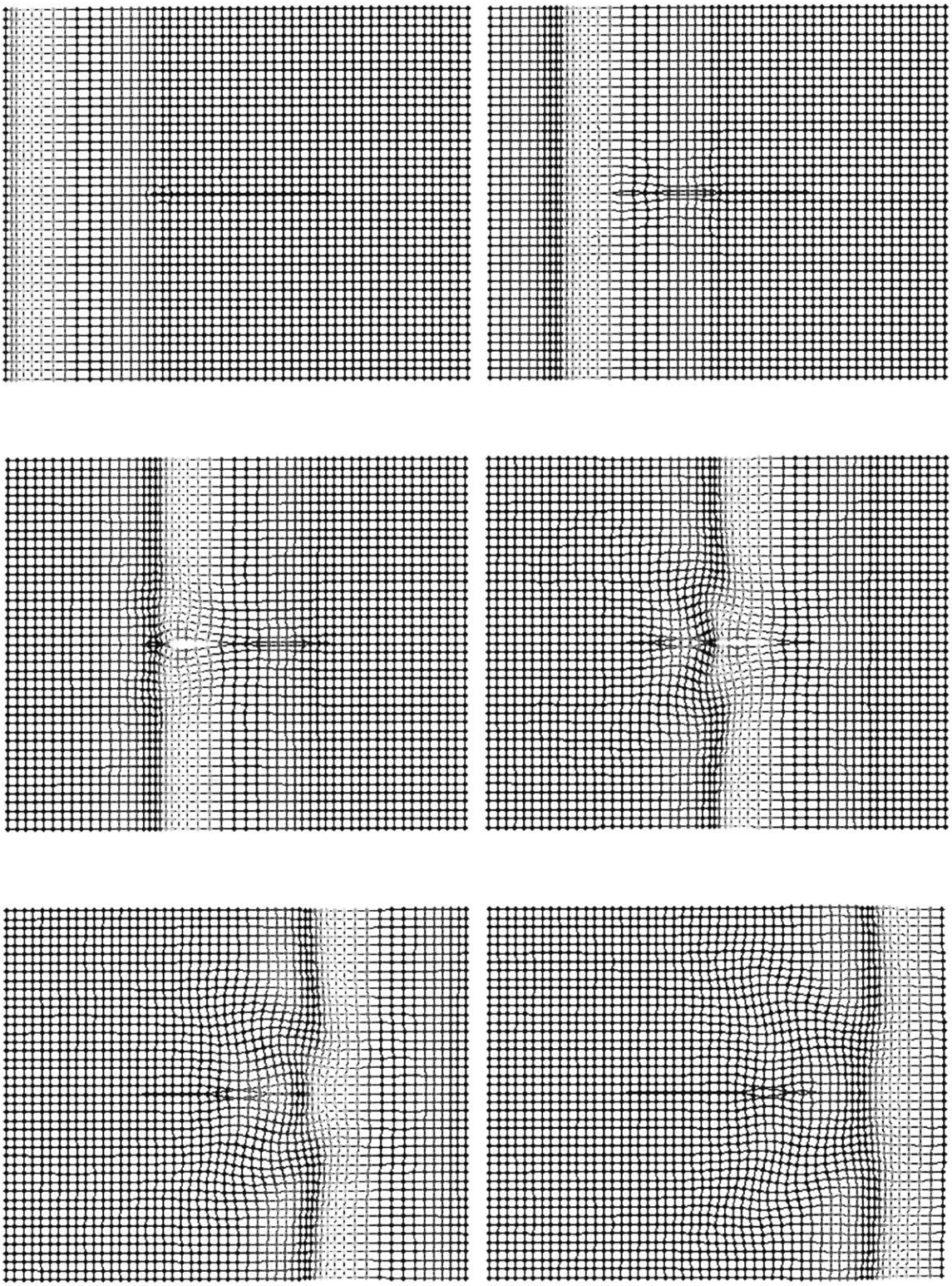

Figure 1-15: P plane wave incident at 0^{o}

Chapter 2 :

Analytical solutions for waves in wave-guides: Some simple problems

Introduction

In this chapter, we present analytical solutions to several simple problems of propagation of waves in plates, namely, a homogeneous plate under anti-plane loading, a homogeneous plate with hybrid boundary conditions under in-plane loading, and a two-layer plate under anti-plane loading.

Introduction of these examples here is not arbitrary, but serves several purposes. First, they provide an introduction to the modal analysis of waves in layered media. Second, they are yardstick against which we can compare the Green's functions computed via the *Thin Layer Method* (TLM) introduced in the next chapter; this comparison helps also establish guidelines in regard to the number of layers needed in the TLM. Third, the analytical solutions in this chapter can be used as fundamental solutions for the Boundary Integral Equation in the previous chapter, so they can be applied to the study of cracks in plates with mixed boundary conditions. Finally, the modal solutions for homogeneous plates can exhibit convergence problems in the near field, so we use the reference solution to address this problem and propose a simple solution.

Harmonic anti-plane (SH) line load in homogeneous plate

First, we consider the simple case of SH waves propagating in a homogeneous plate of thickness h with traction free surfaces. The equation of motion is

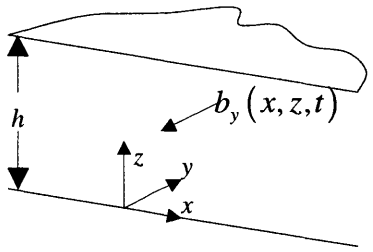

Figure 2-1: Homogeneous free plate subject to anti-plane load

$$\rho\frac{\partial^2 v}{\partial t^2}-\mu\left[\frac{\partial^2 v}{\partial x^2}+\frac{\partial^2 v}{\partial z^2}\right]=b_y(x,z,t) \tag{2.1}$$

Substitution into equation (2.1) of trial solutions of the form $v(x,z,t)=\bar{V}(z)e^{i(\omega t-kx)}$ gives

$$\frac{d^2\bar{V}}{dz^2}+\kappa^2\bar{V}=0 \tag{2.2}$$

where $\kappa^2=k_S^2-k^2$, $k_S=\omega/c_S$, $c_S=\sqrt{\mu/\rho}$ and k is the horizontal wavenumber.

Equation (2.2) has solutions of the form $\bar{V}=A\cos(\kappa z)+B\sin(\kappa z)$. Applying the boundary conditions $\partial v/\partial z\big|_{\substack{z=0\\z=h}}=0$, we obtain the dispersion relationship and the modal shapes in the plate as

$$\begin{aligned} k_n^2&=k_S^2-\alpha_n^2\\ \bar{V}_n&=\cos(\alpha_n z)\end{aligned} \tag{2.3}$$

in which $\alpha_n=n\pi/h$.

Green's function for line loads

Next, consider a unit line load at x=0 and z=z_0, $b_y(x,z,t)=\delta(t)\delta(x)\delta(z-z_0)$. Substitution into equation (2.1) and transformation into the frequency-wavenumber domain gives

$$\rho\omega^2\bar{V}+\mu\left[\frac{\partial^2\bar{V}}{\partial z^2}-k^2\bar{V}\right]=-\delta(z-z_0) \tag{2.4}$$

Assuming a solution of the form $\bar{V}=\sum_{n=0}^{\infty}\phi_n\cos(\alpha_n z)$, we have

$$\sum_{n=0}^{\infty}\left[\kappa^2-\alpha_n^2\right]\phi_n\cos(\alpha_n z)=-\delta(z-z_0)/\mu \tag{2.5}$$

To compute the modal participation factors, ϕ_n, we multiply equation (2.5) by a generic modal shape and integrate over the thickness of the plate, so as to take advantage of the orthogonality of the modes. The solution in the time-wavenumber domain becomes

$$\bar{V} = -\frac{1}{\mu h\left[\left(\omega/c_S\right)^2 - k^2\right]} - \sum_{n=1}^{\infty} \frac{2\cos\left(\alpha_n z_0\right)\cos\left(\alpha_n z\right)}{\mu h\left(k_n^2 - k^2\right)} \tag{2.6}$$

Finally, transforming the solution back into the space domain, the frequency-space Green's function for the plate is

$$G(\omega,x,z) = V(\omega,x,z) = -\frac{\mathrm{i}}{\mu h}\left\{\frac{e^{-\mathrm{i}k_S|x|}}{2k_S} + \sum_{n=1}^{\infty}\frac{\cos\left(\alpha_n z_0\right)\cos\left(\alpha_n z\right)e^{-\mathrm{i}k_n|x|}}{k_n}\right\} \tag{2.7}$$

Stresses are easily obtained from equation (2.7) as

$$\begin{aligned} H_{xy}(\omega,x,z) &= \tau_{xy}(\omega,x,z) = \mp\frac{1}{h}\left\{\frac{e^{-\mathrm{i}k_S|x|}}{2} + \sum_{n=1}^{\infty}\cos\left(\alpha_n z_0\right)\cos\left(\alpha_n z\right)e^{-\mathrm{i}k_n|x|}\right\} \\ H_{zy}(\omega,x,z) &= \tau_{zy}(\omega,x,z) = \frac{\mathrm{i}}{h}\left\{\sum_{n=1}^{\infty}\frac{\alpha_n}{k_n}\cos\left(\alpha_n z_0\right)\sin\left(\alpha_n z\right)e^{-\mathrm{i}k_n|x|}\right\} \end{aligned} \tag{2.8}$$

Green's function for line dipoles

As shown previously, the Green's function for a line dipole may be readily obtained from the line load case as

$$\mathbf{u} = \hat{\mathbf{a}}\nabla_0\mathbf{g} \tag{2.9}$$

Applying (2.9) to the previous results, the Green's function and stresses for a unit dipole with vertical axis are, respectively

$$V(\omega,x,z) = \frac{\mathrm{i}}{\mu h}\left\{\sum_{n=1}^{\infty}\frac{\alpha_n}{k_n}\sin\left(\alpha_n z_0\right)\cos\left(\alpha_n z\right)e^{-\mathrm{i}k_n|x|}\right\} \tag{2.10}$$

$$\begin{aligned}\tau_{xy}(\omega,x,z) &= \pm\frac{1}{h}\left\{\sum_{n=1}^{\infty}\alpha_n \sin(\alpha_n z_0)\cos(\alpha_n z)e^{-ik_n|x|}\right\}\\ \tau_{zy}(\omega,x,z) &= -\frac{i}{h}\left\{\sum_{n=1}^{\infty}\frac{\alpha_n^2}{k_n}\sin(\alpha_n z_0)\sin(\alpha_n z)e^{-ik_n|x|}\right\}\end{aligned} \tag{2.11}$$

Displacements and stresses directly above and below the loads

In general, the previous expressions converge rather fast, due mainly to the fast decay of the exponential term. At the point of application of loads, however, both displacement and stress fields present singularities. Furthermore, note that for any given abscissa, these expressions are similar to a Fourier series, which are known to exhibit convergence problems in the vicinity of discontinuities. So, when attempting to evaluate these expressions immediately above or below the load, we expect to encounter convergence problems.

On the other hand, when applying the BIEM, we are actually interested in the integral over the loaded element, which partially disposes of some of the convergence problems near the singularity. Still, special care is required to properly represent the jumps in both displacements and stresses.

Stress immediately above a line load

Consider the interval $x_1 = \pm a$, such that $|x_1| < a$. The integral of stresses over this interval is

$$\begin{aligned}\overline{\tau}_{zy}(\omega,x,z) &= \frac{i}{h}\left\{\sum_{n=1}^{\infty}\frac{\alpha_n}{k_n}\cos(\alpha_n z_0)\sin(\alpha_n z)\int_{-a}^{a}e^{-ik_n|x|}dx\right\}\\ &= \frac{-2}{h}\left\{\sum_{n=1}^{\infty}\frac{\alpha_n}{k_n^2}\cos(\alpha_n z_0)\sin(\alpha_n z)\left[\cos(k_n x)e^{-ik_n a}-1\right]\right\}\end{aligned} \tag{2.12}$$

Applying (2.3),

$$\bar{\tau}_{zy}(\omega,x,z)=\frac{-2}{h}\left\{\sum_{n=1}^{\infty}\frac{k_S^2}{\alpha_n k_n^2}\cos(\alpha_n z_0)\sin(\alpha_n z)\left[\cos(k_n x)e^{-ik_n a}-1\right]\right.$$
$$\left.-\frac{1}{\alpha_n}\cos(\alpha_n z_0)\sin(\alpha_n z)\left[\cos(k_n x)e^{-ik_n a}-1\right]\right\} \tag{2.13}$$

This expression can be further transformed into

$$\bar{\tau}_{zy}(\omega,x,z)=\frac{2}{h}\left\{\sum_{n=1}^{\infty}\frac{\cos(\alpha_n z_0)\sin(\alpha_n z)}{\alpha_n}\left[\left(1-\frac{k_S^2}{k_n^2}\right)\cos(k_n x)e^{-ik_n a}+\frac{k_S^2}{k_n^2}\right]\right\}$$
$$+\begin{cases}z/h & z<z_0\\ z/h-1 & z>z_0\end{cases} \tag{2.14}$$

This expression explicitly demonstrates the discontinuity.

Displacement immediately above a line dipole

Proceeding as previously, the integral of the displacements over the interval $x_1=\pm a$ due to a line dipole is

$$\bar{V}(\omega,x,z)=\frac{2}{\mu h}\left\{\sum_{n=1}^{\infty}\frac{\sin(\alpha_n z_0)\cos(\alpha_n z)}{\alpha_n}\left[\left(1-\frac{k_S^2}{k_n^2}\right)\cos(k_n x)e^{-ik_n a}+\frac{k_S^2}{k_n^2}\right]\right\}$$
$$+\begin{cases}(z_0-h)/\mu h & z<z_0\\ z_0/\mu h & z>z_0\end{cases} \tag{2.15}$$

Accelerating the convergence of modal solutions

It is a well-known fact that the truncated Fourier series representation of a discontinuous function,

$$g(x)=\sum_{k=-N}^{N}c_k e^{ikx} \tag{2.16}$$

presents ripples in the proximity of the discontinuity. This is often referred to as the Gibbs phenomenon.

Lanczos observed that the ripples have periods of either the last term kept or the first term discarded in the series, and he argued that averaging the truncated series over this period would remove the main effect of the ripples. This averaging process can be accomplished by multiplying the terms of the truncated series by some smoothing factors. Lanczos proposed multiplicative factors of the form $\sigma(N,k)=\sin(\pi k/N)/(\pi k/N)$; other smoothing factors widely used are Fejer's, $c(N,k)=(N-k)/N$. These factors average out the ripples and provide for a faster and smoother convergence to the true value.

The same ripples occur when we use equation (2.12) to compute stresses. Using Lanczos' smoothing factors to increase the convergence rate, equation (2.12) becomes

$$\bar{\tau}_{zy}(\omega,x,z)=\frac{2}{h}\left\{\sum_{n=1}^{N}\left[\frac{\sin(\pi n/N)}{\pi n/N}\right]\frac{\alpha_n}{k_n^2}\cos(\alpha_n z_0)\sin(\alpha_n z)\left[1-\cos(k_n x)e^{-ik_n a}\right]\right\} \quad (2.17)$$

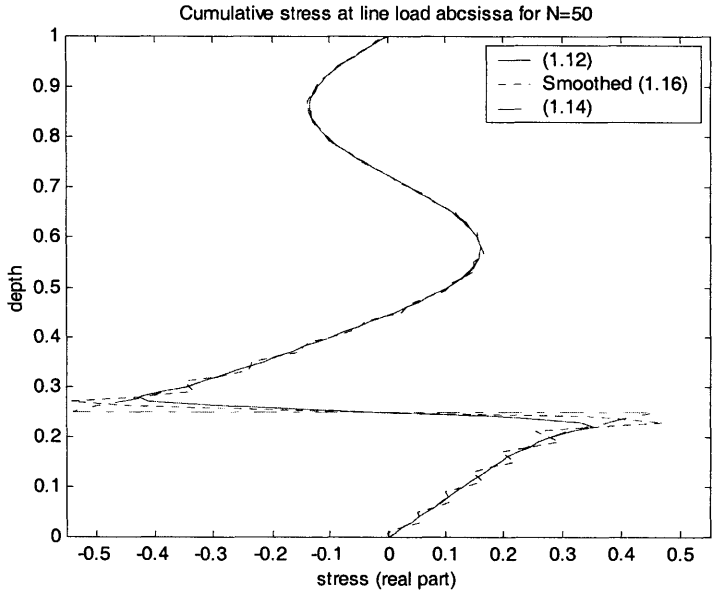

Figure 2-2: Cumulative stress at load abcisa

The Gibbs phenomenon is of great importance in Fourier analysis and Digital Filtering; detailed explanations can be found in books dealing with these topics.

Concerning the stresses at the location of the load, we can use the fact that Fourier series converge to the average value of the function at the discontinuity. Since this average is zero, we simply need to add or subtract one half of the applied force to the value given by equation (2.17).

Stresses for uniform line dipole in homogeneous plate

Stresses due to dipoles present a strong singularity for which simple direct integration is not enough. To evaluate the integrals in the vicinity of this singularity, we apply a point dipole at $(0, z_0)$, isolate a rectangular prism between $x \pm a$ and consider its equilibrium.

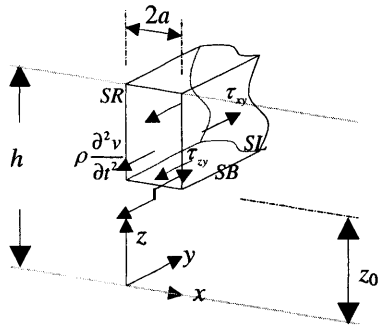

Figure 2-3: Equilibrium above dipole

$$\int_{SR} \tau_{xy} ds - \int_{SL} \tau_{xy} ds - \int_{SB} \tau_{zy} ds - \int_V \rho \frac{\partial^2 v}{\partial t^2} dv = 0 \tag{2.18}$$

Of these four integrals, the first two and the last one can be evaluated in a direct way. Using equations (2.10) and (2.11), we have

$$\begin{aligned} \int_V \rho \frac{\partial^2 v}{\partial t^2} dv &= -\frac{i\rho\omega^2}{\mu h} \sum_{n=1}^{\infty} \frac{\alpha_n}{k_n} \sin(\alpha_n z_0) \left[2 \int_0^{a-x} e^{-ik_n x} dx + \int_{a-x}^{a+x} e^{-ik_n x} dx \right] \int_z^h \cos(\alpha_n z) dz \\ &= \frac{2k_S^2}{h} \sum_{n=1}^{\infty} \frac{\sin(\alpha_n z_0) \sin(\alpha_n z)}{k_n^2} \left[\left(1 - e^{-ik_n a} e^{ik_n x}\right) + i e^{-ik_n a} \sin(k_n x) \right] \end{aligned} \tag{2.19}$$

$$\int_{SR}\tau_{xy}ds-\int_{SL}\tau_{xy}ds=\frac{1}{h}\sum_{n=1}^{\infty}\alpha_n\sin(\alpha_n z_0)\left[e^{-ik_n(a+x)}+e^{-ik_n(a-x)}\right]\int_z^h\cos(\alpha_n z)dz$$
$$=-\frac{2}{h}\sum_{n=1}^{\infty}\sin(\alpha_n z_0)\sin(\alpha_n z)e^{-ik_n a}\cos(k_n x) \tag{2.20}$$

Then, substitution into (2.18) gives

$$\int_{SB}\tau_{zy}ds=\int_{x-a}^{x+a}\tau_{zy}dx=\frac{2}{h}\sum_{n=1}^{\infty}\sin(\alpha_n z_0)\sin(\alpha_n z)\left\{\frac{k_S^2}{k_n^2}\left[\cos(k_n x)e^{-ik_n a}-1\right]-\cos(k_n x)e^{-ik_n a}\right\} \tag{2.21}$$

Harmonic in-plane (SV-P) waves in homogeneous plate with mixed boundary conditions

We consider next a simple case of SV-P waves. The analysis of in-plane waves that propagate in layered media is rather complex, and while there are analytical solutions in the frequency-wavenumber domain, their inversion usually requires numerical techniques. However, for an homogeneous plate with mixed boundary conditions, the SV and the P waves decouple, simplifying the analysis and allowing for an analytical solution in terms of a sums of modes. While this case has limited practical use, it can be very useful as a benchmark for the TLM solutions.

Vertically restrained plate

The equations of motion for in-plane waves propagating in an elastic medium are

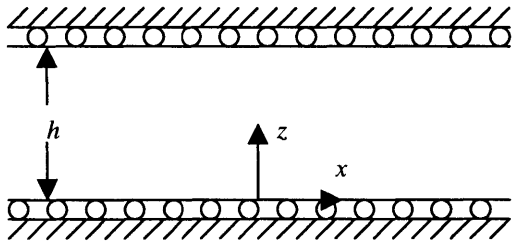

Figure 2-4: Vertically restrained plate subject to in-plane load

$$\begin{aligned}(\lambda+\mu)\left\{\frac{\partial^2 u}{\partial x^2}+\frac{\partial^2 w}{\partial x \partial z}\right\}+\mu\nabla^2 u+f_x&=\rho\frac{\partial^2 u}{\partial t^2}\\(\lambda+\mu)\left\{\frac{\partial^2 u}{\partial x \partial z}+\frac{\partial^2 w}{\partial z^2}\right\}+\mu\nabla^2 w+f_z&=\rho\frac{\partial^2 w}{\partial t^2}\end{aligned} \tag{2.22}$$

Applying the boundary conditions $w\big|_{\substack{z=0\\z=h}}=\tau_{zx}\big|_{\substack{z=0\\z=h}}=0$, the solution of the homogeneous equations gives the dispersion curves and the corresponding modal shapes

$$\begin{aligned}(\omega/c_P)^2&=\alpha_m^2+k_m^2 \qquad m=0,1,2...\text{(P-modes)}\\(\omega/c_S)^2&=\alpha_n^2+k_n^2 \qquad n=1,2,3...\text{(SV-modes)}\end{aligned} \tag{2.23}$$

$$\begin{cases}u_m=\mathrm{i}k\cos(\alpha_m z)e^{-\mathrm{i}(kx-\omega t)}\\w_m=\alpha_m\sin(\alpha_m z)e^{-\mathrm{i}(kx-\omega t)}\end{cases} \quad \text{(P-modes)} \tag{2.24}$$

$$\begin{cases}u_n=\mathrm{i}\alpha_n\cos(\alpha_n z)e^{-\mathrm{i}(kx-\omega t)}\\w_n=-k\sin(\alpha_n z)e^{-\mathrm{i}(kx-\omega t)}\end{cases} \quad \text{(SV-modes)} \tag{2.25}$$

Here $\alpha_n=n\pi/h$, $\alpha_m=m\pi/h$ and k is the horizontal wavenumber. A complete derivation of these equations can be found in Graff[21] (but it should be observed that in this reference, a negative sign convention is used for the exponential term for the frequency).

To solve the non-homogeneous equations, we try a solution based on the modal shapes of the form

$$\begin{aligned}u&=\left\{\mathrm{i}\sum_{m=0}^{\infty}A_m k\cos(\alpha_m z)+\mathrm{i}\sum_{n=1}^{\infty}B_n\alpha_n\cos(\alpha_n z)\right\}e^{-\mathrm{i}(kx-\omega t)}\\w&=\left\{\sum_{m=0}^{\infty}A_m\alpha_m\sin(\alpha_m z)-\sum_{n=1}^{\infty}B_n k\sin(\alpha_n z)\right\}e^{-\mathrm{i}(kx-\omega t)}\end{aligned} \tag{2.26}$$

After substitution into the equations of motion, we obtain

$$\sum_{m=0}^{\infty} A_m \begin{Bmatrix} \mathrm{i}k\left[c_P^2 R_m^2 - \omega^2\right]\cos(\alpha_m z) \\ \alpha_m\left[c_P^2 R_m^2 - \omega^2\right]\sin(\alpha_m z) \end{Bmatrix} + \sum_{n=1}^{\infty} B_n \begin{Bmatrix} \mathrm{i}\alpha_n\left[c_S^2 R_n^2 - \omega^2\right]\cos(\alpha_n z) \\ -k\left[c_S^2 R_n^2 - \omega^2\right]\sin(\alpha_n z) \end{Bmatrix} = \frac{1}{\rho}\begin{Bmatrix} F_x \\ F_z \end{Bmatrix} \quad (2.27)$$

Here $c_P^2 = (\lambda + 2\mu)/\rho$, $c_S^2 = \mu/\rho$, $R_i^2 = k^2 + \alpha_i^2$ and $F_i = \int_{-\infty}^{\infty}\int_{-\infty}^{\infty} f_i e^{\mathrm{i}(kx-\omega t)} dx dt$

To compute the modal participation factors A_m and B_n, we make use of the orthogonality of the modes. Multiplication of the first equation by $\cos(\alpha_i z)$ and of the second by $\sin(\alpha_i z)$, and integration over the whole depth h gives

$$\begin{Bmatrix} \mathrm{i}k\left[c_P^2 R_i^2 - \omega^2\right] & \mathrm{i}\alpha_i\left[c_S^2 R_i^2 - \omega^2\right] \\ \alpha_i\left[c_P^2 R_i^2 - \omega^2\right] & -k\left[c_S^2 R_i^2 - \omega^2\right] \end{Bmatrix} \begin{Bmatrix} .5hA_i \\ .5hB_i \end{Bmatrix} = \frac{1}{\rho}\begin{Bmatrix} \int_0^h F_x \cos(\alpha_i z)\, dz \\ \int_0^h F_z \sin(\alpha_i z)\, dz \end{Bmatrix} \quad i = 1,2,3... \quad (2.28)$$

$$\mathrm{i}k\left[c_P^2 k^2 - \omega^2\right] hA_0 = \frac{1}{\rho}\int_0^h F_x dz$$

In view of this result, we may express the solution as

$$u = \left\{\mathrm{i}A_0 k + \mathrm{i}\sum_{n=1}^{\infty}(A_n k + B_n \alpha_n)\cos(\alpha_n z)\right\} e^{-\mathrm{i}(kx-\omega t)}$$
$$w = \sum_{n=1}^{\infty}(A_n \alpha_n - B_n k)\sin(\alpha_n z) e^{-\mathrm{i}(kx-\omega t)} \quad (2.29)$$

The modal factors are

$$\begin{Bmatrix} A_n \\ B_n \end{Bmatrix} = \frac{2}{\rho h D}\begin{Bmatrix} -k\left[c_S^2 R_n^2 - \omega^2\right] & -\mathrm{i}\alpha_l\left[c_S^2 R_n^2 - \omega^2\right] \\ -\alpha_l\left[c_P^2 R_n^2 - \omega^2\right] & \mathrm{i}k\left[c_P^2 R_n^2 - \omega^2\right] \end{Bmatrix} \begin{Bmatrix} \int_0^h F_x \cos(\alpha_n z)\, dz \\ \int_0^h F_z \sin(\alpha_n z)\, dz \end{Bmatrix} \quad i = 1,2,3... \quad (2.30)$$

$$A_0 = \frac{1}{\mathrm{i}k\left[c_P^2 k^2 - \omega^2\right]\rho h}\int_0^h F_x dz$$

with

$$D = -\mathrm{i}R_l^2\left[c_P^2 R_n^2 - \omega^2\right]\left[c_2^2 R_n^2 - \omega^2\right] \quad (2.31)$$

Green's function for horizontal load

Consider now a concentrated horizontal line load,

$$\begin{aligned} F_x &= \int_{-\infty}^{\infty}\int_{-\infty}^{\infty} f_x e^{\mathrm{i}(kx-\omega t)}dxdt = \int_{-\infty}^{\infty}\int_{-\infty}^{\infty} \delta(z-z_o)\delta(x)\delta(t)e^{\mathrm{i}(kx-\omega t)}dxdt = \delta(z-z_o)e^{\mathrm{i}(kx-\omega t)} \\ F_z &= \int_{-\infty}^{\infty}\int_{-\infty}^{\infty} f_z e^{\mathrm{i}(kx-\omega t)}dxdt = 0 \end{aligned} \tag{2.32}$$

Then

$$\begin{aligned} A_n k + B_n \alpha_n &= \frac{-2\mathrm{i}\left(c_P^2 R_n^2 - \omega^2\right)\cos(\alpha_n z_o)}{\rho h\left[c_P^2 R_n^2 - \omega^2\right]\left[c_S^2 R_n^2 - \omega^2\right]} \\ A_n \alpha_n - B_n k &= \frac{2\mathrm{i}\alpha_n k\left(c_P^2 - c_S^2\right)\cos(\alpha_n z_o)}{\rho h\left[c_P^2 R_n^2 - \omega^2\right]\left[c_S^2 R_n^2 - \omega^2\right]} \\ \mathrm{i}kA_0 &= \frac{1}{\rho h\left[c_P^2 k^2 - \omega^2\right]} \end{aligned} \tag{2.33}$$

Substitution into equation (2.29) gives

$$\begin{aligned} u &= \left\{\frac{1}{\rho h\left[c_P^2 k^2 - \omega^2\right]} + \sum_{n=1}^{\infty}\frac{2\left(c_P^2 R_n^2 - \omega^2\right)\cos(\alpha_n z)\cos(\alpha_n z_o)}{\rho h\left[c_P^2 R_n^2 - \omega^2\right]\left[c_S^2 R_n^2 - \omega^2\right]}\right\} e^{-\mathrm{i}(kx-\omega t)} \\ w &= \sum_{n=1}^{\infty}\frac{2\mathrm{i}\left(c_P^2 - c_S^2\right)k\alpha_n \sin(\alpha_n z)\cos(\alpha_n z_o)}{\rho h\left[c_P^2 R_n^2 - \omega^2\right]\left[c_S^2 R_n^2 - \omega^2\right]} e^{-\mathrm{i}(kx-\omega t)} \end{aligned} \tag{2.34}$$

Inversion of this result into the space domain by contour integration is straightforward. The contour of integration must include the poles in the fourth quadrant (positive real part to satisfy the radiation condition, and negative imaginary part to have a bounded response), which are

$$\begin{aligned} k_{SVn} &= \begin{cases} \sqrt{k_S^2 - \alpha_n^2} & k_S > \alpha_n \\ -\mathrm{i}\sqrt{\alpha_n^2 - k_S^2} & k_S < \alpha_n \end{cases} \\ k_{Pn} &= \begin{cases} \sqrt{k_P^2 - \alpha_n^2} & k_P > \alpha_n \\ -\mathrm{i}\sqrt{\alpha_n^2 - k_P^2} & k_P < \alpha_n \end{cases} \end{aligned} \tag{2.35}$$

Green's function for vertical load

For a vertical line load,

$$F_x = \int_{-\infty}^{\infty}\int_{-\infty}^{\infty} f_x e^{\mathrm{i}(kx-\omega t)}dxdt = 0$$
$$F_z = \int_{-\infty}^{\infty}\int_{-\infty}^{\infty} f_z e^{\mathrm{i}(kx-\omega t)}dxdt = \int_{-\infty}^{\infty}\int_{-\infty}^{\infty}\delta(z-z_o)\delta(x)\delta(t)e^{\mathrm{i}(kx-\omega t)}dxdt = \delta(z-z_o)e^{\mathrm{i}(kx-\omega t)} \tag{2.36}$$

the results are

$$u = \sum_{n=1}^{\infty}\frac{-2\mathrm{i}\alpha_n k\left(c_P^2-c_S^2\right)\cos(\alpha_n z)\sin(\alpha_n z_o)}{\rho h\left[c_P^2R_n^2-\omega^2\right]\left[c_S^2R_n^2-\omega^2\right]}e^{-\mathrm{i}(kx-\omega t)}$$
$$w = \sum_{n=1}^{\infty}\frac{2\left(c_P^2k^2+c_S^2\alpha_n^2-\mathrm{w}^2\right)\sin(\alpha_n z)\sin(\alpha_n z_o)}{\rho h\left[c_P^2R_n^2-\omega^2\right]\left[c_S^2R_n^2-\omega^2\right]}e^{-\mathrm{i}(kx-\omega t)} \tag{2.37}$$

Horizontally restrained plate

The dispersion curves for a horizontally restrained plate are those of a vertically restrained plate, except that now $m = 1,2,3...$ and $n = 0,1,2,3....$ The modal shapes are

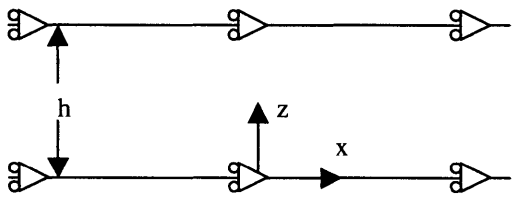

Figure 2-5: Horizontally restrained plate subject to in-plane load

$$\begin{cases} u = \mathrm{i}k\sin(\alpha_m z)e^{-\mathrm{i}(kx-\mathrm{w}t)} \\ w = -\alpha_m\cos(\alpha_m z)e^{-\mathrm{i}(kx-\mathrm{w}t)} \end{cases} \quad \text{(P-modes)} \tag{2.38}$$

$$\begin{cases} u = \mathrm{i}\alpha_n\sin(\alpha_n z)e^{-\mathrm{i}(kx-\mathrm{w}t)} \\ w = k\cos(\alpha_n z)e^{-\mathrm{i}(kx-\mathrm{w}t)} \end{cases} \quad \text{(SV-modes)} \tag{2.39}$$

Hybrid plate

We can obtain the displacements field of a plate with horizontal restraints on one surface and vertical restraints on the other from the previous two cases by simple symmetry and anti-symmetry considerations.

The anti-symmetric modes of a vertically restrained plate, i.e. those for odd values of m, show no horizontal displacement at the center. Therefore, the addition of horizontal restraints at this location does not affect these modes. Dropping the symmetric modes in equations (2.24) and (2.25), and including a factor two to account for the increased depth we obtain the modes of the hybrid case

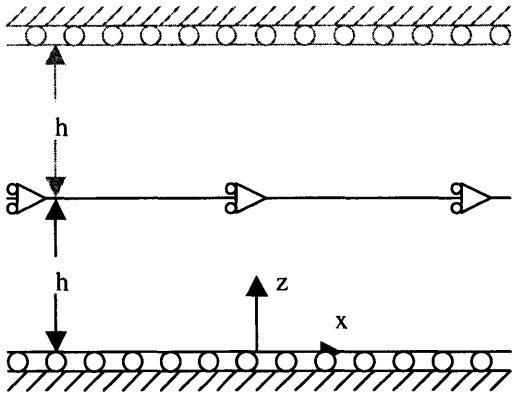

Figure 2-6: Hybrid plate

$$\begin{cases} u = \mathrm{i}k\cos(\beta_m z)e^{-\mathrm{i}(kx-\omega t)} \\ w = \beta_m \sin(\beta_m z)e^{-\mathrm{i}(kx-\omega t)} \end{cases} \quad \text{(P-modes)} \qquad (2.40)$$

$$\begin{cases} u = \mathrm{i}\beta_n \cos(\beta_n z)e^{-\mathrm{i}(kx-\omega t)} \\ w = -k\sin(\beta_n z)e^{-\mathrm{i}(kx-\omega t)} \end{cases} \quad \text{(SV-modes)} \qquad (2.41)$$

Here $\beta_n = \alpha_n/2 = 0.5n\pi/(2h)$, $\beta_m = \alpha_m/2 = m\pi/(2h)$ and $n, m = 1,3,5...$

Because these modes are of the same form of those in (2.24) and (2.25), the Green's function may be obtained from those of the vertically restrained plate by replacing β_n for

α_n and adding the odd terms only. The poles that need be included in the contour of integration are

$$\chi_{SVn} = \begin{cases} \sqrt{k_S^2 - \beta_n^2} & k_S > \beta_n \\ -\mathrm{i}\sqrt{\beta_n^2 - k_S^2} & k_S < \beta_n \end{cases}$$
$$\chi_{Pn} = \begin{cases} \sqrt{k_P^2 - \beta_n^2} & k_P > \beta_n \\ -\mathrm{i}\sqrt{\beta_n^2 - k_P^2} & k_P < \beta_n \end{cases} \tag{2.42}$$

Table of Green's functions

The following table collects the frequency-space Green's functions for the various cases. The Green's functions for dipoles may then be obtained by simple differentiation.

In the evaluation of stresses at the abscissa of the load, we encounter the same convergence issues we find in the anti-plane. For the in-plane case however there are two components of stresses, one parallel to the load and one perpendicular to it. Of the two, only the one parallel to the load is discontinuous at it; the other one shows either a maximum or a minimum. The Lanczos' factors are only applicable for the stress component that shows the discontinuity; if used with the other one they will bias the response.

	Horizontal load	Vertical load
Vertically restrained plate	$u=\frac{-\mathrm{i}e^{\mathrm{i}\omega t}}{\mu hk_S^2}\left\{0.5k_{P0}e^{-\mathrm{i}k_{P0}\lvert x\rvert}+\sum_{n=1}^{\infty}\left[\frac{\alpha_n^2}{k_{SVn}}e^{-\mathrm{i}k_{SVn}\lvert x\rvert}+k_{Pn}e^{-\mathrm{i}k_{Pn}\lvert x\rvert}\right]\cos(\alpha_n z)\cos(\alpha_n z_o)\right\}$ $w=\pm\frac{e^{\mathrm{i}\omega t}}{\mu hk_S^2}\sum_{n=1}^{\infty}\alpha_n\left[e^{-\mathrm{i}k_{SVn}x}-e^{-\mathrm{i}k_{Pn}x}\right]\sin(\alpha_n z)\cos(\alpha_n z_o)$	$u=\pm\frac{e^{\mathrm{i}\omega t}}{\mu hk_S^2}\sum_{n=1}^{\infty}\alpha_n\left[e^{-\mathrm{i}k_{Pn}\lvert x\rvert}-e^{-\mathrm{i}k_{SVn}\lvert x\rvert}\right]\cos(\alpha_n z)\sin(\alpha_n z_o)$ $w=\frac{-\mathrm{i}e^{\mathrm{i}\omega t}}{\mu hk_S^2}\sum_{n=1}^{\infty}\left[\frac{\alpha_n^2}{k_{Pn}}e^{-\mathrm{i}k_{Pn}\lvert x\rvert}+k_{SVn}e^{-\mathrm{i}k_{SVn}\lvert x\rvert}\right]\sin(\alpha_n z)\sin(\alpha_n z_o)$
Horizontally restrained plate	$u=\frac{-\mathrm{i}e^{\mathrm{i}\omega t}}{\mu hk_S^2}\sum_{n=1}^{\infty}\left[\frac{\alpha_n^2}{k_{SVn}}e^{-\mathrm{i}k_{SVn}\lvert x\rvert}+k_{Pn}e^{-\mathrm{i}k_{Pn}\lvert x\rvert}\right]\sin(\alpha_n z)\sin(\alpha_n z_o)$ $w=\pm\frac{e^{\mathrm{i}\omega t}}{\mu hk_S^2}\sum_{n=1}^{\infty}\alpha_n\left[e^{-\mathrm{i}k_{Pn}\lvert x\rvert}-e^{-\mathrm{i}k_{SVn}\lvert x\rvert}\right]\cos(\alpha_n z)\sin(\alpha_n z_o)$	$u=\pm\frac{e^{\mathrm{i}\omega t}}{\mu hk_S^2}\sum_{n=1}^{\infty}\alpha_n\left[e^{-\mathrm{i}k_{SVn}\lvert x\rvert}-e^{-\mathrm{i}k_{Pn}\lvert x\rvert}\right]\sin(\alpha_n z)\cos(\alpha_n z_o)$ $w=\frac{-\mathrm{i}e^{\mathrm{i}\omega t}}{\mu hk_S^2}\left\{0.5k_{SV0}e^{-\mathrm{i}k_{SV0}\lvert x\rvert}+\sum_{n=1}^{\infty}\left[\frac{\alpha_n^2}{k_{Pn}}e^{-\mathrm{i}k_{Pn}\lvert x\rvert}+k_{SVn}e^{-\mathrm{i}k_{SVn}\lvert x\rvert}\right]\cos(\alpha_n z)\cos(\alpha_n z_o)\right\}$
Hybrid	$u=\frac{-\mathrm{i}e^{\mathrm{i}\omega t}}{\mu hk_S^2}\sum_{n=1,3,5\ldots}\left[\frac{\beta_n^2}{\chi_{SVn}}e^{-\mathrm{i}\chi_{SVn}\lvert x\rvert}+\chi_{Pn}e^{-\mathrm{i}\chi_{Pn}\lvert x\rvert}\right]\cos(\beta_n z)\cos(\beta_n z$ $w=\pm\frac{e^{\mathrm{i}\omega t}}{\mu hk_S^2}\sum_{n=1,3,5\ldots}\beta_n\left[e^{-\mathrm{i}\chi_{SVn}\lvert x\rvert}-e^{-\mathrm{i}\chi_{Pn}\lvert x\rvert}\right]\sin(\beta_n z)\cos(\beta_n z_o)$	$u=\pm\frac{e^{\mathrm{i}\omega t}}{\mu hk_S^2}\sum_{n=1,3,5\ldots}\beta_n\left[e^{-\mathrm{i}\chi_{Pn}\lvert x\rvert}-e^{-\mathrm{i}\chi_{SVn}\lvert x\rvert}\right]\cos(\beta_n z)\sin(\beta_n z_o)$ $w=\frac{-\mathrm{i}e^{\mathrm{i}\omega t}}{\mu hk_S^2}\sum_{n=1,3,5\ldots}\left[\frac{\beta_n^2}{\chi_{Pn}}e^{-\mathrm{i}\chi_{Pn}\lvert x\rvert}+\chi_{SVn}e^{-\mathrm{i}\chi_{SVn}\lvert x\rvert}\right]\sin(\beta_n z)\sin(\beta_n z_o$

	Horizontal load	Vertical load
Vertically restrained plate	$\tau_{xx} = \pm\dfrac{e^{i\omega t}}{hk_S^2}\left\{\begin{array}{l} -k_S^2\left[\dfrac{e^{-ik_{P0}\lvert x\rvert}}{2}+\sum\limits_{n=1}^{\infty}e^{-ik_{Pn}\lvert x\rvert}\cos(\alpha_n z)\cos(\alpha_n z_o)\right] \\ +2\sum\limits_{n=1}^{\infty}\alpha_n^2\left[e^{-ik_{Pn}\lvert x\rvert}-e^{-ik_{SVn}\lvert x\rvert}\right]\cos(\alpha_n z)\cos(\alpha_n z_o)\end{array}\right\}$	$\tau_{xx} = \dfrac{-ie^{i\omega t}}{hk_S^2}\left\{\begin{array}{l} k_S^2\sum\limits_{n=1}^{\infty}\dfrac{\alpha_n}{k_{Pn}}e^{-ik_{Pn}\lvert x\rvert}\cos(\alpha_n z)\sin(\alpha_n z_o) \\ -2\sum\limits_{n=1}^{\infty}\alpha_n\left[\dfrac{\alpha_n^2}{k_{Pn}}e^{-ik_{Pn}\lvert x\rvert}+k_{SVn}e^{-ik_{SVn}\lvert x\rvert}\right]\cos(\alpha_n z)\sin(\alpha_n z_o)\end{array}\right\}$
	$\tau_{zz} = \pm\dfrac{e^{i\omega t}}{hk_S^2}\left\{\begin{array}{l} \left(2k_P^2-k_S^2\right)\left[\dfrac{e^{-ik_{P0}\lvert x\rvert}}{2}+\sum\limits_{n=1}^{\infty}e^{-ik_{Pn}\lvert x\rvert}\cos(\alpha_n z)\cos(\alpha_n z_o)\right] \\ -2\sum\limits_{n=1}^{\infty}\alpha_n^2\left[e^{-ik_{Pn}\lvert x\rvert}-e^{-ik_{SVn}\lvert x\rvert}\right]\cos(\alpha_n z)\cos(\alpha_n z_o)\end{array}\right\}$	$\tau_{zz} = \dfrac{-ie^{i\omega t}}{hk_S^2}\left\{\begin{array}{l} k_S^2\sum\limits_{n=1}^{\infty}\dfrac{\alpha_n}{k_{Pn}}e^{-ik_{Pn}\lvert x\rvert}\cos(\alpha_n z)\sin(\alpha_n z_o) \\ -2\sum\limits_{n=1}^{\infty}\alpha_n\left[k_{Pn}e^{-ik_{Pn}\lvert x\rvert}-k_{SVn}e^{-ik_{SVn}\lvert x\rvert}\right]\cos(\alpha_n z)\sin(\alpha_n z_o)\end{array}\right\}$
	$\tau_{zx} = \dfrac{ie^{i\omega t}}{hk_S^2}\sum\limits_{n=1}^{\infty}\left[\left(\dfrac{\alpha_n^2}{k_{SVn}}-k_{SVn}\right)e^{-ik_{SVn}\lvert x\rvert}+2k_{Pn}e^{-ik_{Pn}\lvert x\rvert}\right]\alpha_n\sin(\alpha_n z)\cos(\alpha_n z_o)$	$\tau_{zx} = \mp\dfrac{e^{i\omega t}}{hk_S^2}\sum\limits_{n=1}^{\infty}\left[2\alpha_n^2\left(e^{-ik_{Pn}\lvert x\rvert}-e^{-ik_{SVn}\lvert x\rvert}\right)+k_S^2e^{-ik_{SVn}\lvert x\rvert}\right]\sin(\alpha_n z)\sin(\alpha_n z_o)$

2-layer plate subject to harmonic anti-plane line loads

The third case we consider for analytical treatment is that of a free-free plate with two material layers, each one of which has distinct properties and its own equation of motion.

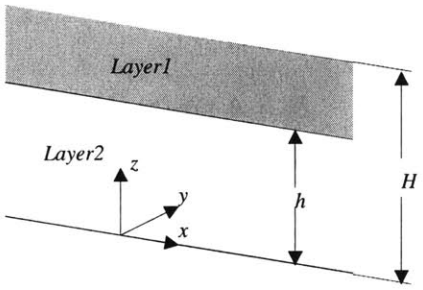

$$\rho_L \frac{\partial^2 v}{\partial t^2} - \mu_L \left[\frac{\partial^2 v}{\partial x^2} + \frac{\partial^2 v}{\partial z^2} \right] = b_y(x,z,t) \qquad L = 1,2 \tag{2.43}$$

There are now four boundary conditions: free edge at top and bottom, and continuity of displacements and stresses at the interface of the layers.

We consider first the homogeneous equation, to which we apply trial functions of the form $v(x,z,t) = \overline{V}(z) e^{\mathrm{i}(\omega t - kx)}$. The result is of the form

$$\frac{d^2 \overline{V}}{dz^2} + \kappa_L^2 \overline{V} = 0 \tag{2.44}$$

where $\kappa_L^2 = k_{SL}^2 - k^2$, $k_{SL} = \omega / c_{SL}$ and $c_{SL} = \sqrt{\mu_L / \rho_L}$. Note that the continuity of stresses and displacements at the interface demands the horizontal wavenumber to be the same in both layers.

These equations have solutions of the form $\overline{V} = A_L \cos(\kappa_L z) + B_L \sin(\kappa_L z)$, which upon substitution of the boundary conditions leads to

$$\begin{aligned}
&\partial\bar{V}/\partial z\big|_{z=H} = \kappa_1\left(-A_1\sin(\kappa_1 H)+B_1\cos(\kappa_1 H)\right)=0\\
&\partial\bar{V}/\partial z\big|_{z=0} = \kappa_2\left(-A_2\sin(\kappa_2 0)+B_2\cos(\kappa_2 0)\right)=0\\
&A_1\cos(\kappa_1 h)+B_1\sin(\kappa_1 h)=A_2\cos(\kappa_2 h)+B_2\sin(\kappa_2 h)\\
&\kappa_1\left(-A_1\sin(\kappa_1 h)+B_1\cos(\kappa_1 h)\right)=\kappa_2\left(-A_2\sin(\kappa_2 h)+B_2\cos(\kappa_2 h)\right)
\end{aligned} \tag{2.45}$$

From the first two equations,

$$\begin{aligned}
B_1 &= A_1\tan(\kappa_1 H)\\
B_2 &= 0
\end{aligned} \tag{2.46}$$

and substitution of (2.46) into the last two boundary conditions yields

$$\begin{pmatrix} \cos(\kappa_1 h)+\sin(\kappa_1 h)\tan(\kappa_1 H) & -\cos(\kappa_2 h)\\ \mu_1\kappa_1\left(-\sin(\kappa_1 h)+\cos(\kappa_1 h)\tan(\kappa_1 H)\right) & \mu_2\kappa_2\sin(\kappa_2 h)\end{pmatrix}\begin{pmatrix}A_1\\A_2\end{pmatrix}=\begin{pmatrix}0\\0\end{pmatrix} \tag{2.47}$$

By setting the determinant of the square matrix to zero, we get the dispersion relationship

$$\boxed{\mu_2\kappa_2\tan(\kappa_2 h)=-\mu_1\kappa_1\tan\left(\kappa_1(H-h)\right)} \tag{2.48}$$

The modal shapes are

$$\boxed{\bar{V}_n=\begin{cases}\cos(\kappa_{1n}z)+\tan(\kappa_{1n}H)\sin(\kappa_{1n}z)\\ \left[\cos(\kappa_{1n}h)+\tan(\kappa_{1n}H)\sin(\kappa_{1n}h)\right]\cos(\kappa_{2n}z)/\cos(\kappa_{2n}h)\end{cases}} \tag{2.49}$$

The dispersion curves

The problem to solve is: given the frequency ω, determine the wavenumbers k that satisfy the wave equations and boundary conditions without the need for external loads (i.e. the normal modes of wave propagation). The function $k(\omega)$ thus obtained is referred to as the dispersion relationship. To this effect, and assuming the top layer to be slower one, we define $\eta = c_{S1}/c_{S2} < 1$ and $\chi = k/k_{\beta 1}$, and rewrite equation (2.48) as

$$\mu_2\sqrt{\eta^2-\chi^2}\tan\left[(\omega h/c_{S1})\sqrt{\eta^2-\chi^2}\right]=-\mu_1\sqrt{1-\chi^2}\tan\left[\left(\omega(H-h)/c_{S1}\right)\sqrt{1-\chi^2}\right] \tag{2.50}$$

For any given frequency, we can identify three regions

1. $\chi^2 > 1$: the argument of the tangents on both sides are imaginary numbers, which changes them into hyperbolic tangents. Thus, the dispersion equation becomes

$$\mu_2\sqrt{\chi^2-\eta^2}\tanh\left[(\omega h/c_{S1})\sqrt{\chi^2-\eta^2}\right]=-\mu_1\sqrt{\chi^2-1}\tanh\left[(\omega(H-h)/c_{S1})\sqrt{\chi^2-1}\right] \quad (2.51)$$

   In this interval there are no real roots, since the right hand side (r.h.s.) is always positive while the left hand side (l.h.s.) is always negative.

2. $1 > \chi^2 > \eta^2$: Now, the tangent on the r.h.s. has branches that intersect the hyperbolic tangent on the l.h.s. at discrete points. If we subdivide this interval into sub-intervals by the values of χ^2 at which the tangent is unbounded, we find that every sub-interval contains just a single root. The modes corresponding to these roots propagate only in the top layer (the slow layer); while, in the bottom layer they decay exponentially with depth.

3. $\chi^2 < \eta^2$: In this interval, there are two families of tangents of opposite sign. Subdividing it by the values of χ^2 at which both families are unbounded, in every sub-interval there is one and only one root. As a special case, if for any value of χ^2 both branches are unbounded then this value is an actual root, too. In this interval, the modes propagate in both layers.

Given the simple structure of the dispersion equation for this case, it is very easy to search for the roots numerically following the subdivision scheme explained above.

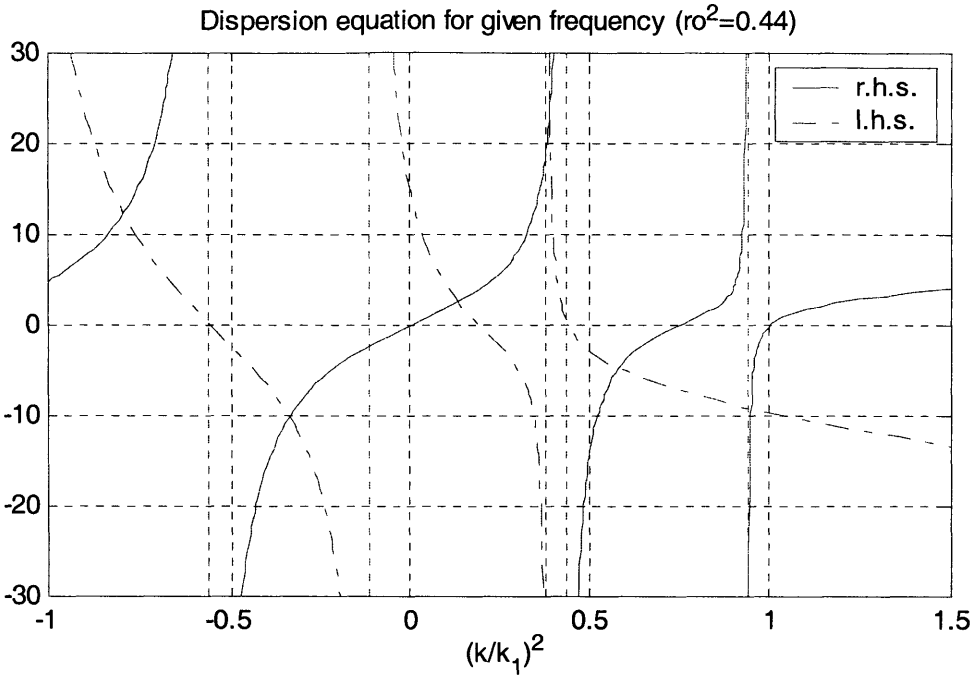

Figure 2-7: Root of the dispersion equation for a two-layer plate

Green's function for line loads

Considering unit line load, $b_y(x,z,t)=\delta(t)\delta(x)\delta(z-z_0)$, and a solution of the form $\bar{V}=\sum_n \phi_n \bar{V}_n$, we have

$$\sum_{n=0}^{\infty}\left[\kappa_L^2-\kappa_{Ln}^2\right]\phi_n\bar{V}_n=-\delta(z-z_0)/\mu_L \tag{2.52}$$

Here, we also can use the orthogonality of the modes to compute the modal factors

$$\int_0^H \mu_L\bar{V}_n\bar{V}_n dz=\begin{cases}\mu_1 H/2\cos^2(\kappa_{1n}H)+\mu_1\sin(2\kappa_{1n}\Delta)\left[1-(\kappa_{1n}/\kappa_{2n})^2\right]/4\kappa_{1n}\cos^2(\kappa_{1n}H)\\ +h\left[\mu_2\cos^2(\kappa_{1n}\Delta)-\mu_1+(\mu_1\kappa_{1n}/\mu_2\kappa_{2n})^2\sin^2(\kappa_{1n}\Delta)\right]/2\cos^2(\kappa_{1n}H)\end{cases} \tag{2.53}$$

$$\int_0^H \mu_L\bar{V}_n\bar{V}_m dz=0 \qquad n\neq m$$

Finally, the Green's function in the time-wavenumber domain is

$$\boxed{\bar{V}(k,z,t)=\sum_{n=0}^{\infty}\frac{-\bar{V}_n(z_0)\bar{V}_n(z)}{\left(k_n^2-k^2\right)\int_0^H \mu_L\bar{V}_n\bar{V}_n dz}_n} \tag{2.54}$$

Chapter 3 :

Singular solutions for layered plates: The Thin Layer Method (TLM)

Introduction

The classical approach to the study of waves in wave-guides and layered media involves the use of Integral Transforms, such as the Fourier and Hankel transforms. The application of these transforms reduces the dimensionality of the wave equation, yielding in the case of layered media an equation in which depth is the only variable, namely *the depth-dependent equation*. This approach is equivalent to the *method of Separation of Variables*. Usually, the depth-dependent equation is much easier to handle, and after its solution has been found, it must be transformed back into the original space. For simple cases, analytical transformation via contour integration is possible; cases that are more complicated require numerical integration or other approximate methods.

The back transformation by means of numerical techniques will generally require a large number of points in the frequency-wavenumber domain. Therefore, a fast and reliable method to solve the wave equation in the transformed space is critical to the applicability of Integral Transforms. Among the possible different approaches to handle the transformed equation are the Transfer Matrix Method, the Direct Global method, the use of Stiffness Matrices and the TLM.

The first numerical attempt at this problem is the Transfer Matrix Approach presented by Thomson[22] and Haskell[23]. In this approach, the medium is first divided into a set of homogeneous layers. Thereafter, a so-called Transfer Matrix (T-Matrices) relating the stresses and displacements at one interface to those at the other interface is built for each and every layer. Using the continuity conditions at the interfaces, the state between any two interfaces on the media can then be related via a simple matrix equation, which is obtained by multiplying the T-Matrices for the layers contained between these two arbitrary interfaces. While the T-matrix approach requires moderate computational effort and memory, it suffers from serious numerical shortcomings that relate to the numerical stability of some of the terms that couple one layer to the next, particularly at high frequencies and/or when the layers are thick in comparison to the dominant wavelengths.

Kausel & Roesset[24] presented and alternative method based on Stiffness Matrices, which they derived directly from the T-matrices. While in principle fully equivalent to the T-matrix approach, the use of stiffness matrices has the significant advantage of avoiding the numerical instabilities of the T-matrices, they are fully symmetric, and their bandwidth is half as large as that of the T-matrices. In addition, they allows for the use of sub-structuring, condensation and the simultaneous treatment for multiple loadings. Finally, they lead naturally to the TLM.

The Direct Global Method[25], developed by Schmidt in the 80s, uses a global element formulation in which each layer is represented in terms of so-called propagators. It differs from the stiffness matrix method in that the unknowns are wave amplitudes instead of interface displacements. As a result, the global matrix has twice the bandwidth of the global stiffness matrix, and in addition, it is not symmetric. Thus, it is substantially less efficient than the stiffness matrix approach.

The formulations summarized above share a common inefficiency, namely they all involve transcendental functions as arguments in the matrices. These make a closed form evaluation of the integral transform all but intractable. On the other hand, if the thicknesses of the layers are small as compared to the wavelengths of interest, it is possible to linearize the transcendental functions that govern the displacements. This procedure, initially proposed by Lysmer and Waas, led in time to the TLM. The compelling advantage of this approach is that the substitution of the transcendental expressions by algebraic ones allows for analytical computation of at least one of the integral transforms required, either that over wavenumbers, or the one over frequencies. Another appealing feature of special interest for this research is that it provides an elegant and easy way to implement the Green's functions for layered plates[26].

The formulation of the TLM was initially obtained from a limiting process, and subsequently derived by Waas[27] using variational principles. In this report, we will derive the TLM equation using principles of Weighted Residuals as suggested by Kausel[28,29].

Discrete model for the anti-plane problem

Consider a horizontally stratified elastic plate subject to anti-plane loading, and a Cartesian coordinate system with y-axis parallel to the motion of the particles and z-axis perpendicular to the layering (Figure 3-1). The differential equation of motion is

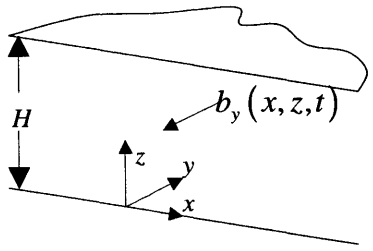

Figure 3-1: Plate subject to anti-plane load

$$\rho(z)\frac{\partial^2 v(x,z)}{\partial t^2} - \mu(z)\nabla^2 v(x,z) = \rho(z) f_y(x,z) = b_y(x,z) \tag{3.1}$$

In the TLM, we approximate the plate as an assemblage of homogeneous layers that are thin in comparison to the wave lengths expected to be involved in the analysis. Within each thin layer, we assume that the displacements at any depth can be determined by numerical interpolation of the displacements at a fixed, but arbitrary number n of conveniently chosen layer interfaces which are akin to nodes in a conventional finite element formulation. The most common choices are n=2 or n=3, which lead to linear and quadratic layers, respectively. For a generic thin layer m, the displacement at any point is given by

$$v(x,z,t) = \mathbf{N}(z)\cdot\mathbf{U}_m(x,t) \tag{3.2}$$

In this expression, $\mathbf{U}_m$ is a column vector containing the n nodal displacements and $\mathbf{N}$ is a row vector with n interpolation functions. Note that the nodal displacements are only function of x and t, while the interpolation functions depend only on z. While the

numbering of the nodes is arbitrary, we choose to number them downwards (opposite to increasing values of z); thus, the first node is at the top while the last is at the bottom.

The first step in the derivation of the Discrete Equation of Motion is to isolate a thin layer of thickness h from the plate, and apply external tractions T_1 and T_n at its top and bottom boundaries equal and opposite to the actual internal stresses, τ_1 and τ_n, so as to preserve equilibrium. Substitution of the approximated displacements, equation (3.2), into the wave equation (3.1) gives some residual body force, r, due to the difference between the approximated and the actual displacements, and some residual tractions at the boundaries

$$r = b_y - \rho_m \mathbf{N}\ddot{\mathbf{U}}_m + \mu_m \left[\mathbf{N}''\mathbf{U}_m + \mathbf{N}\mathbf{U}_m''\right] \tag{3.3}$$

$$q_i = T_i - \tau_i \qquad (i = 1, n) \tag{3.4}$$

Next, we require the work performed by the residual force and tractions throughout an elementary volume of the thin layer $(dx \cdot dy \cdot h)$ under any compatible virtual field of displacements to be zero (method of Weighted Residuals). Choosing a virtual displacement of the form $\delta v = \mathbf{N} \cdot \delta \mathbf{U}_m$, we obtain

$$\delta \mathbf{U}_m{}^{\mathrm{T}} \cdot \left\{ \mathbf{Q}_m + \int_{z_n}^{z_1} \left[\mathbf{N}^{\mathrm{T}} \cdot b_y - \rho_m \mathbf{N}^{\mathrm{T}} \mathbf{N} \ddot{\mathbf{U}}_m + \mu_m \mathbf{N}^{\mathrm{T}} \left(\mathbf{N}''\mathbf{U}_m + \mathbf{N}\mathbf{U}_m'' \right) \right] dz \right\} dxdy = 0 \tag{3.5}$$

Here, $\mathbf{Q}_m$ is column vector of the same dimensions as $\mathbf{U}_m$ with all of its components zero except the first and last elements that are the residual tractions at the top and bottom of the thin layer respectively.

$$\mathbf{Q}_m = \begin{bmatrix} T_1 \\ \vdots \\ T_N \end{bmatrix} - \mu_m \begin{bmatrix} \mathbf{N}'|_{z_1} \\ \vdots \\ -\mathbf{N}'|_{z_n} \end{bmatrix} \mathbf{U}_m(x,t) \tag{3.6}$$

Because this must hold for any virtual displacement, after substitution of (3.6) into (3.5), we obtain

$$\mathbf{P}_m = \mathbf{M}_m \ddot{\mathbf{U}}_m - \mathbf{A}_m \mathbf{U}_m'' + \mathbf{G}_m \mathbf{U}_m \tag{3.7}$$

$$\mathbf{P}_m = \mathbf{T} + \int_{z_n}^{z_1} \mathbf{N}^{\mathrm{T}} b_y dz$$
$$\mathbf{M}_m = \int_{z_n}^{z_1} \rho_m \mathbf{N}^{\mathrm{T}} \mathbf{N} dz \qquad \mathbf{G} = \int_{z_n}^{z_1} \mu_m \left\{ \begin{bmatrix} \mathbf{N}'\big|_{z_1} \\ \vdots \\ -\mathbf{N}'\big|_{z_n} \end{bmatrix} - \mathbf{N}^{\mathrm{T}} \mathbf{N}'' \right\} dz \tag{3.8}$$
$$\mathbf{A}_m = \int_{z_n}^{z_1} \mu_m \mathbf{N}^{\mathrm{T}} \mathbf{N} dz$$

Now that we have the equilibrium equation for a single thin layer subject to external forces and equilibrating tractions T_1 and T_n, (3.7), assembling the equations for all the layers gives us the Discrete Equilibrium Equation for the whole system. The final equation includes only actual forces, as the equilibrating internal forces cancel each other out in the assembling process.

Discrete model for the in-plane problem

For the SV-P problem, we have two coupled differential equations

$$\begin{aligned} (\lambda+\mu)\left\{\frac{\partial^2 u}{\partial x^2} + \frac{\partial^2 w}{\partial x \partial z}\right\} + \mu \nabla^2 u + f_x &= \rho \frac{\partial^2 u}{\partial t^2} \\ (\lambda+\mu)\left\{\frac{\partial^2 u}{\partial x \partial z} + \frac{\partial^2 w}{\partial z^2}\right\} + \mu \nabla^2 w + f_z &= \rho \frac{\partial^2 w}{\partial t^2} \end{aligned} \tag{3.9}$$

Repeating the same process as before, we obtain for a single layer the following equilibrium equation, where we have dropped the sub-index *m*,

$$\mathbf{P} = \mathbf{M}\ddot{\mathbf{U}} - \mathbf{A}\mathbf{U}'' - \mathbf{B}\mathbf{U}' + \mathbf{G}\mathbf{U} \tag{3.10}$$

$$
\begin{aligned}
\mathbf{P} &= \mathbf{T} + \int_{z_n}^{z_1} \mathbf{N}^{\mathrm{T}} b_y \, dz \\
\mathbf{M} &= \int_{z_n}^{z_1} \rho \mathbf{N}^{\mathrm{T}} \mathbf{N} \, dz \\
\mathbf{A} &= \int_{z_n}^{z_1} \mathbf{N}^{\mathrm{T}} \begin{bmatrix} \lambda + 2\mu & 0 \\ 0 & \mu \end{bmatrix} \mathbf{N} \, dz \\
\mathbf{G} &= \int_{z_1}^{z_n} \left\{ \begin{bmatrix} \mu \begin{bmatrix} \mathbf{N}'|_{z_1} \\ \vdots \\ -\mathbf{N}'|_{z_n} \end{bmatrix} & \cdot \\ \cdot & (\lambda + 2\mu) \begin{bmatrix} \mathbf{N}'|_{z_1} \\ \vdots \\ -\mathbf{N}'|_{z_n} \end{bmatrix} \end{bmatrix} - \mathbf{N}^{\mathrm{T}} \begin{bmatrix} \lambda + 2\mu & 0 \\ 0 & \mu \end{bmatrix} \mathbf{N}'' \right\} dz
\end{aligned}
\tag{3.11}
$$

In these expressions, the top half of the vector of nodal displacements corresponds to the horizontal displacements and the bottom half to the vertical displacements. In addition, the interpolation matrix is $\mathbf{N}^{\mathrm{T}} = \begin{bmatrix} \mathbf{N}^{\mathrm{T}} & \cdot \\ \cdot & \mathbf{N}^{\mathrm{T}} \end{bmatrix}$ where $\mathbf{N}$ is a row vector that contains the same interpolation functions used for the anti-plane case.

Solution of the discrete equation of motion

To solve the discrete equation of motion, we begin by Fourier transforming the horizontal coordinate x into the horizontal wavenumber k

$$
\bar{\mathbf{P}}(k,t) = \mathbf{M}\ddot{\bar{\mathbf{U}}} + \left(k^2\mathbf{A} + \mathrm{i}k\mathbf{B} + \mathbf{G}\right)\bar{\mathbf{U}} \tag{3.12}
$$

in which the direct and inverse integral transformation are defined as

$$
\begin{aligned}
\bar{\mathbf{U}} &= \int_{-\infty}^{\infty} \mathbf{U} \exp(\mathrm{i}kx) \, dx \\
\mathbf{U} &= \frac{1}{2\pi} \int_{-\infty}^{\infty} \bar{\mathbf{U}} \exp(-\mathrm{i}kx) \, dk
\end{aligned}
\tag{3.13}
$$

There exist at least four alternative ways of solving this equation[29]:

- Use a finite differences scheme to solve at each t, integrate numerically over wavenumbers, and march forward in time.
- Transform equation (3.12) into the frequency domain, solve in the frequency domain and integrate numerically over both frequencies and wavenumbers.
- Transform equation (3.12) into the frequency domain, at each frequency solve an eigenvalue problem for wavenumbers, integrate analytically over wavenumbers and then numerically over frequency.
- Transform equation (3.12) into the frequency domain, solve at each wavenumber an eigenvalues for frequencies, integrate analytically over frequencies and then numerically over wavenumbers[28].

Of these four alternatives, the first solution is the most expensive and is computationally unattractive; in the second alternative, there is no actual incentive to use the discrete solution over the continuous solutions (T-matrix approach or others); and, between the last two, the third alternative (modal solution in the frequency domain) presents clear advantages both in manageability and computational effort. In particular, it allows for easy computation of stresses and easy modeling of material damping. Also, because the integration over wavenumber is performed analytically, there is no spatial aliasing and thus no limitation in maximum range. Its principal disadvantage is that it requires solving a quadratic eigenvalue problem with complex eigenvalues at each frequency.

Modal solution in the frequency domain

The modal solution in the frequency domain of the discrete equation of motion parallels that of the continuous model. First, we transform the equation of motion into the frequency-wavenumber domain. Second, for every frequency in the analysis, we solve the homogeneous equation (no external forces) and obtain the modes that propagate in the plate at that given frequency. Next, we find the solution of the inhomogeneous equation as a linear combination of the modes previously computed and invert the

solution into the frequency-space domain by means of contour integration, as alluded to previously. Finally, the inversion from frequency into time domain must be performed numerically, by means of either numerical integration techniques or using the Discrete Fourier Transform. A further appeal of the Thin Layer Method is that it accepts complex frequencies, and therefore it allows for easy implementation of the *Exponential Window Method*[20].

The spectral decomposition of the *Dynamic Stiffness Matrix*, that is the computation of the natural modes in the plate by solving the eigenvalue problem given by the homogeneous equation, is a critical step in the TLM, both from the point of view of numerical stability and computational effort.

In the anti-plane case, taking the frequency ω as a parameter, we obtain a linear eigenvalue problem

$$(\alpha \mathbf{A} + \mathbf{C})\bar{\mathbf{U}} = 0 \tag{3.14}$$

In this equation $\alpha = k^2$ and the matrix $\mathbf{C} = \mathbf{G} - \omega^2 \mathbf{M}$ is known.

The subject of linear eigenproblems is most relevant to Structural Dynamics, among other fields, and is extensively treated in the literature. Apart for the need of complex algebra, equation (3.14) does not present any mayor complication. Its solution yields N eigenvalues α_i and N eigenvectors; thus, a total of $2N$ values for k_j. For points to the right of the load, we select only those values k_j which have a negative imaginary part if the eigenvalue is complex, or if the eigenvalue is real, the real part with a sign such that the group velocity remains positive. That is, we are interested only in those waves that decay with distance to the source or that propagate (or more precisely, carry energy) away from it.

For the in-plane case, taking ω as a parameter gives a complex quadratic eigenvalue

$$(k^2 \mathbf{A} + \mathrm{i}k\mathbf{B} + \mathbf{C})\bar{\mathbf{U}} = 0 \tag{3.15}$$

The quadratic eigenvalue problem appears in various Structural Dynamics problems, e.g. in the analysis of viscously damped systems and in fluid-structure interaction; however, in our case the matrices are complex and not hermitian, which somehow complicates the solution.

A common solution strategy consists in transforming the quadratic eigenproblem into a linear eigenproblem by addition of a trivial equation, namely

$$k\begin{bmatrix}\mathbf{A} & 0\\ 0 & -\mathbf{C}\end{bmatrix}\begin{pmatrix}k\bar{\mathbf{U}}\\ \bar{\mathbf{U}}\end{pmatrix}+\begin{bmatrix}\mathrm{i}\mathbf{B} & \mathbf{C}\\ \mathbf{C} & 0\end{bmatrix}\begin{pmatrix}k\bar{\mathbf{U}}\\ \bar{\mathbf{U}}\end{pmatrix}=\begin{pmatrix}0\\ 0\end{pmatrix} \tag{3.16}$$

This approach, however, doubles the dimension of the problem and, with the exception of small problems, it incurs into a significant penalty in memory and computational time.

If stresses near the point of application of loads are to be adequately represented with the discrete model, it will necessarily include many layers, which makes this approach ineffective. For an efficient combination of the Green's functions given by the TLM and the *Boundary Element Method*, we need a fast algorithm to solve (3.15). In the present work, the authors used *Inverse Iteration with shift by Rayleigh quotient* especially tailored for the problem at hand. This approach allows solving efficiently in standard PC eigenproblems with thousands of equations. This quadratic eigenvalue problem yields twice as many eigenvalues as there are equations. The eigenvalue selection criteria remain the same as those for the anti-plane case.

Green's functions in the TLM

Green's functions for line loads

Once the required eigenvalues and eigenvectors have been computed, the displacement in the plate are given by the following expressions:

- Anti-plane case

$$\mathbf{V}=\frac{1}{2\mathrm{i}}\Phi^{\mathrm{L}}\,\mathbf{E}^{\mathrm{L}}_{|\lambda|}\,\mathbf{K}_{\mathrm{L}}^{-1}\,\Phi^{\mathrm{L}^{\mathrm{T}}}\mathbf{P} \tag{3.17}$$

- In-plane case

$$\begin{pmatrix} \mathbf{U} \\ \mathbf{W} \end{pmatrix} = \frac{1}{2\mathrm{i}} \begin{bmatrix} \Phi_x^{\mathrm{R}} \mathbf{E}_{|x|}^{\mathrm{R}} \mathbf{K}_{\mathrm{R}}^{-1} \Phi_x^{\mathrm{R}\,\mathrm{T}} & \mp \Phi_x^{\mathrm{R}} \mathbf{E}_{|x|}^{\mathrm{R}} \mathbf{K}_{\mathrm{R}}^{-1} \Phi_z^{\mathrm{R}\,\mathrm{T}} \\ \pm \Phi_z^{\mathrm{R}} \mathbf{E}_{|x|}^{\mathrm{R}} \mathbf{K}_{\mathrm{R}}^{-1} \Phi_x^{\mathrm{R}\,\mathrm{T}} & -\Phi_z^{\mathrm{R}} \mathbf{E}_{|x|}^{\mathrm{R}} \mathbf{K}_{\mathrm{R}}^{-1} \Phi_z^{\mathrm{R}\,\mathrm{T}} \end{bmatrix} \begin{pmatrix} \mathbf{P}_x \\ \mathbf{P}_z \end{pmatrix} \quad \begin{matrix} x > 0 \\ x < \end{matrix} \tag{3.18}$$

In these expressions

$$\begin{aligned} \Phi &= \left[\phi_1, \phi_2, \ldots \phi_j, \ldots \right] \\ \mathbf{E}_{|x|} &= diag\left\{ \exp\left(-\mathrm{i} k_j |x| \right) \right\} \\ \mathbf{K} &= diag\left\{ k_j \right\} \end{aligned} \tag{3.19}$$

The super-indices R and L indicate whether the eigenvalues (k_j) and the eigenvectors (ϕ_j) are those of the anti-plane case (L, for Love waves) or the in-plane case (R, for Rayleigh waves), the sub indices x and z indicate whether the horizontal components or the vertical components of the eigenvectors are to be used, and the loads are applied at $x = 0$. Also, the eigenvectors must satisfy the following normalization conditions

$$\begin{aligned} \phi_{yj}^{\mathrm{T}} \mathbf{A} \phi_{yj} &= \mathbf{I} \\ \mathbf{K}_{\mathrm{R}} \begin{pmatrix} \phi_{xj} \\ -\phi_{zj} \end{pmatrix}^{\mathrm{T}} \mathbf{A} \begin{pmatrix} \phi_{xj} \\ \phi_{zj} \end{pmatrix} \mathbf{K}_{\mathrm{R}} - \begin{pmatrix} \phi_{xj} \\ -\phi_{zj} \end{pmatrix}^{\mathrm{T}} \mathbf{C} \begin{pmatrix} \phi_{xj} \\ \phi_{zj} \end{pmatrix} &= 2\mathbf{K}_{\mathrm{R}}^2 \end{aligned} \tag{3.20}$$

Equations (3.17) and (3.18) come directly from equations (48) and (47) in the report *An Explicit Solution for the Green Functions for Dynamic Loads in Layered Media*[26]. Equation (3.18) differs however slightly from the one in the report, due to some implicit imaginary factors that are introduced in the report equations for the in-plane cases.

The Green's functions for line load are obtained simply by introducing unit loads in the expressions above.

Green's functions for line dipoles

The Green's functions for dipoles are obtained directly from the Green's functions for line loads by simple differentiation[18] (see also chapter 1). Special care must be taken

though when the differentiation is along the layering axis, as one must be careful to differentiate with respect to the point of application of the load.

Stresses in the TLM

In the application of the Traction Boundary Element Method (TBEM) to crack problems, the accurate evaluation of stresses is of utmost importance, as they are the kernels in the *Boundary Integral Equation*. The straightforward and most common approach to compute the stresses is to apply the traction operator to the discrete solution for displacements. This is certainly the standard way in FE analysis. However, it is widely acknowledged that the accuracy of the stresses will in general be less than that of the displacements, as the accuracy of discrete approximations generally decreases with differentiation.

In the TLM, we may distinguish between stresses on vertical planes and stresses on horizontal planes. While both cases could be treated with the traction operator, there is an alternative and more accurate way of computing the stresses in horizontal layers, which is the use of the so-called *consistent stresses*. These are the forces at the interfaces that balance out the combination of inertia forces and residual forces within the layer.

Kausel[26] gives expressions for stresses on both horizontal planes and vertical planes, in terms of the corresponding eigenvalues and eigenvectors, for the linear interpolation. Because we are looking at cracks parallel to the layering, we focus on the *consistent stresses* on horizontal planes, which are

- Anti-plane case

$$\begin{pmatrix} \tau_m \\ -\tau_{m+1} \end{pmatrix} = \sum_{l=1}^{N} \mathbf{K}_{ml} \begin{pmatrix} \phi_y^{m,l} \\ \phi_y^{m+1,l} \end{pmatrix} \frac{1}{2\mathrm{i}} \frac{\phi_y^{n,l}}{k_l^{\mathrm{L}}} \exp\left(-\mathrm{i}k_l^{\mathrm{L}}|x|\right) + \delta(x)\mathbf{A}_m \sum_{l=1}^{N} \begin{pmatrix} \phi_y^{m,l} \\ \phi_y^{m+1,l} \end{pmatrix} \phi_y^{n,l} \qquad (3.21)$$

- In-plane case

$$\begin{pmatrix} \tau_m \\ -\sigma_m \\ -\tau_{m+1} \\ \sigma_{m+1} \end{pmatrix} = \sum_{l=1}^{2N} \mathbf{K}_{ml} \begin{pmatrix} \phi_x^{m,l} \\ \mathrm{i}\phi_z^{m,l} \\ \phi_x^{m+1,l} \\ \mathrm{i}\phi_z^{m+1,l} \end{pmatrix} \alpha_{nl} \exp\left(-\mathrm{i}k_l^{\mathrm{R}} x\right) + S_n \quad x \geq 0 \tag{3.22}$$

In these expressions, $\mathbf{K}_{ml}$ is the *dynamic stiffness layer* of the layer m evaluated at wavenumber k_l, $\alpha_{nl} = \phi_x^{nl} / \left(2\mathrm{i}k_l^{\mathrm{R}}\right)$ for horizontal loads or $\alpha_{nl} = \phi_z^{nl} / \left(2k_l^{\mathrm{R}}\right)$ for vertical loads and the singularity term is given by

$$S_n = \delta(x)\mathbf{A}_m \sum_{l=1}^{2N} \begin{Bmatrix} \phi_x^{m,l} \\ 0 \\ \phi_x^{m+1,l} \\ 0 \end{Bmatrix} \phi_x^{n,l} \qquad \text{for horizontal loads} \tag{3.23}$$

$$S_n = -\delta(x)\mathbf{A}_m \sum_{l=1}^{2N} \begin{Bmatrix} \phi_z^{m,l} \\ 0 \\ \phi_z^{m+1,l} \\ 0 \end{Bmatrix} \phi_z^{n,l} \qquad \text{for vertical loads} \tag{3.24}$$

Accuracy and Convergence of the discrete solution

In order to better assess the suitability of the Discrete Green's functions for their application to BEM, and to establish within which limits they perform as required in the BEM, we carried out an exhaustive comparison between discrete solutions and continuous modal solutions. The comparison was made in terms of dispersion curves, displacements and stresses, and the discrete model showed great potential. In the following, we highlight some of the conclusions:

1. Quadratic layers gave consistently better accuracy than linear layers, for the same total number of degrees of freedom, both in terms of dispersion curves and of displacements and stresses. The improvement of using cubic layers vs. quadratic layers was very small.

2. For the anti-plane case, the first half of the dispersions curves computed with the discrete model accurately matched those in the continuous model. For the in-plane problem, the percentage of accurate modes decreased to about 33%. The higher modes were progressively being affected by the discretization. Thus, enough layers are needed to ensure that the accurate modes suffice for representing the displacement and stress fields.

3. Despite their mismatch with the continuous modes, all the discrete modes are necessary for a proper representation of displacements and stresses at short epicentral distances. In fact, at very short epicentral distances the rate of convergence of the discrete solution was substantially better than that of the continuous model. That is, with the same number of modes in both, the discrete solution was more accurate. This proves that the discrepancy in the high modes does not imply a less accurate Green's function.

4. For the same number of layers, displacements were more accurate than stresses. Among these, consistent stresses were more accurate and converged faster to the true solution than regular stresses. This was an expected result, as consistent stresses are not computed through differentiation, but instead using the discrete equilibrium equation.

5. As expected, the Green's functions for dipoles were worse than those for line loads. The differentiation step needed to go from line loads to dipoles reduces accuracy.

6. When selecting the number of layers to model a plate, the limiting factor is the accuracy of the stresses in the near field due to a dipole, particularly in the immediate neighborhood of the source. Convergence analyses showed that some ten to fifteen quadratic layers per shortest wavelength are needed for an accurate representation of the stresses.

Two final notes on the use of consistent stresses: First, because the usual interpolation functions are not continuous in slope across the interfaces, stresses computed via differentiation will present discontinuities at the interfaces, and the results will depend on whether the top or bottom layers are used to compute them. Consistent stresses, on the

other hand, do not depend on the layer used to compute them. Second, a minor disadvantage of consistent stresses is that they can only be computed at the interfaces. However, if stresses within the layers were required, we could always interpolate with a continuous model just for that layer. Given a good solution for the interface displacements, this approach produced very reliable results.

Convergence analysis

We present here several figures to support our conclusions. These figures show the error of fundamental solutions in the frequency-space domain for either displacements or stresses at different frequencies and with different discrete models (different type and number of layers). The benchmark for the discrete solutions are the fundamental solutions for continuous models developed in the previous chapter.

In Figure 3-2, we consider displacements at three different depths (top surface, center of plate and a point in between) and three different epicentral distances (0.1, 0.5 and 1.5 times the thickness of the plate) in a free plate subject to an anti-plane line load. We use both linear and quadratic discrete models to compute the displacements and we plot the relative error of the absolute displacement as a function of the total number of nodes in the model. For equal number of nodes, the linear model has twice as many thin layers as the quadratic model; still, the total number of degrees of freedom and the dimension of the eigenproblem is the same as these are given by the number of nodes. This figure shows clearly that the quadratic models (thick lines) converge faster to the continuous solution than the linear ones (thin lines); therefore, for equal number of nodes the quadratic models give more accurate results than the linear ones.

Figure 3-3 compares consistent vs. non-consistent stresses for the anti-plane problem. We consider here the same plate, frequency and epicentral distances than above, and we move the output station on the surface a little inside the plate (stresses vanish at the surface), to study the discrete stresses. Using only quadratic TLM models, we compute consistent and non-consistent stresses and plot the relative error of their absolute value once again as a function of the total number of nodes. As already mentioned, consistent stresses (thick line) show unambiguously superior performance.

Finally, Figure 3-4 to Figure 3-7 focus on the stresses at the abscissa of the load. We present here average stresses rather than point stresses. The reason being that for the application of the TBEM, the relevant quantities are the integrals of the stresses multiplied by the interpolation functions over the boundary elements and that the interpolation function for uniform elements is a constant value of one.

Figure 3-4 shows the relative error of the modulus of the average shear stress for three different depths (0.02, 0.06 and 0.1 from the top) in a 0.2-thick vertically restrained plate subject to a horizontal line load on its top surface, as a function of the number of nodes. Figure 3-6 shows the same stresses for a different frequency. Figure 3-5 and Figure 3-7 show the corresponding absolute error in the phase.

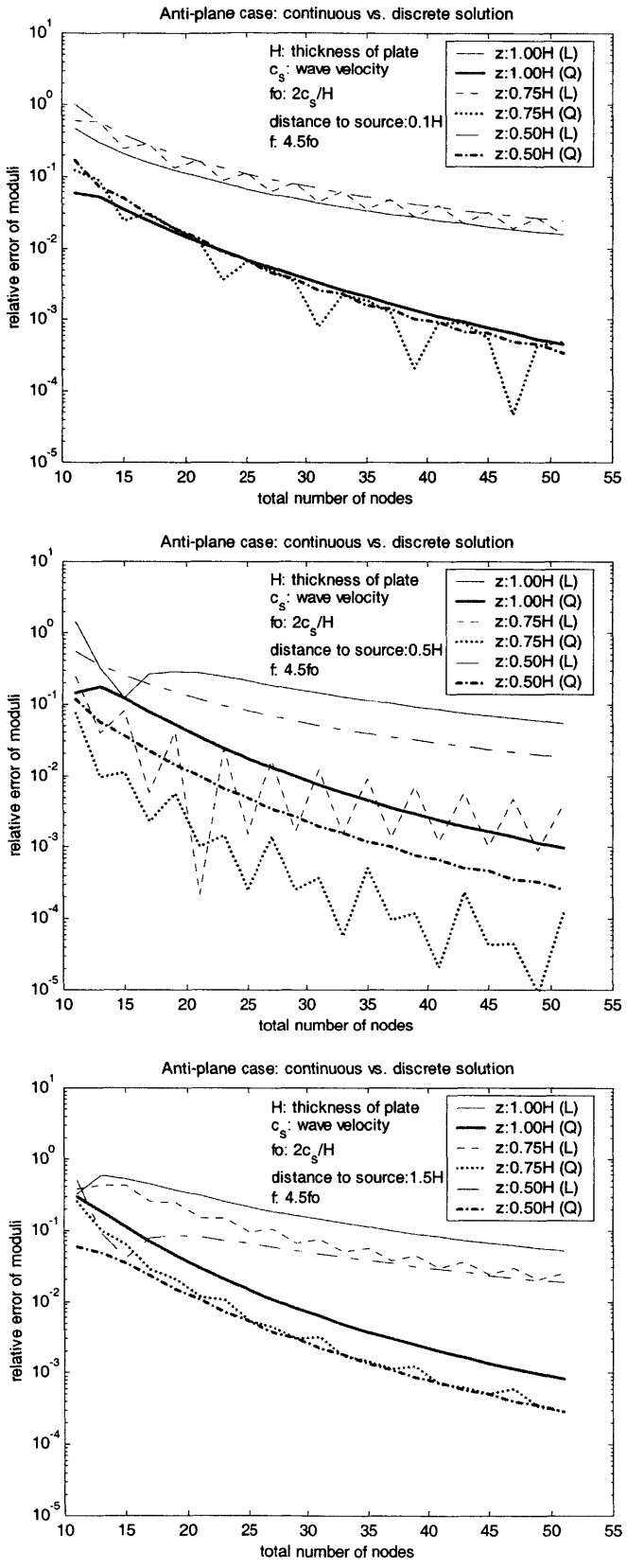

Figure 3-2: Convergence of linear vs. quadratic discrete models

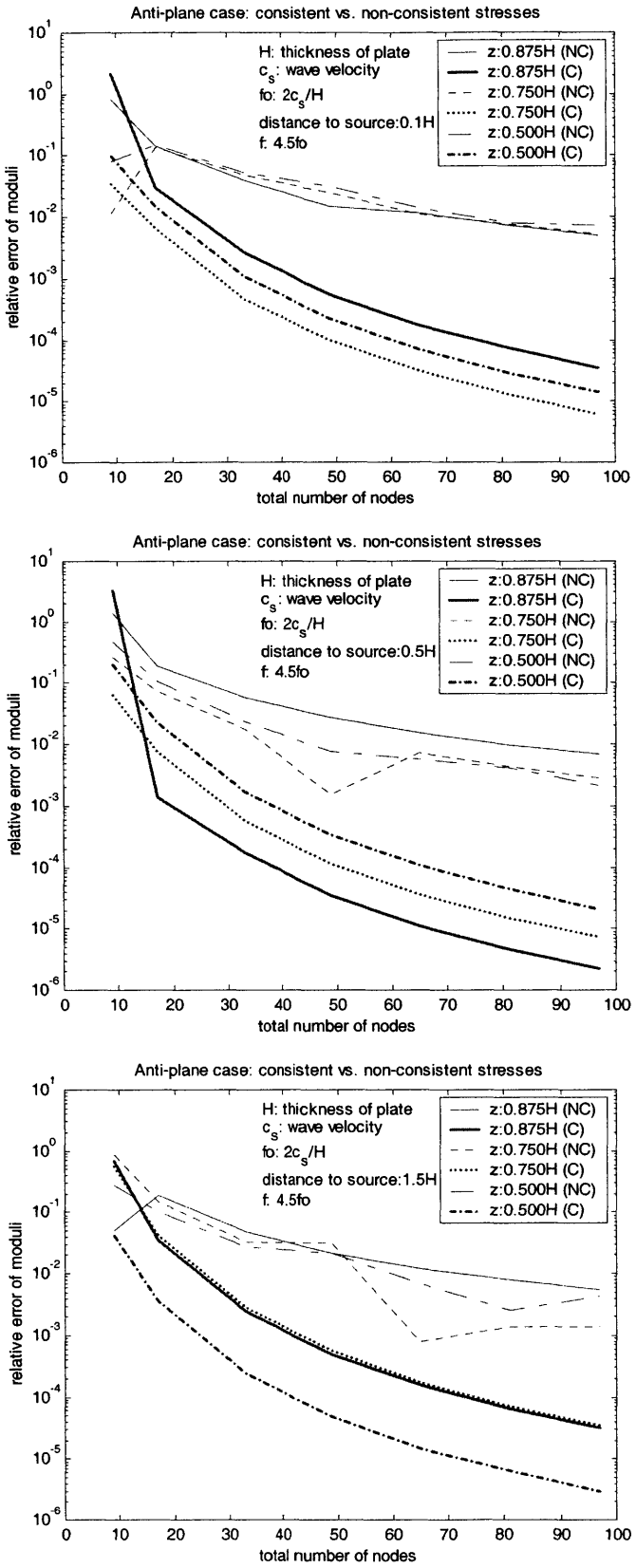

Figure 3-3: Convergence of consistent vs. non- consistent stresses

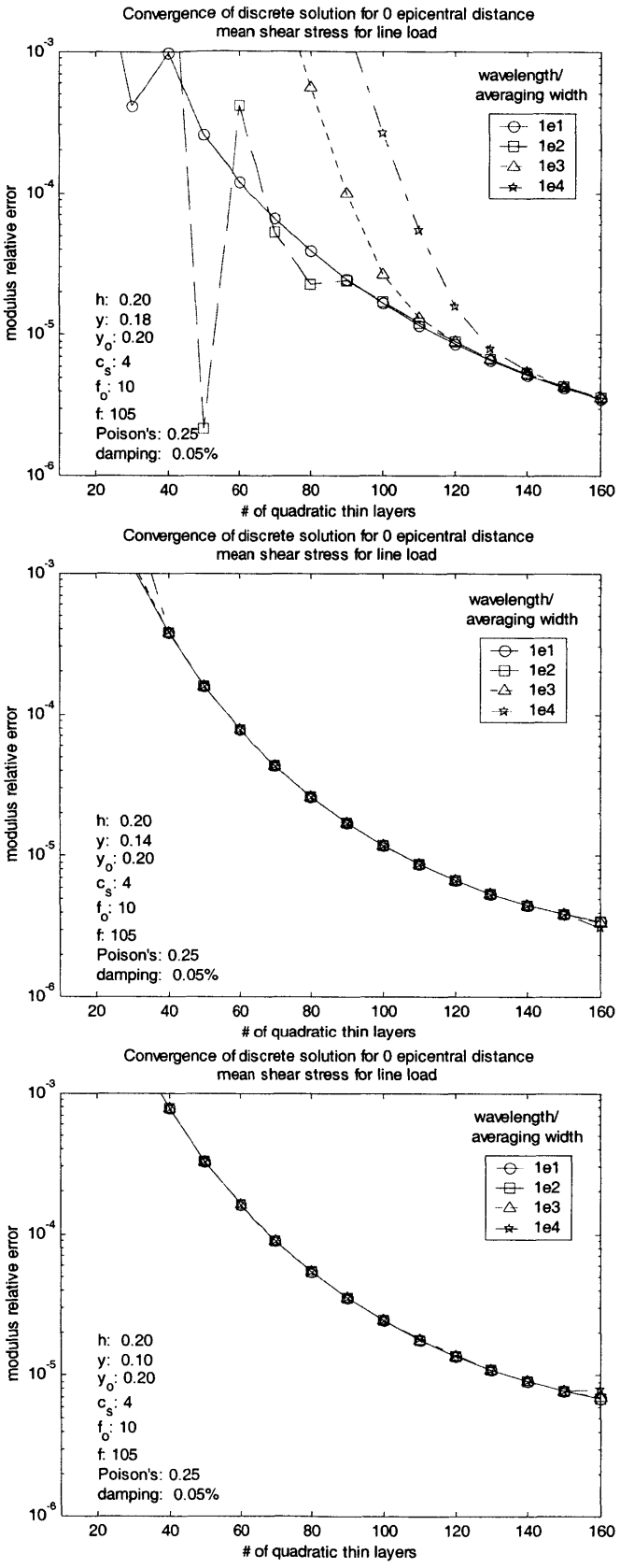

Figure 3-4: Convergence of mean stress at the abscissa of the load (modulus)

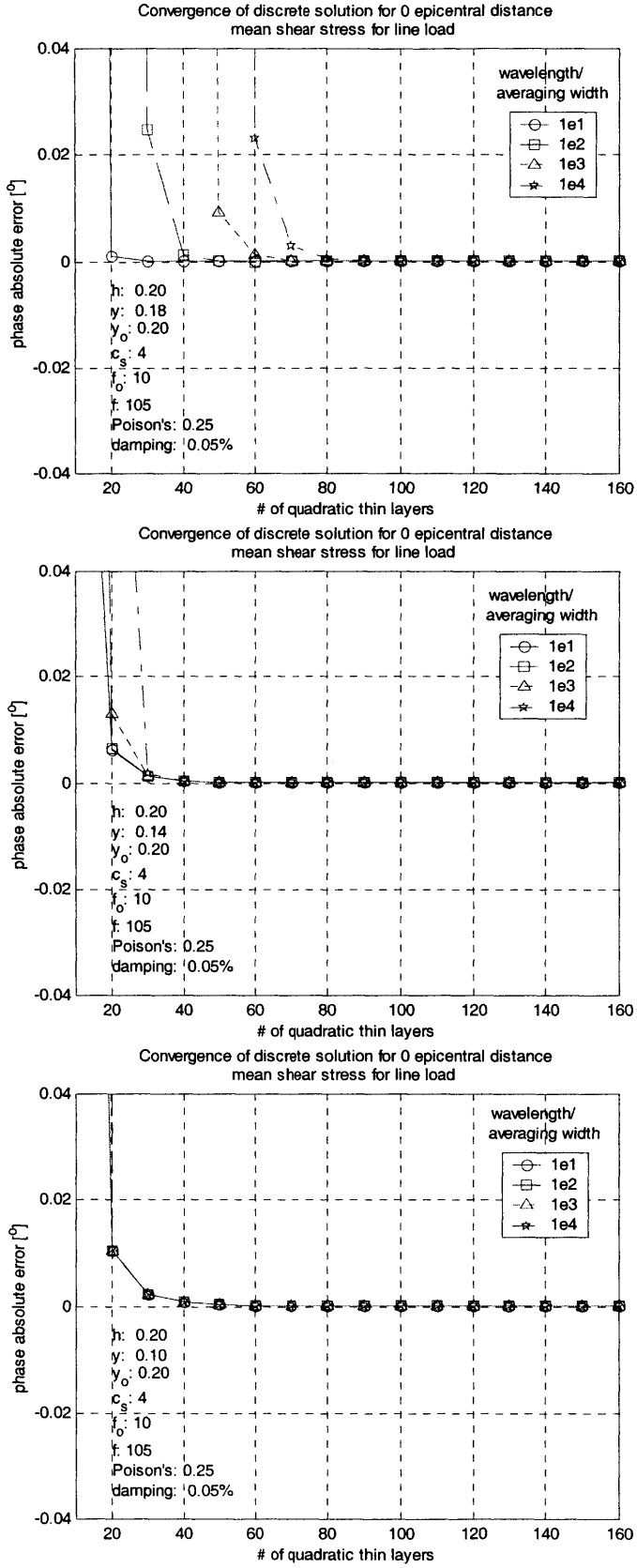

Figure 3-5: Convergence of mean stress at the abscissa of the load (phase)

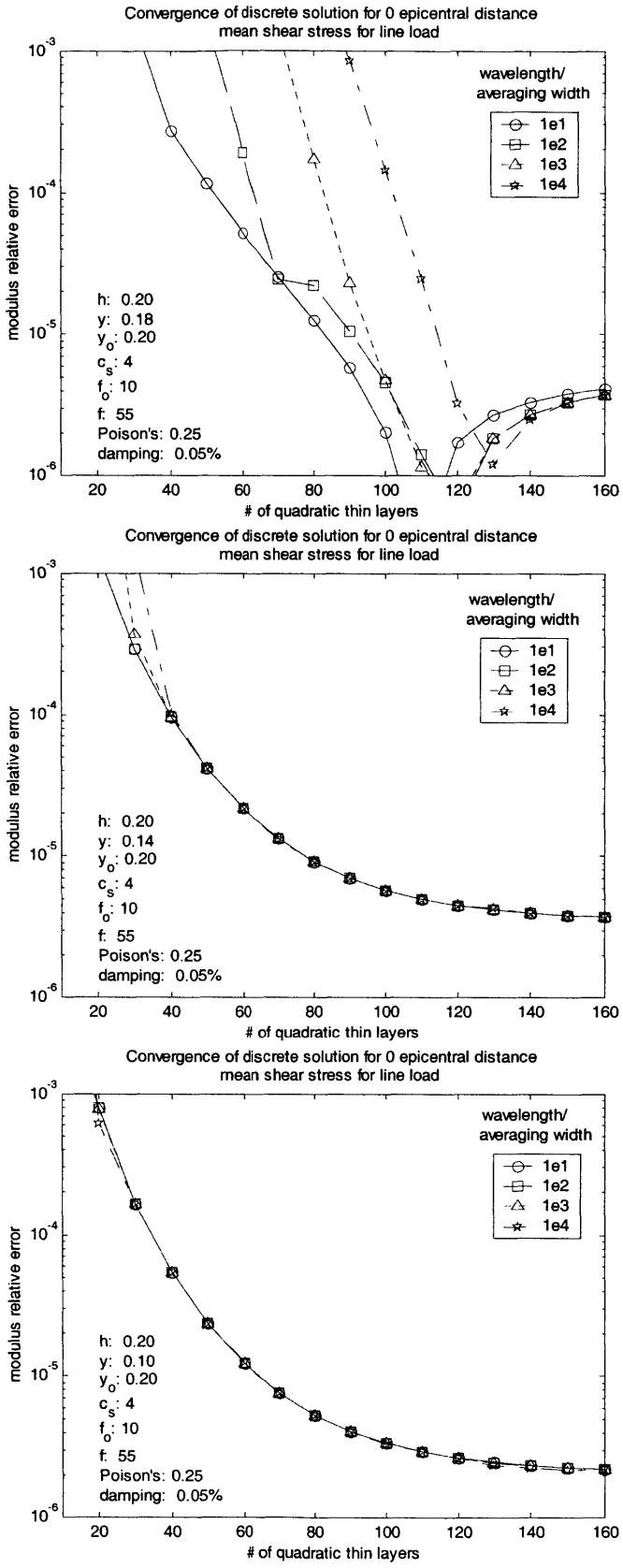

Figure 3-6: Convergence of mean stress at the abscissa of the load (modulus)

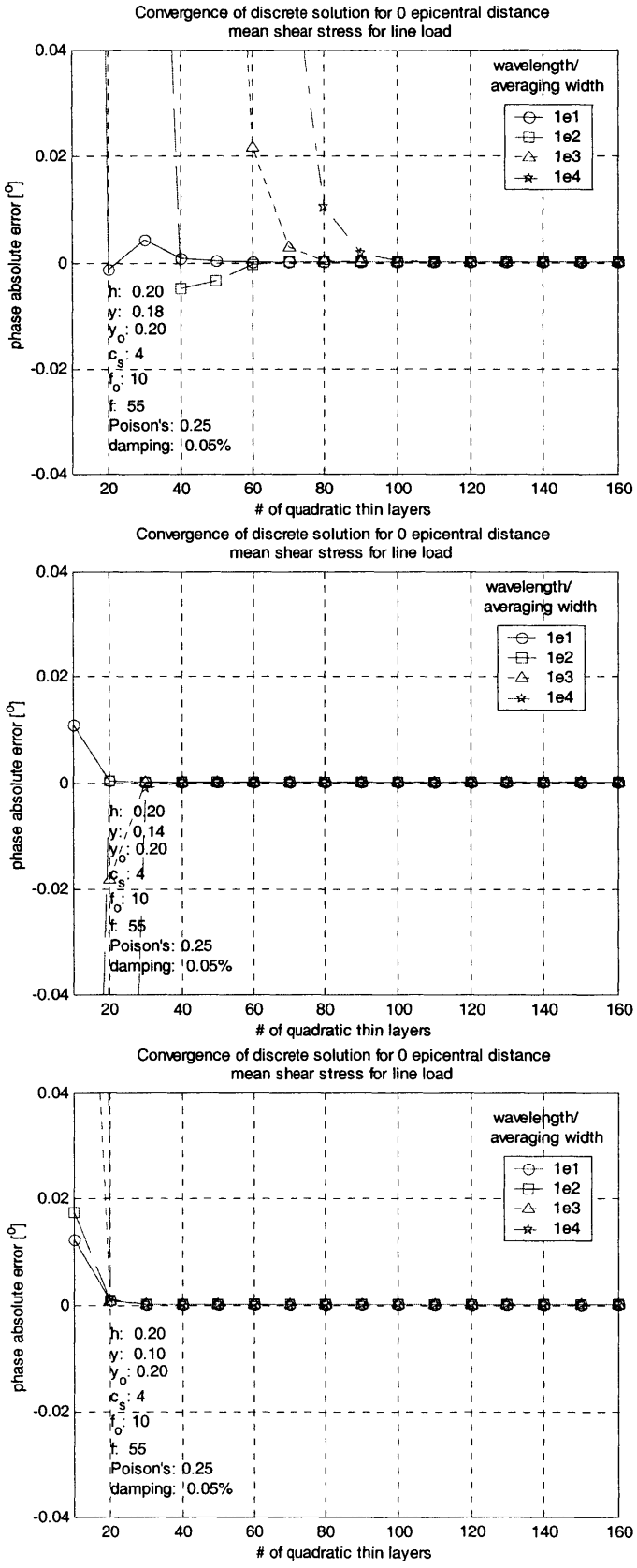

Figure 3-7: Convergence of mean stress at the abscissa of the load (phase)

Sample of solutions from the discrete model

In this final section of the chapter, we present a sample of fundamental solutions in the frequency-space domain for a 0.2 m. thick vertically restrained plate. Every figure has three graphics. The top and middle graphics plot respectively the real and the imaginary part of the response of the discrete model in dashed line, and they include also the response of the continuous model (exact response). The bottom graphic plots in continuous line the relative error of the modulus of the response (scale to the left of the plot), and in dashed line the absolute error of the phase in degrees (scale to the right of the plot). The horizontal axis in all plots represent the epicentral distance normalized by the thickness of the plate.

Figure 3-8, Figure 3-9 and Figure 3-10 show the displacements, shear stresses and normal stresses of the plate when subject to an harmonic horizontal line load of 50 kHz (10 times the first shear resonance of 5 kHz) on the surface. The response is evaluated one centimeter from the loaded surface. As expected, the response for stresses is slightly worse than the one for displacements.

Figure 3-11 shows shear stresses of the plate when subject to a pair of opposite harmonic horizontal loads of 50 kHz distant vertically by an infinitesimal amount (dipole). In this figure, we represent average-stresses, averaged over a width of two centimeters. Figure 3-12 is simply a zoom-in of Figure 3-11 in the proximity of the dipole.

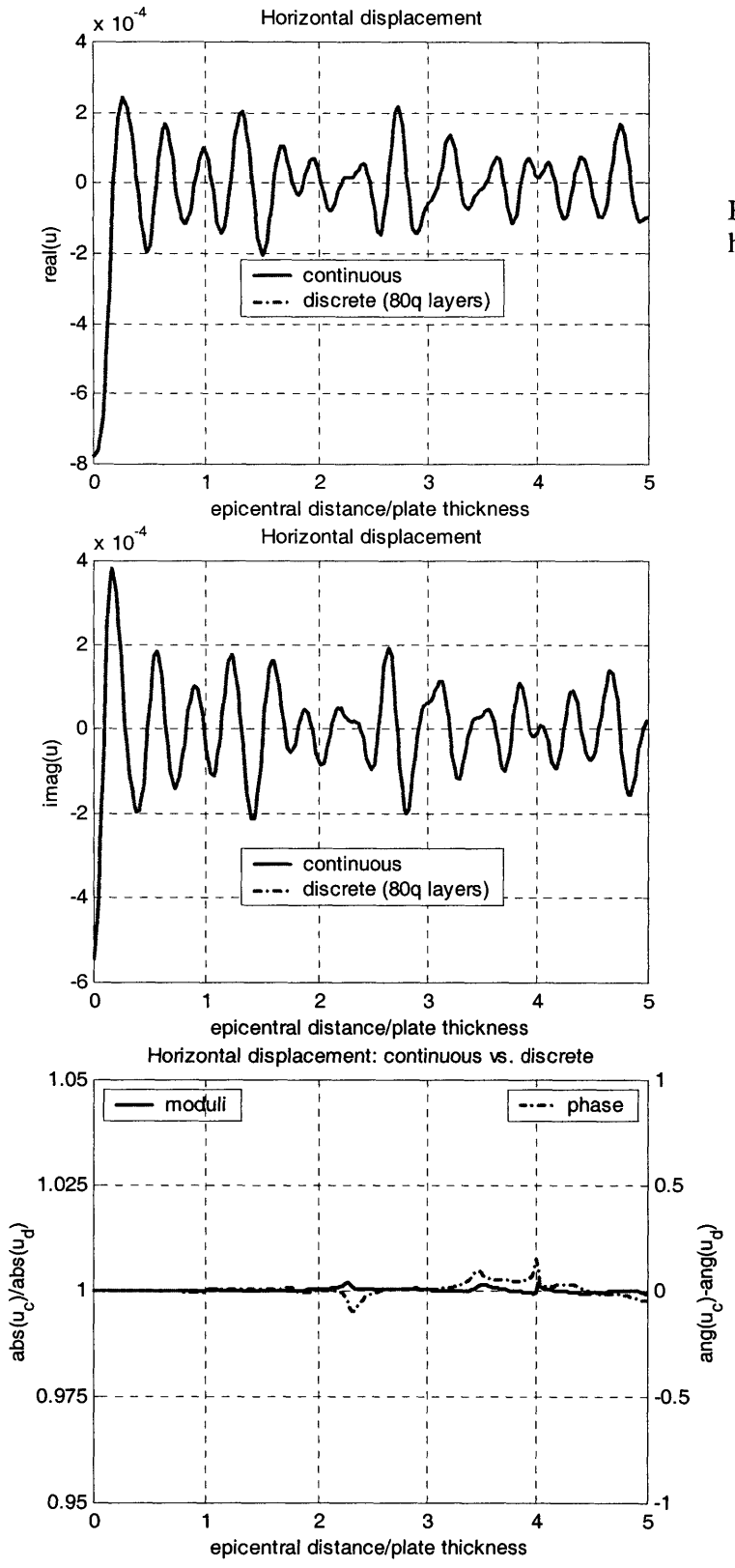

Homogeneous plate subject to horizontal harmonic uniform load at top

- Shear speed: 2 m/ms
- Poisson's ratio: 0.25
- Frequency of load: 50 kHz
- Plate thickness: 20 cm
- Load thickness: 2 cm.
- Output depth: 1cm. from top
- Damping: 0.1 %
- Horizontal support at top and bottom (no vertical motion)

Figure 3-8: Displacements for line load

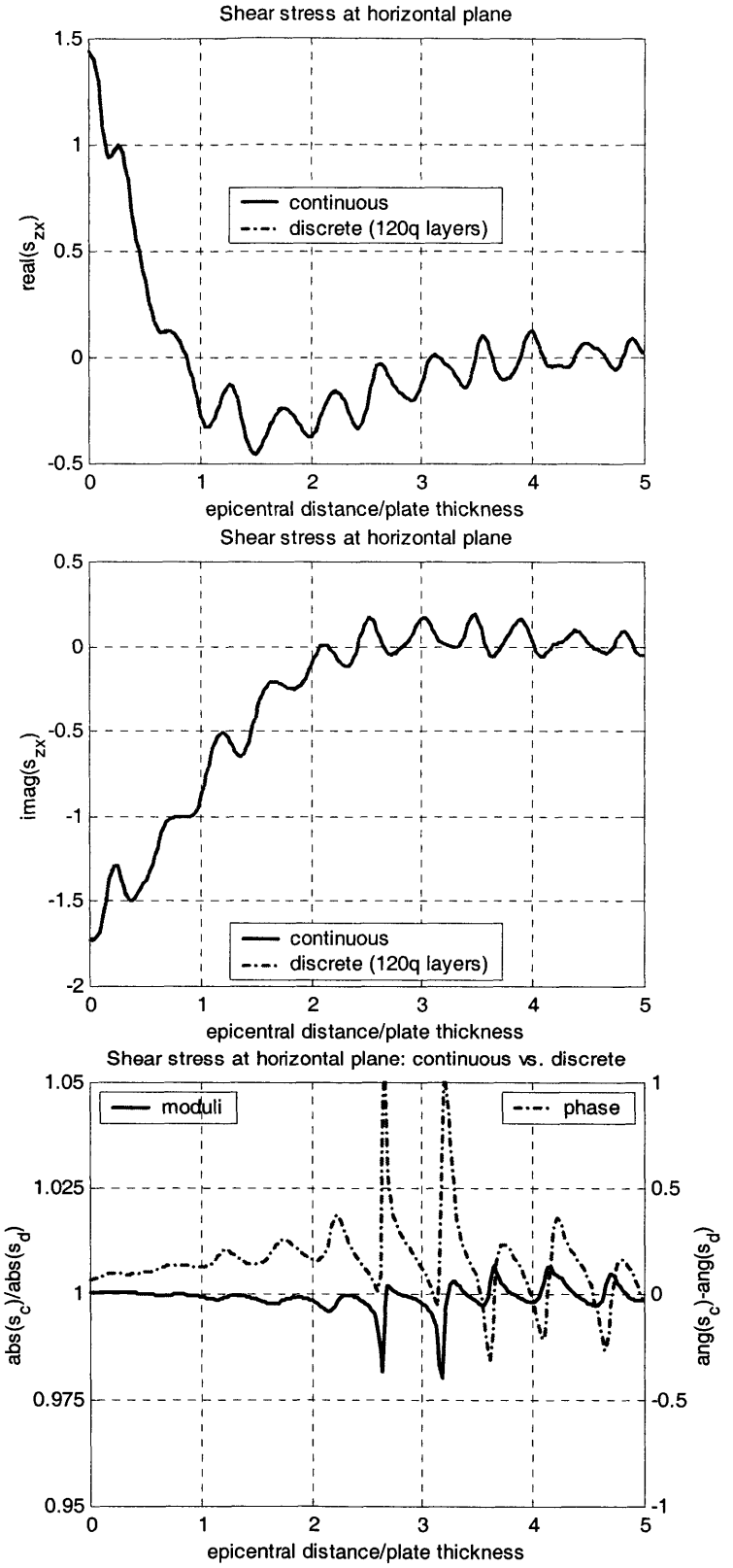

Figure 3-9: Shear stresses in horizontal plane for line load

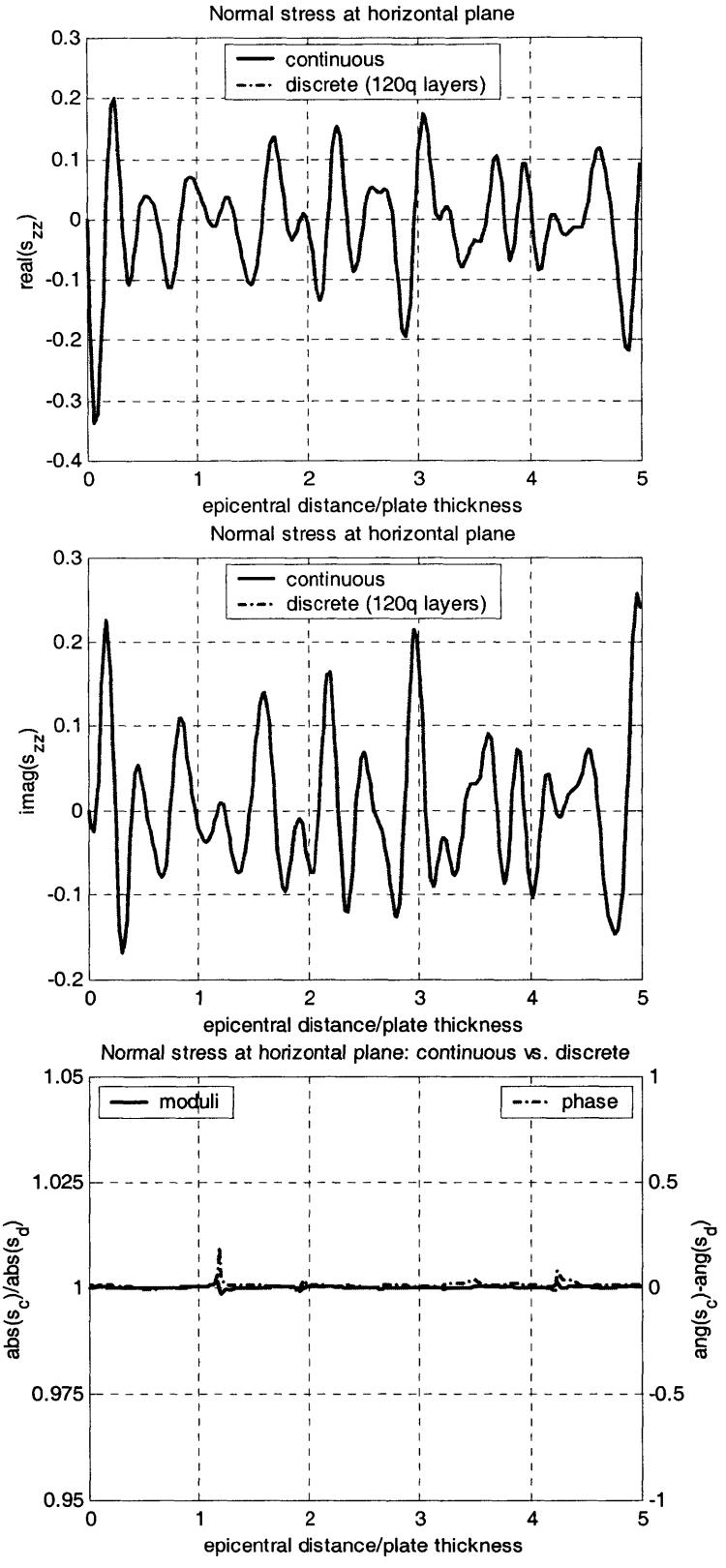

Figure 3-10: Normal stresses in horizontal plane for line load

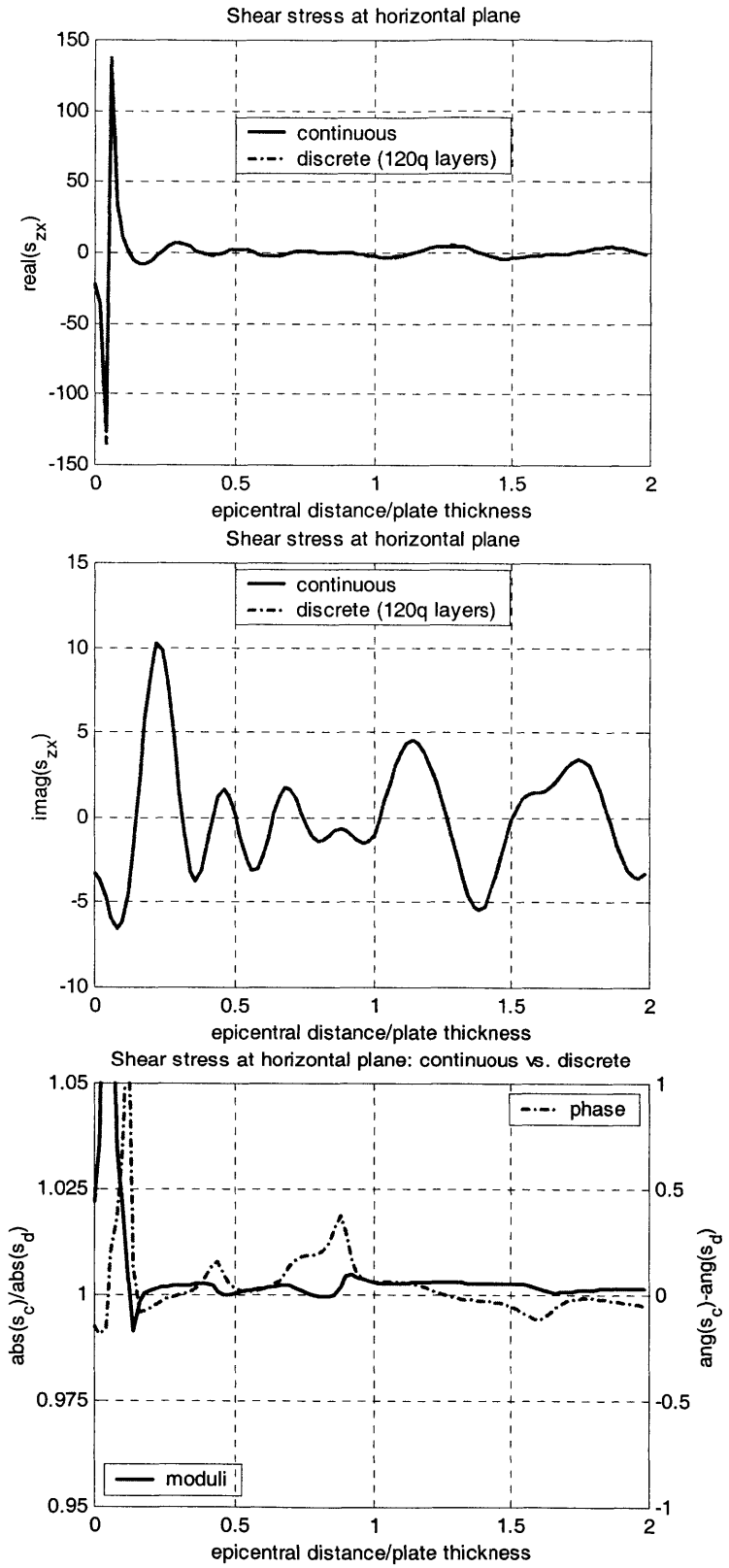

Homogeneous plate subject to horizontal harmonic uniform dipole two cm deep from top

- Shear speed: 2 m/ms
- Poisson's ratio: 0.25
- Frequency of load: 50 kHz
- Plate thickness: 20 cm
- Dipole thickness: 2 cm.
- Output depth: 2cm. from top
- Damping: 0.1 %
- Horizontal support at top and bottom (no vertical motion)

Figure 3-11: Shear stresses in horizontal plane for line dipole

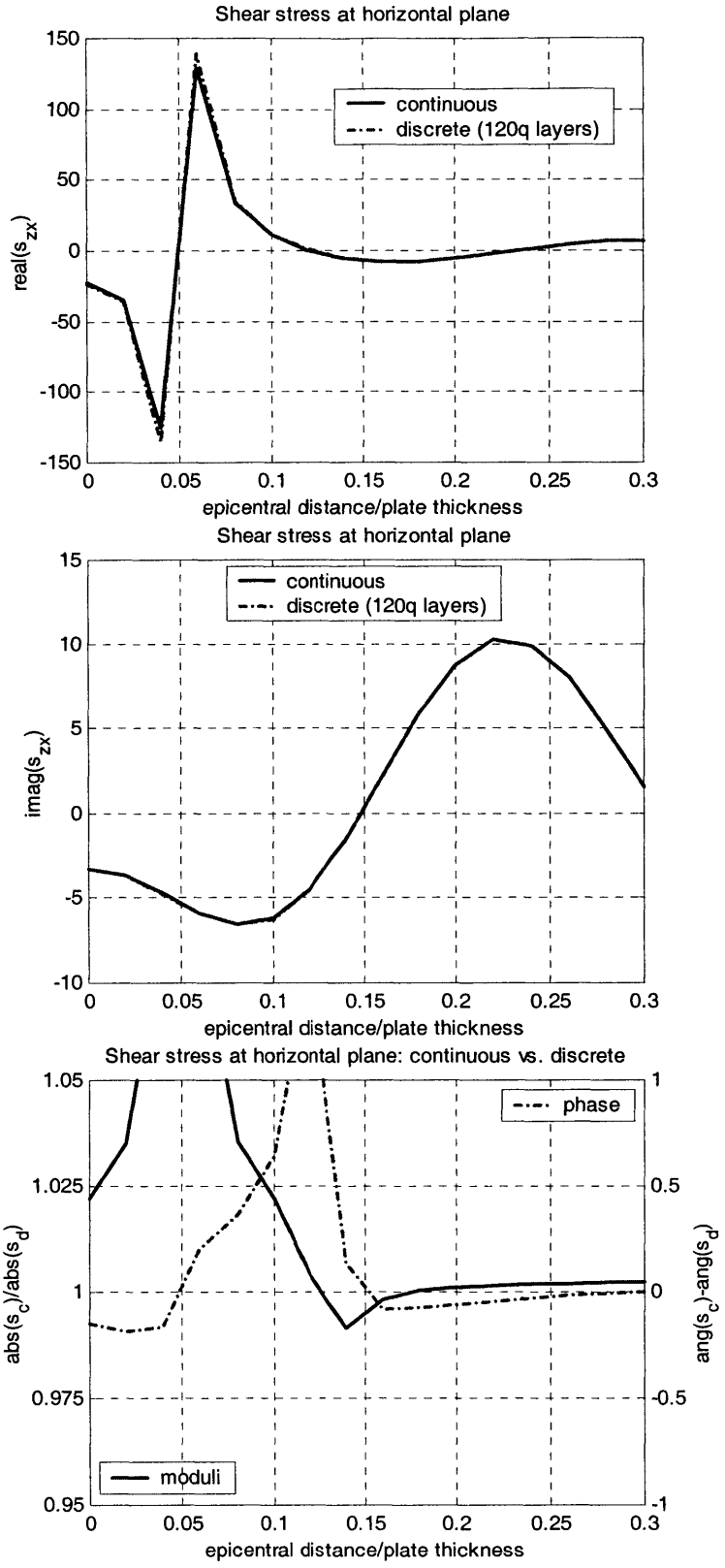

Figure 3-12: Shear stresses in horizontal plane for line load

Detecting cracks in laminated media

The main objective of the mathematical model outlined in the first three chapters of this thesis is to provide a tool to carry out parametric analysis of plates with known material defects. The results of these analyses provide in turn considerable insight into the dynamic response of delaminated plates. As part of the research that led to this dissertation, we developed a computer code capable of modeling the scattering of elastic waves in delaminated layered plates. This code was written using C++ and FORTRAN and compiled for use in a standard PC with Windows OS, implementing the numerical tools outlined in the previous chapter. We used the compiled code extensively to simulate various cracks in different plates, and to evaluate approaches to Acoustic Non Destructive Evaluation (NDE). We created also computer simulations (videos in mpg format) of wave scattering in layered plates.

Sounding and *impact-echo* are probably the two best-known NDE acoustic techniques used in current practice to detect delaminations in concrete walls and decks. The *sounding* technique consists simply in striking the surface of the concrete and listening for hollow sounds, which are usually related to shallow delaminations. The *impact-echo* searches for echoes in the dynamic response of the concrete surface that convey information about discontinuities in the structure's interior. However, these two methods rely on very simple physical interpretations that are applicable only in the immediate vicinity of a defect. Thus, they have significant limitations in their ability to detect delaminations.

In this thesis, we make a parametric study of the response of a plate subjected to an impact load centered above a crack. We explore cracks of different sizes and at various depths. Furthermore, we interpret the results from the point of view of the simple models in *sounding* and *impact-echo*, and assess the limitations of these conventional techniques.

Later on, we assess the response of the plate from a completely different perspective. When excited dynamically, plates act as wave-guides directing the energy flow within it boundaries, parallel to the layering. The total response of the plate can be decomposed into a linear combination of individual cross-sectional motion profiles called *guided*

modes. The use of arrays of sensors and array processing techniques allows unraveling the surface response of the plate and expressing it in terms of the principal wave modes.

The presence of a crack affects the relative contribution of each mode to the total response. Thus, it is possible to detect delaminations in a plate by means of an array of sensors providing information about the propagating modes. The mathematical model that is the basis for this approach is valid anywhere on or within the plate, in contrast to the conventional approaches that are valid only inn the immediate vicinity of a defect. Therefore, it can detect cracks at distance from the source or located beyond the array area.

In the fifth chapter, we compare the modal components for cracks of different sizes and locations and show the significant impact that the presence of a crack can have on the response of the plate, both locally and at a distance from the crack. We also demonstrate the existence of mode conversion phenomena due to the crack.

Chapter 4 :

On sounding and the impact-echo method

Introduction

Various types of civil structures, such as walls, pavements, decks, slabs and pipes, can often be modeled as layered systems for the purpose of assessing how waves propagate in them, and how these waves can be used in turn to detect hidden defects. A frequent pathology in the structural integrity of these systems is the development of delaminations (i.e. cracks) that run parallel to the layering, either within or between the material layers. Such delaminations can grow significantly in size before manifesting themselves on the surface, and thus remain largely invisible from the exterior. These defects can significantly affect the structural performance of structural systems and may eventually lead to costly failures. Hence, early detection of incipient defects could result in significant savings in the maintenance of these infrastructures, both by preventing the progress of decay as well as the potential costs of sudden failure. A reliable detection of such delaminations is an important objective in the Non Destructive Evaluation (NDE) of civil structures, which has been the focus of intensive research.

In the last couple of decades, several NDE techniques have been developed based on infrared thermography, ground penetrating radar or acoustic methods. While all the methods present advantages and disadvantages, the latter group of methods, which are based on the use of transient stress waves to study cracks and voids in structures, has shown considerable potential for the detection of delaminations in plate-like systems. The principal advantages of the wave-based methods are their lack of sensitivity to site conditions such as temperature and humidity and their potential for rapid deployment and ease of use. Their main drawback, on the other hand, is that the transient elastic response of plate-like systems involves many different types of waves so that the response signatures are, in general, difficult to interpret. Acoustic methods have been researched in concrete structures both for detecting anomalies and for estimating in-situ mechanical properties.

A first classification of acoustic techniques divides them into direct and indirect methods. In the direct method, a transient pulse is introduced on one face of the test subject and the response is measured on the other side; thus, there is a direct transmission path from the

input to the output. However, if only one side is accessible, as often happens, the source and the receiver must be placed on the same face, in which case there is no direct path other than that immediately below the surface. Inner defects must then be detected via reflections, in which case the methods are called indirect, and the interpretation of the wave signatures is far more complicated. Among the existing indirect acoustic methods, the sounding method and the impact-echo (or pulse-echo) method are the best known.

In the sounding method (sometimes called chain-dragging method), the surface of the concrete is struck with a metal object, such as a hammer or a chain. When the percussion takes place above a shallow delamination, a hollow sound can be heard which reveals the presence of the void. This sound relates to the bending modes of the concrete mass above the delamination, which acts like a clamped plate. Sounding relies on local bending modes due to delaminations, which greatly influence the response for shallow delaminations. However, the bending response decreases as the delamination depth increases. Also, because no instruments are used, the delamination cannot be sized accurately.

In the impact echo method, a brief impact is applied to the concrete with a hammer, which generates broadband signals whose Fourier amplitude spectra contain peaks at frequencies that relate to the inner structure. These frequency peaks are the result of echoes at material discontinuities such as the bottom of the plate, but most importantly, they are the manifestation of reflections taking place at delaminations and voids. By striking immediately above a delamination, it is possible to measure its echo. The impact method can run into problems for shallow delaminations, because their detection requires very high frequencies, which are hard to excite and record.

The study of the elastic response of layered plates, either with or without cracks, is of interest for the development and application of acoustic methods in general, and relevant to the two methods cited above in particular. In the bibliography, we find several numerical and experimental studies that deal with this and other similar problems. Sansalone and Carino[30,31] have used finite element methods and time numerical integration to simulate the response of finite plates with various layers and different cracks, and they have also performed several laboratory and field studies. Sack and

Olson[32] have published interesting application of the impact-echo method to bridge decks and buried concrete pipes. More recently, Toutanji[33] published some interesting laboratory results as well.

However, most of the work mentioned above has focused on assessing the potential of the acoustic methods to detect delaminations, and not on the limitations of the indirect acoustic methods. Thus, the question of how the size and depth of the delaminations affects the response signatures and what limits there are to their detection has not been completely answered yet. For this reason, we address this problem herein by carrying out parametric analyses for the diffraction of waves in delaminated layered plates. Using a numerical tool specially developed for this task, we model and analyze cracks of various sizes and depths below the surface. Some conclusions are drawn about the detectability of cracks under real test conditions.

Mathematical Model

Most of the numerical studies reported in the literature have relied on the use of Finite Element Techniques with direct time step integration. Resonance characteristics were then measured and analyzed by means of spectral estimation of the computed time histories (i.e. numerical signals).

In this study, we follow a different approach. In order to study the scattering due to delaminations in layered plates, we developed a plane strain (2D) numerical model based on a Boundary Integral Equation (BIE). The resulting BIE is solved using uniform Boundary Elements (BE). We formulated the BIE from the Somigliana Stress Identity, and not from the Somigliana Identity, as it is customary in standard Boundary Integral Methods, because the standard derivation degenerates when applied to crack problems[1]. With the formulation used, only one face of the crack needs modeling, and the unknowns are the jumps in displacement across the crack.

To compute the Green's functions that the Boundary Integral formulation requires, we use the Thin Layer Method[7,29] (TLM), which is a powerful numerical tool specially suited for the dynamic analysis of layered systems. The TLM basically performs a

discretization of the wave equation in the direction of the layering, while using other analytical techniques (usually Fourier Transformations) to solve the equations for the other coordinate directions. The advantage of using these functions rather than the full space fundamental solutions is that we need not model with BE the top and bottom surfaces (or even internal layering, if any), as they are automatically accounted for in the Green's functions. As a result, the dimensions of the matrices in the Boundary Element Method are drastically reduced. As for the expansion in the through-the-thickness direction, the discretization can be of any order; for the modeling of the plate, we have found quadratic thin layers to be optimal.

The main advantages of this numerical tool are

- Radiation conditions at infinity are automatically accounted for.
- Layering is not really an issue, as the TLM is especially suited for it.
- The number of boundary nodes (and thus of unknowns) is greatly reduced.

The two principal difficulties we encountered in developing the model were the hyper-singularity of the kernels in the BIE, and the solution of the eigenvalue problem required by the TLM formulation, which is a non-standard quadratic eigenvalue problem, when the models contained large number of thin layers. Both of these problems were satisfactorily dealt with.

Regarding the choice between a time domain solution versus a frequency analysis, we opted for the latter. We use the numerical model to compute the *velocity transfer functions* for the various cases studied. This approach gives a better resolution in the frequency domain, as issues dealing with the shape of the transient pulse, the duration of the response, and the sampling rates do not play a role.

The writer feels that this approach demonstrates more clearly the potential for the use of acoustic methods. The effects of the shape of the load and issues related to sampling can be easily incorporated a posteriori. Hence, the results presented here, in addition to show a clearer picture, can be used as a tool for designing real life experiments.

Simplified models to explain resonances in delaminated plates

When a delaminated plate is excited with a dynamic source, it elicits a response which is a combination of at least two phenomena: flexural waves in the concrete above the delamination —the so-called *drum mode*— and echoes from the physical discontinuities in the plate, the layer interfaces and the delamination itself. The role that these two mechanisms play in the response varies with the size and depth of the delamination. Because the existing indirect methods exploit either one of these two main physical phenomena, their success will depend on the actual physical characteristics of the delamination.

Both mechanisms of response can be explained with simple models. For the drum mode, we can think of the concrete on top of the delamination as a plate partially restrained by the edges. The edge boundary condition will be a compromise between a clamped edge and a simply supported edge, but perhaps somewhat closer to the former. In the case of shallow delaminations, the delaminated mass is much smaller than the mass of the plate, so the assumption of a plate resting on a fixed support may work very well. As the depth increases, however, this model progressively deteriorates.

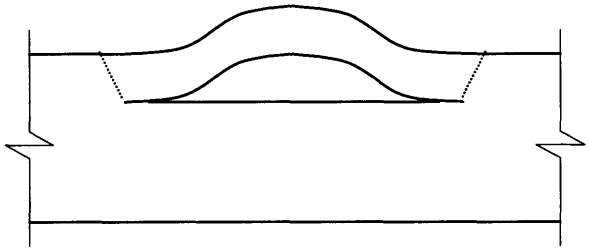

Figure 4-1: Bending of delaminated portion of plate

Making an analogy of the drum mode with that of plane flexural waves in thin plates with clamped conditions, we obtain the dispersion relation[21]

$$D k^2 - \rho h c^2 = 0 \tag{4.1}$$

In this relation, $D = Eh^3/12(1-\nu^2)$, E is the modulus of elasticity, ρ is the density, ν is Poisson's ratio, h is the thickness of the plate and k and c are the wavenumber and wave velocity, respectively. This is possibly the simplest model, in the sense that shear effects and rotary inertias are neglected.

As for the echo mechanism, Sansalone and Carino thoroughly explain it in their paper "*Finite Element Studies of The Impact-Echo Response of Layered Plates Containing Flaws*"[30]. Here, we provide a brief summary of their description.

A sudden vertical impact on the surface of a plate generates three types of waves: dilatational (P) and distorsional (S) waves that propagate into the body, and a Rayleigh (R) wave that propagates near and on the surface. The body waves, as they hit the opposite surface of the plate are reflected, and thus return to the recording surface. For points close to the source, the vertical motion at the receiver is largely controlled by P waves, because S waves produce mostly horizontal motions there while the R wave passes by before any reflections arrive from the interior.

Consider first a homogeneous plate and assume normal incidence, which is a reasonable assumption for receivers close to the source. When the P wave reaches the opposite face, it generates a reflected wave with reversed polarity that, upon returning to the top surface, is yet again reflected with changed polarity, after which the reflection pattern is repeated, causing a resonant condition. The time lapse between echoes equals the travel time for the P-wave across twice the thickness of the plate. For P-wave velocity c_P and thickness h, this resonant condition manifests itself in the spectra as a peak at a frequency

$$f = c_P/2h \tag{4.2}$$

In a two-layer plate, there are three main resonant conditions, two that correspond to the individual layers and one for the composite plate itself. If we use the sub-index 1 for the harder layer and 2 for the softer layer, these frequencies are

$$
\begin{aligned}
f_1 &= c_{P1}/2h_1 \\
f_2 &= c_{P2}/4h_2 \\
f_{12} &= \frac{1}{2h_1/c_{P1} + 2h_2/c_{P2}}
\end{aligned}
\tag{4.3}
$$

When a wave traveling in a softer medium encounters a harder one, it is reflected with the same polarity, and thus the pattern on the free face is repeated only half as many times as if it were attached to a softer medium. This is why the resonance related to the softer layer has a factor of four instead of two.

The main hypothesis of the impact-echo method is that these resonances will show up in the frequency analysis of the time histories recorded on the plate. If there were any significant delaminations, they would affect the main resonances and a new peak associated with the depth of the delamination would become apparent as well.

Anti-plane drum mode

The first case we analyze is a 20 cm thick homogeneous free plate subject to an anti-plane load centered above a delamination. This case does not bear much practical interest, but it provides relevant and interesting insight into the drum mode.

The properties of the plate and principal parameters in the analysis are

Thickness of plate:	0.2 m
Speed of shear waves:	2.0 m/ms
Material damping:	0.1 %
Frequency range:	0-10 kHz
Frequency step:	0.02 kHz
Length of Boundary Elements:	0.005 m

The response is measured at the loaded point, above the delamination, and in this analysis, we used the Green's functions for the homogeneous case, rather than the Thin-Layer Green's functions.

Figure 4-2 compares the frequency response of an undamaged plate to those of damaged plates when subject to anti-plane loading. The response of an undamaged free plate presents sharp peaks corresponding to the full thickness of the plate and multiples of it: 5 kHz, 10 kHz, 15 kHz and so on; the response in between these peaks is small.

On the other hand, the delaminations introduce significant disruption in the response. The responses of the damaged plates do not show a resonance at the frequency corresponding to the thickness of the plate. Instead, they show a new low frequency resonance that largely dominates the response. This resonance is related to the sections of the plate above and below the delamination acting as shear beams partially clamped on the edges (Figure 4-3), which results in waves of wavelengths close to twice the length of the delamination propagating horizontally from end to end of it. This resonance is the equivalent to the drum mode, except that instead of bending for the anti-plane problem we have shear deformation. In addition, the delaminated plates show a larger response at frequencies corresponding to the depth of the delamination, the expected echo at the crack.

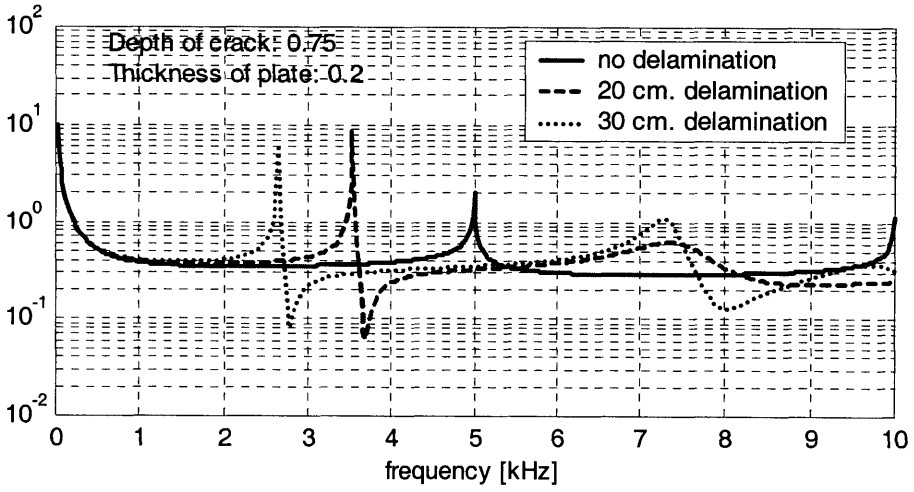

Figure 4-2: Transfer function of free plate subject to anti-plane load

We observe in Figure 4-3 that the drum mode affects only locally to the response of the plate. Thus, it is only excited by loading on top of the delamination, and it is only sensed there, too. The drum mode shape further indicates that its energy does not flow away from the crack, but is mostly trapped there.

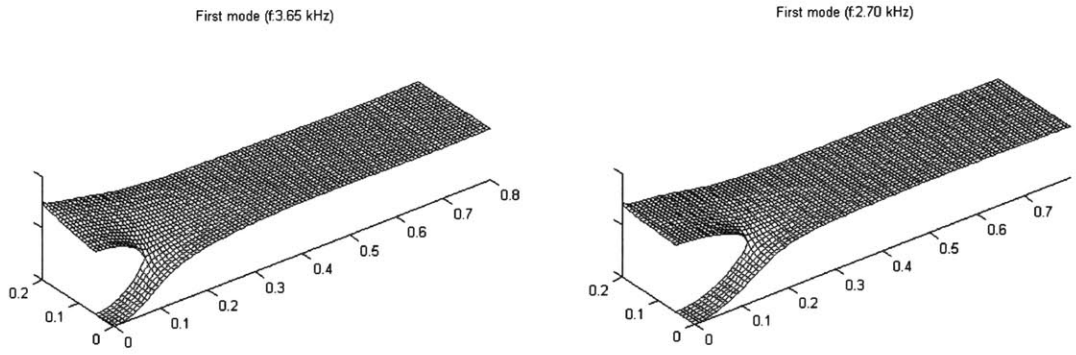

Figure 4-3: Drum modes for anti-plane load (20 and 30 cm. delaminations)

An extensive analysis of different cracks shows that for cracks wider than 1.5 the thickness of the plate, the drum resonance depends mostly on the width of the crack and not on its depths. The drum resonance for these large cracks provides a good estimate of their sizes. For smaller cracks, both depth and size affect the drum mode and size estimation cannot be done based only on the drum mode.

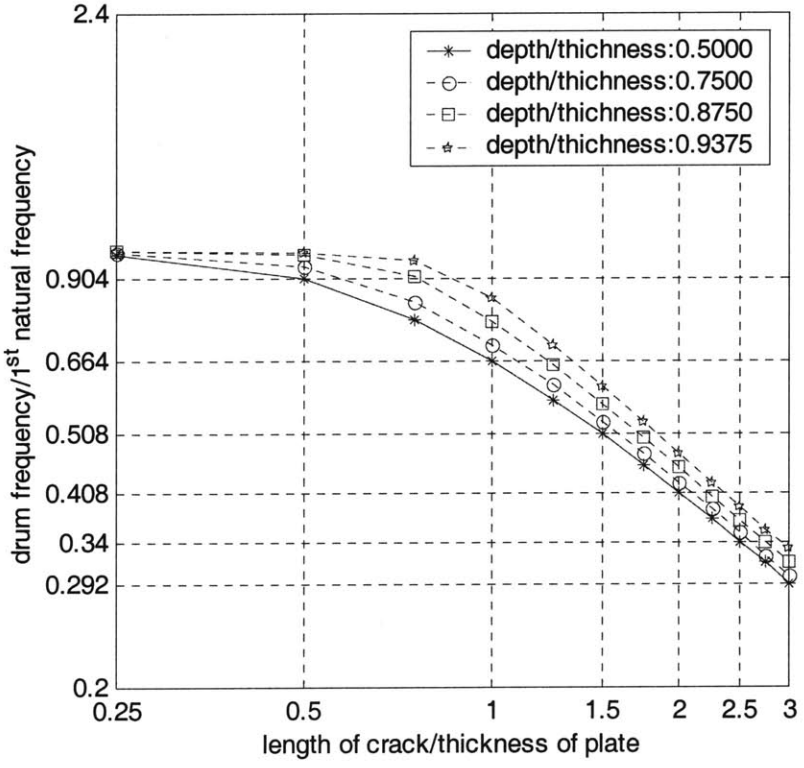

Figure 4-4: Drum resonance as a function of size and depth of crack

Response of homogeneous plate

Next, we turn to a more practical situation, and study a 20 cm thick homogeneous concrete plate. We study six different crack sizes at six different depths. In every case, the source is centered above the crack and the response is measured 2.5 cm away from it. The properties of the plate and principal parameters in the analysis are

Thickness of plate:	0.2 m
Shear wave speed of concrete:	2.0 m/ms
Poison's ratio:	0.25
Material damping:	0.1 %
Frequency range:	0-20 kHz
Frequency step:	0.05 kHz
Length of Boundary Elements:	0.005 m
TLM model:	160 quadratic layers

For these properties, we expect the main echo for the solid plate to show up at a frequency of about 8.6 kHz.

For the sake of clarity, we present the velocity transfer functions only for cracks of lengths 10, 30 and 50 cm. We also show explicitly the lowest modes for shallow delaminations, the ones due to bending, and compare the actual size of the crack to estimates computed from bending theory.

Analysis of the Frequency Response

There are several conclusions that follow directly from the results of our analysis.

As expected, the response of a solid plate presents a major concentration of energy around the main P-resonance at 8.6 kHz. There are two additional minor peaks, one at twice the main P-resonance and one at a slightly lower frequency, namely 15 kHz. The energy content below the main P-resonance is low and presents no peaks.

For delaminations within the top-half of the plate, the drum modes control the response, which causes significant response levels at low frequencies; the shallower the crack, the larger the energy content at low frequencies (Figure 4-5).

The drum modes at frequencies below the main P-resonance are local to the crack and do not propagate. Hence, they are only excited and detected when the impact and measuring takes place in the immediate proximity of the crack. In addition, they attenuate much slower than the propagating modes since material damping is their main mechanism of dissipation.

For a fixed crack depth, the drum modes are good indicators of the size of the crack. Indeed, for shallow cracks, the ratios between the length of the cracks and the length of a simply supported plate with resonance frequency equal to the drum modes are consistent (L_{EST} in Table 1 and Table 2). However, inasmuch as multiple drum modes are possible depending on the location of the source relative to the crack, it can be tricky to identify which are the modes actually excited. The *n*-resonance of a simply supported plate of thickness h and length L is

$$\omega_n = (n\pi)^2 hc_s \Big/ \left(L^2\sqrt{6(1-\nu)}\right) \tag{4.4}$$

where c_S is the velocity of shear waves in the material and ν is the Poisson's ratio.

In some cases, it is possible for the frequency of one of the drum modes to be close to the main P-resonance. In this case, an energy peak at this resonance can mislead us into thinking that the plate is in good condition, while in fact it is not (e.g. 0.5 m-long crack at center graph in Figure 4-5).

Estimating the depth of shallow cracks from its echoes can be a very difficult task. For one, we would need to be able to excite very high frequencies. In addition, there is the fact that most of the energy of the response is in the low frequency range (drum modes).

For cracks at the center of the plate, the thickness resonance does not exist. Instead, as predicted by the impact-echo model, there are significant peaks at twice this frequency. For cracks at other depths, the thickness resonance does not always disappear, and the crack-depth resonance is not always easy to identify.

The intensity of the drum mode vibration decays very fast with the depth of the crack. Once this depth increases beyond the center of the plate, it virtually disappears. In that case, the impact-echo is the only one capable of detecting such deep cracks.

A standard experiment based on the impact-echo method does not convey information about the dimensions of the crack. To size the crack, it is necessary to register acoustic signals in a dense network of points located in the anticipated location of the crack and search for its echo.

Table 1: Fundamental drum mode for shallow delaminations

	Depth of crack					
	0.0125		0.025		0.1	
Length of crack (L)	f_{D1} [kHz]	L_{EST}	f_{D1} [kHz]	L_{EST}	f_{D1} [kHz]	L_{EST}
0.10	2.75	0.08	4.05	**0.10**	4.80	0.18
0.20	0.75	0.16	1.45	0.16	2.60	0.24
0.30			0.70	0.23	1.60	**0.30**
0.40			0.40	0.30	1.10	0.37
0.50					0.80	0.43
0.60					0.60	0.50

Table 2: Second drum mode for shallow delaminations

	Depth of crack					
	0.0125		0.025		0.1	
Length of crack (L)	f_{D2} [kHz]	L_{EST}	f_{D2} [kHz]	L_{EST}	f_{D2} [kHz]	L_{EST}
0.10						
0.20	4.20	**0.20**				
0.30	1.95	**0.29**	3.50	**0.31**	6.00	0.47
0.40	1.05	**0.40**	2.15	**0.39**	4.45	0.55
0.50	0.65	**0.51**	1.45	**0.48**	3.40	0.63
0.60			1.05	0.56	2.70	0.70

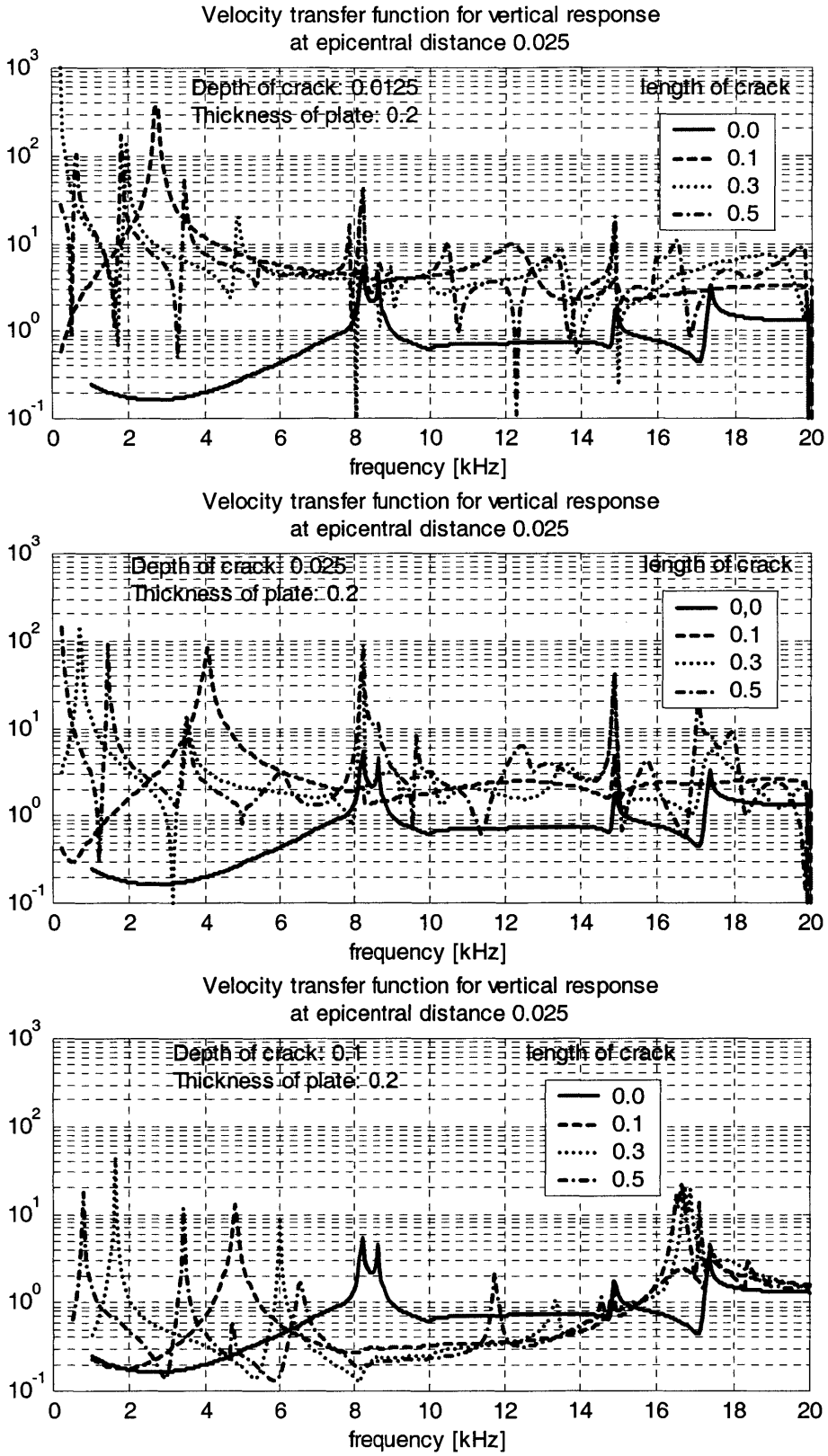

Figure 4-5: Transfer functions for delaminated homogeneous plate

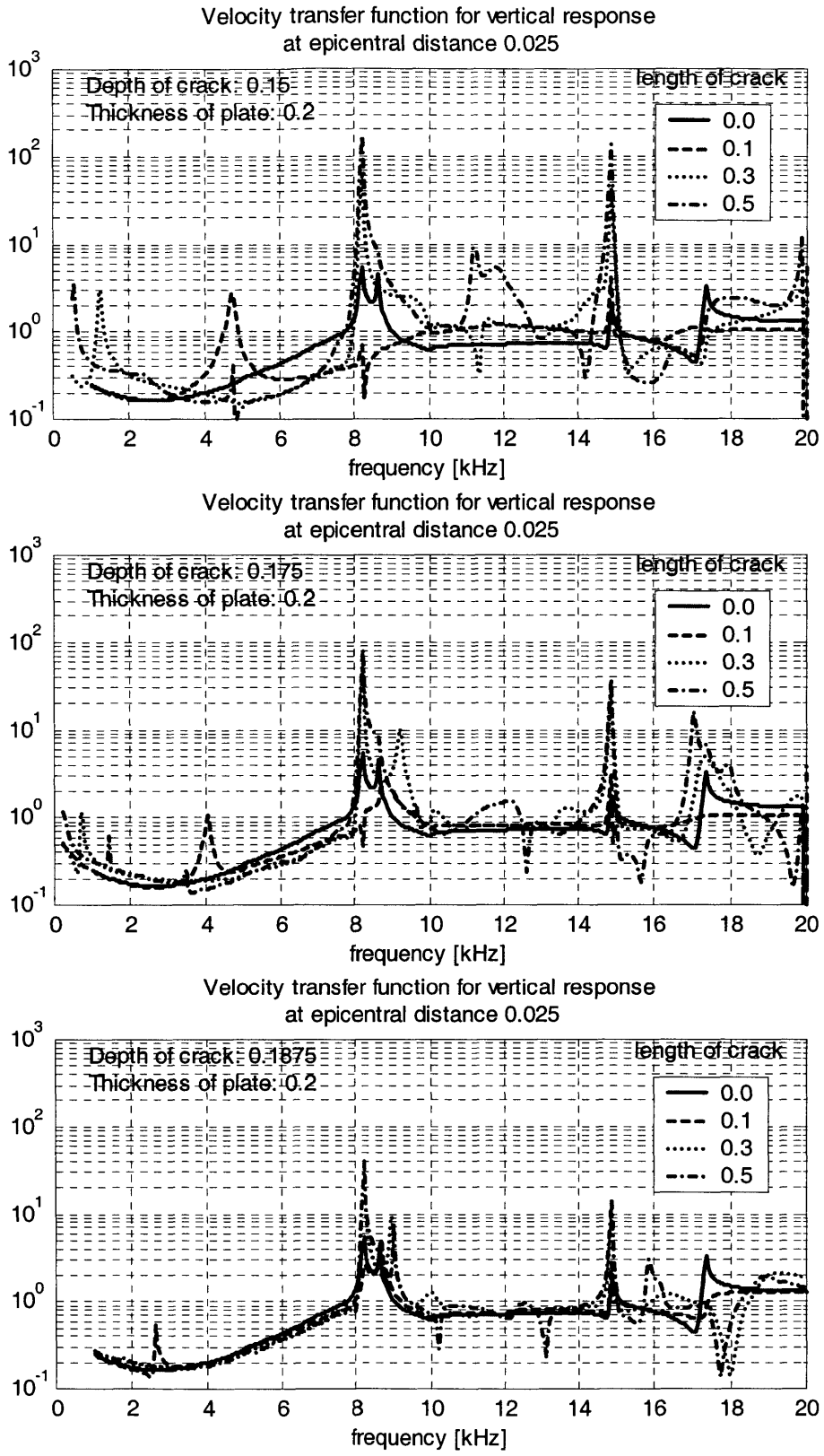

Figure 4-6: Transfer functions for delaminated homogeneous plate

Response of laminated plates

Finally, we study two common cases of laminated plates: a bridge deck and a water main.

For a bridge deck, neglecting the effect of the reinforcement, we have a soft thin asphalt layer on top of a hard concrete layer. The properties and principal parameters are

Thickness of asphalt layer:	4.5 cm
Thickness of concrete layer:	15.5 cm
Shear wave speed of asphalt:	1.4 m/ms
Shear wave speed of concrete:	2.0 m/ms
Poison's ratio:	0.25
Material damping:	0.1 %
Frequency range:	0-30 kHz
Frequency step:	0.05 kHz
Length of Boundary Elements:	0.005 m
TLM model:	160 quadratic layers

For the sake of simplicity, we assumed equal density, damping and Poison's ratio for the asphalt and the concrete.

The water main example involves a similar configuration: From the inside out, the concrete core constitutes the top soft layer, while the outer mortar-cover represents a thin and hard bottom layer. The differences with the deck are

Thickness of concrete core:	15.5 cm
Thickness of mortar cover:	4.5 cm
Shear wave speed of concrete:	2.0 m/ms
Shear wave speed of mortar:	2.4 m/ms

For the properties listed above, we expect the main echo at a frequency of about 7.9 kHz for the deck and 8.99 kHz for the pipe.

The characteristics of the transfer functions for the laminated plates cases (i.e. deck and pipe), are similar to those of the homogeneous plate, whether or not the systems contain a delamination crack. Thus, the conclusions for the homogeneous case apply also to these mildly heterogeneous cases.

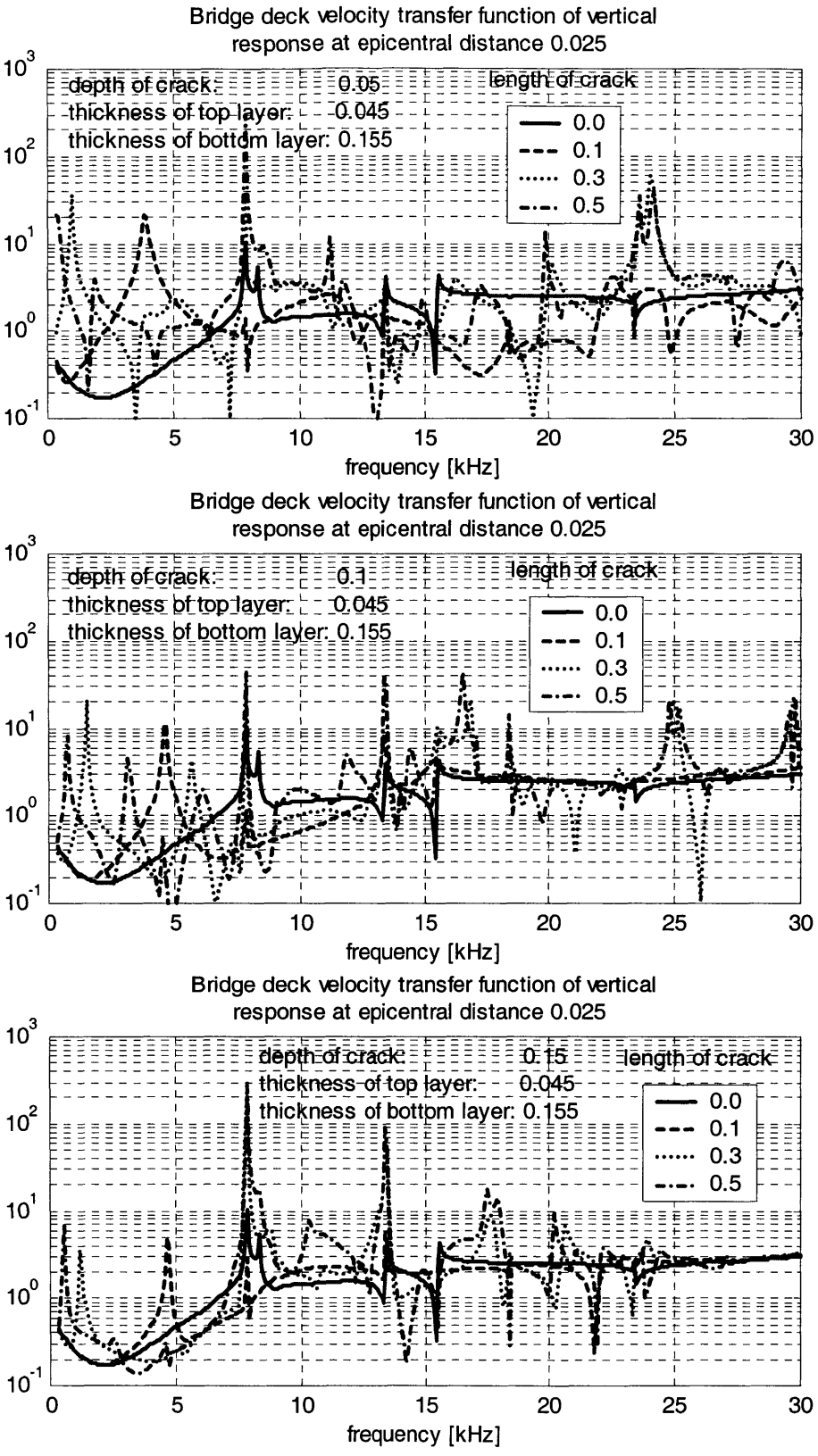

Figure 4-7: Transfer functions for delaminated bridge deck

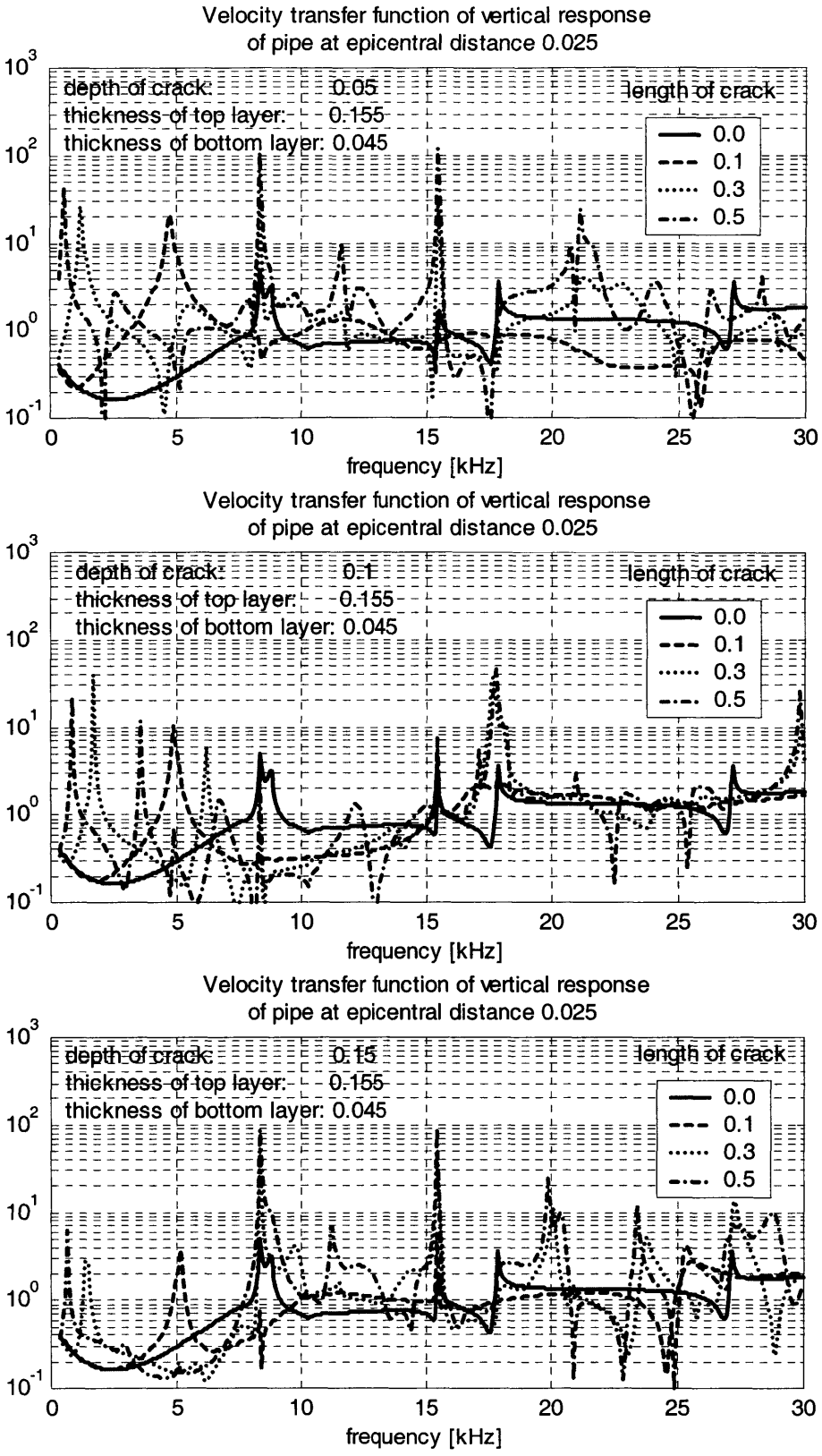

Figure 4-8: Transfer functions for delaminated pipe

Appendix

We include in this appendix plots of the steady state response of the plate at some of the resonant frequencies, including some of the drum modes. For each case, we present four snapshots at different instants of the cycle, so that the actual motion pattern can be visualized.

Figure 4-9 to Figure 4-11 show plates with shallow delamination. Figure 4-9 shows a typical drum mode, corresponding to the first bending mode of the delaminated portion. Figure 4-10 shows the drum mode corresponding to a higher bending mode. The frequency now is above the full thickness resonance and we can observe some energy flow away from the crack, mainly on the top surface. Figure 4-11 shows an interesting case of a large shallow delamination, where in spite of the delamination, we can still see the full thickness resonance of an undamaged plate. Of course, the response of the delaminated plate at lower frequencies is significantly larger than that of the undamaged one.

Figure 4-12 and Figure 4-13 show the first two drum modes, corresponding respectively to the first and third bending mode of the delaminated area, for a center delamination. Both frequencies are below the main P-resonance and the responses do not propagate into the plate. Figure 4-14 shows a resonance higher than the main P-resonance for a center delamination that combines some bending at the crack with some full-thickness mode. This is however a minor resonance that would likely be overshadowed by others. The response in Figure 4-15 is interesting. It shows up at the frequency of the second full thickness resonance. However, it only involves the plate areas above and below the crack. While the portion above the delamination expands, the portion below compress and vice versa, generating a local standing wave through the thickness.

Figure 4-16 and Figure 4-17 show low frequency resonances for deep cracks. The responses in these figures include some minor local bending around the crack, similar to that in the drum modes, combined with a bending wave propagating along the plate. These are again low energy resonance probably without much practical interest.

Finally, Figure 4-18 shows the response that correspond to the echo for a delamination at a depth of three fourth of the thickness. The corresponding peak is shown at the top of Figure 4-6.

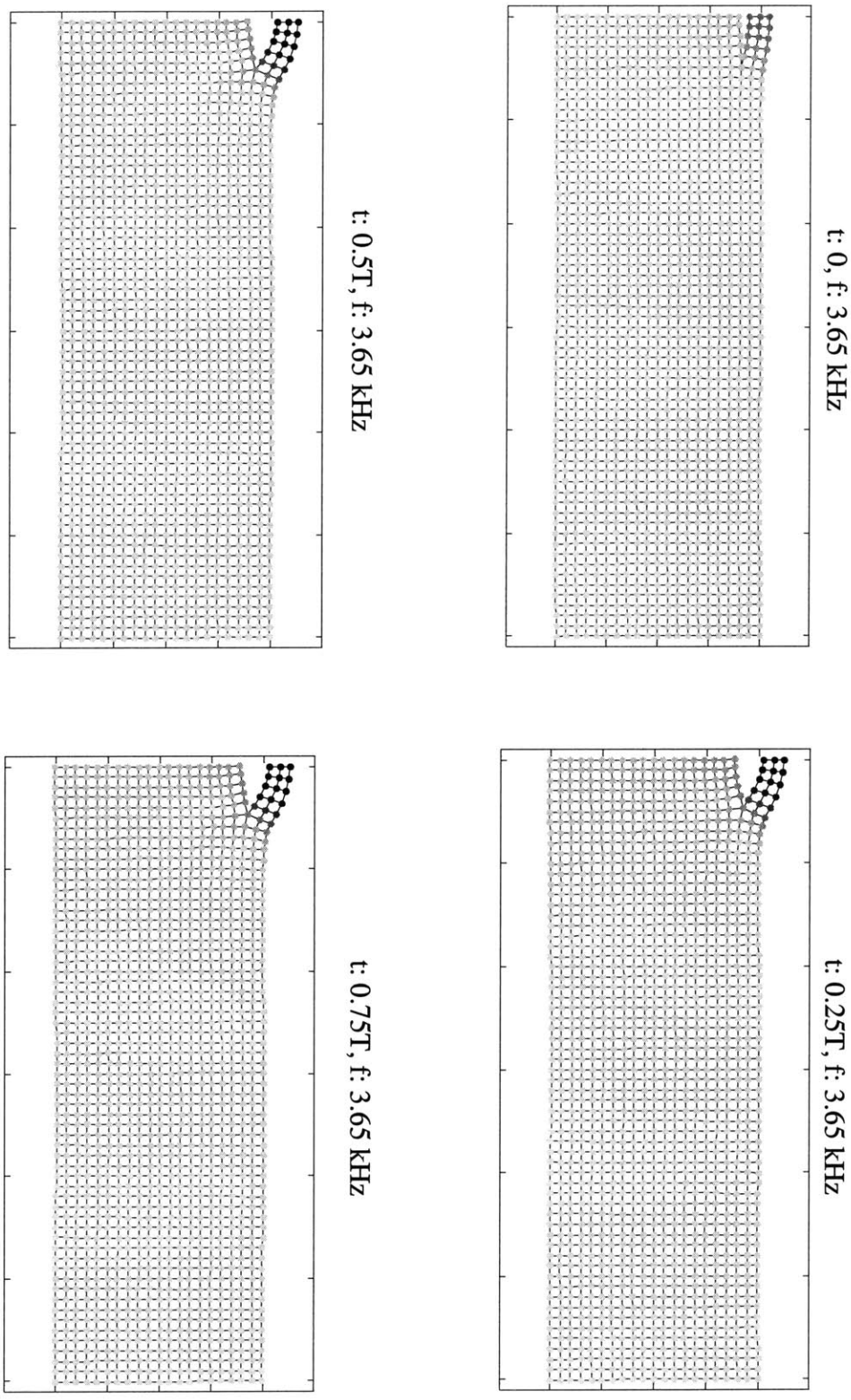

Figure 4-9: First drum mode for shallow small delamination

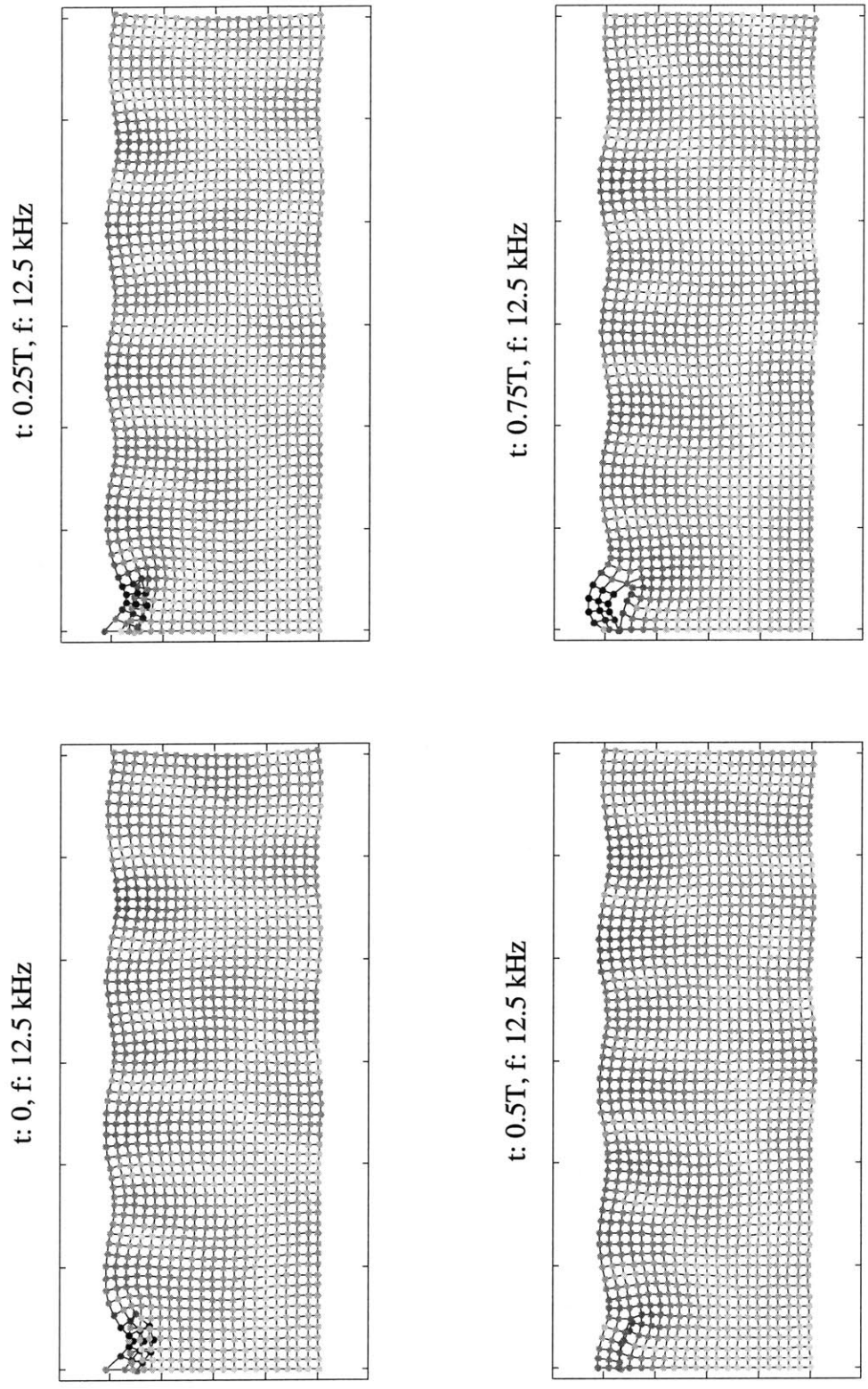

Figure 4-10: Second mode for shallow small delamination

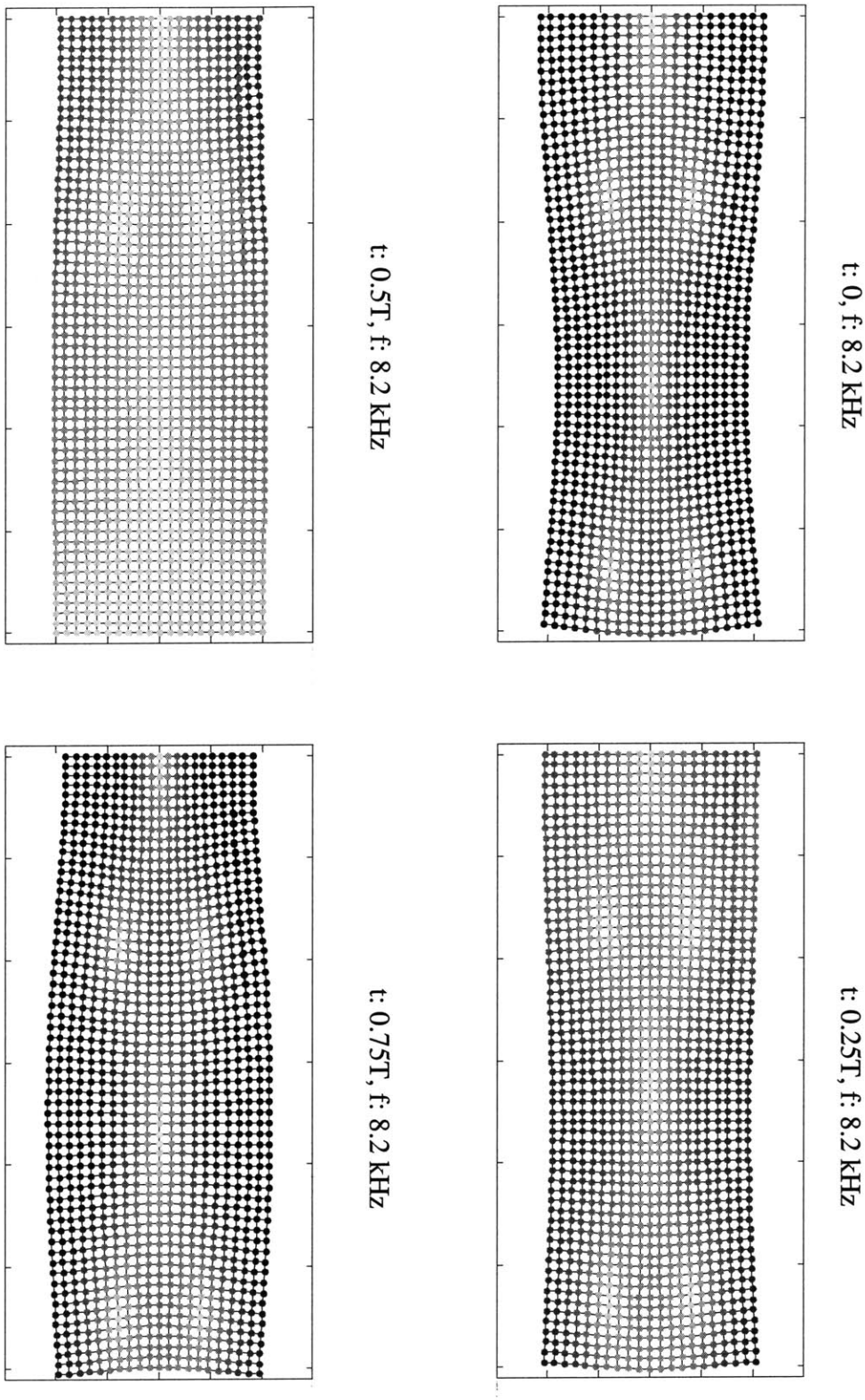

Figure 4-11: Full-thickness resonance in plate with large shallow delamination

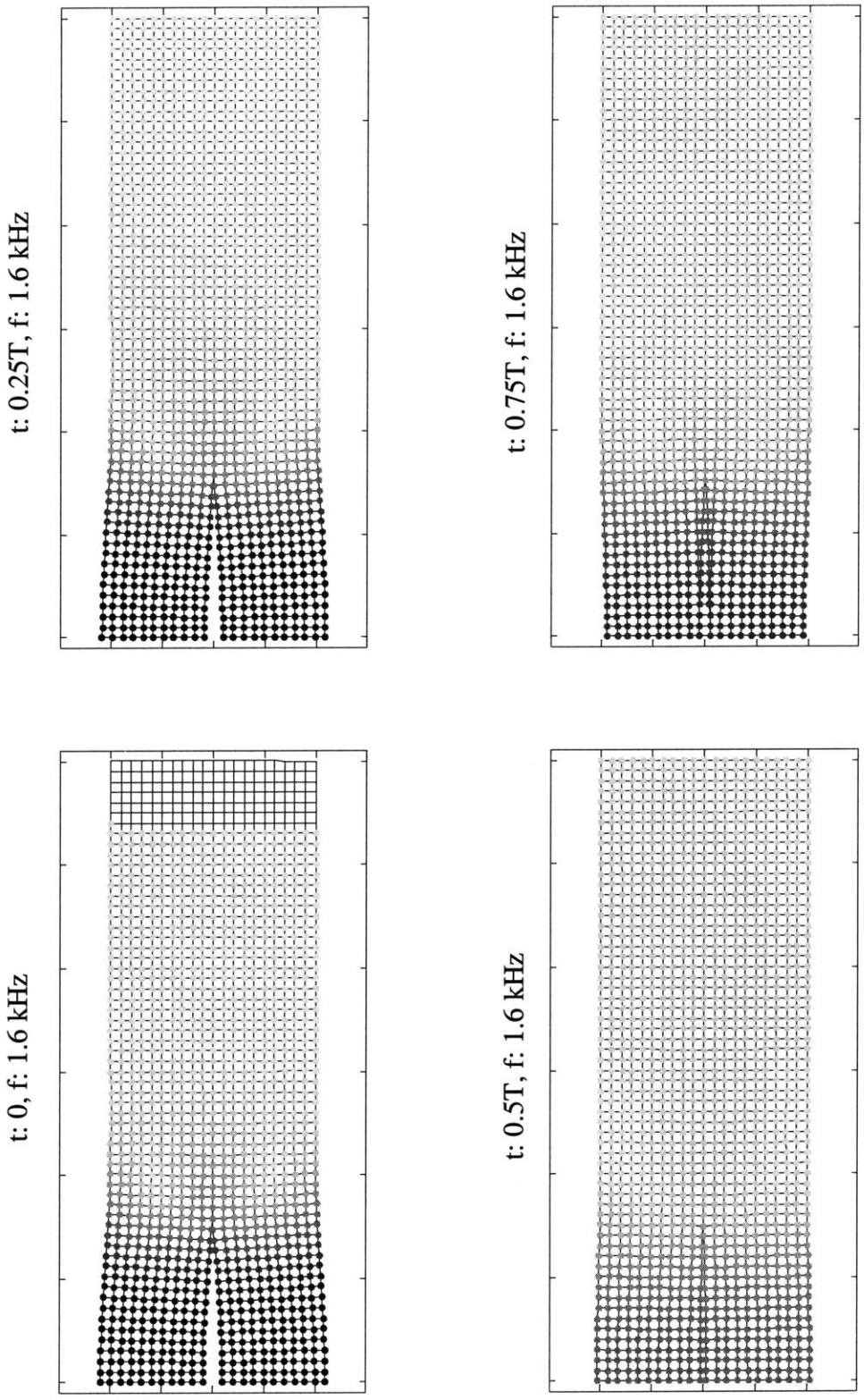

Figure 4-12: First drum mode for center delamination

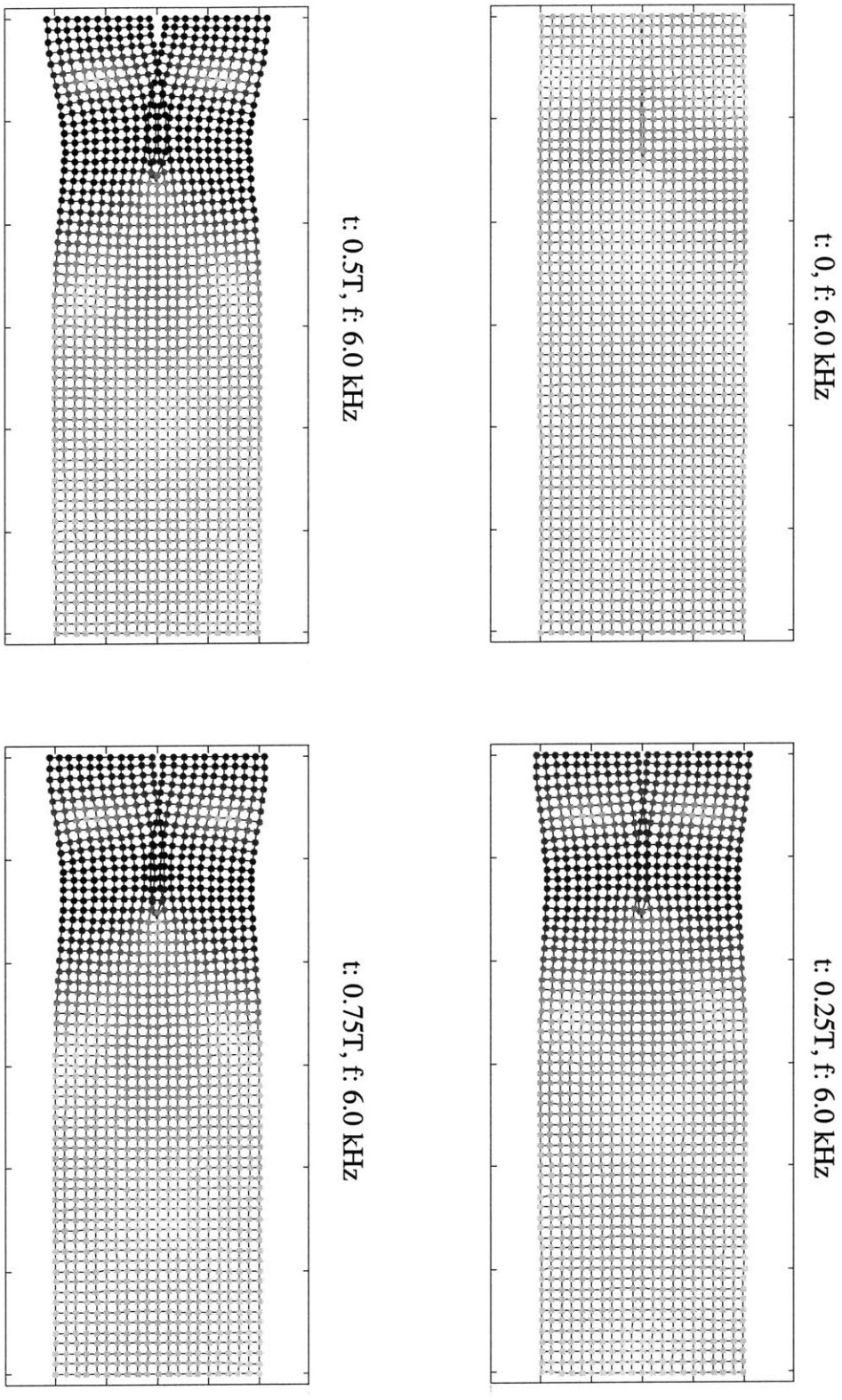

Figure 4-13: Second drum mode for center delamination

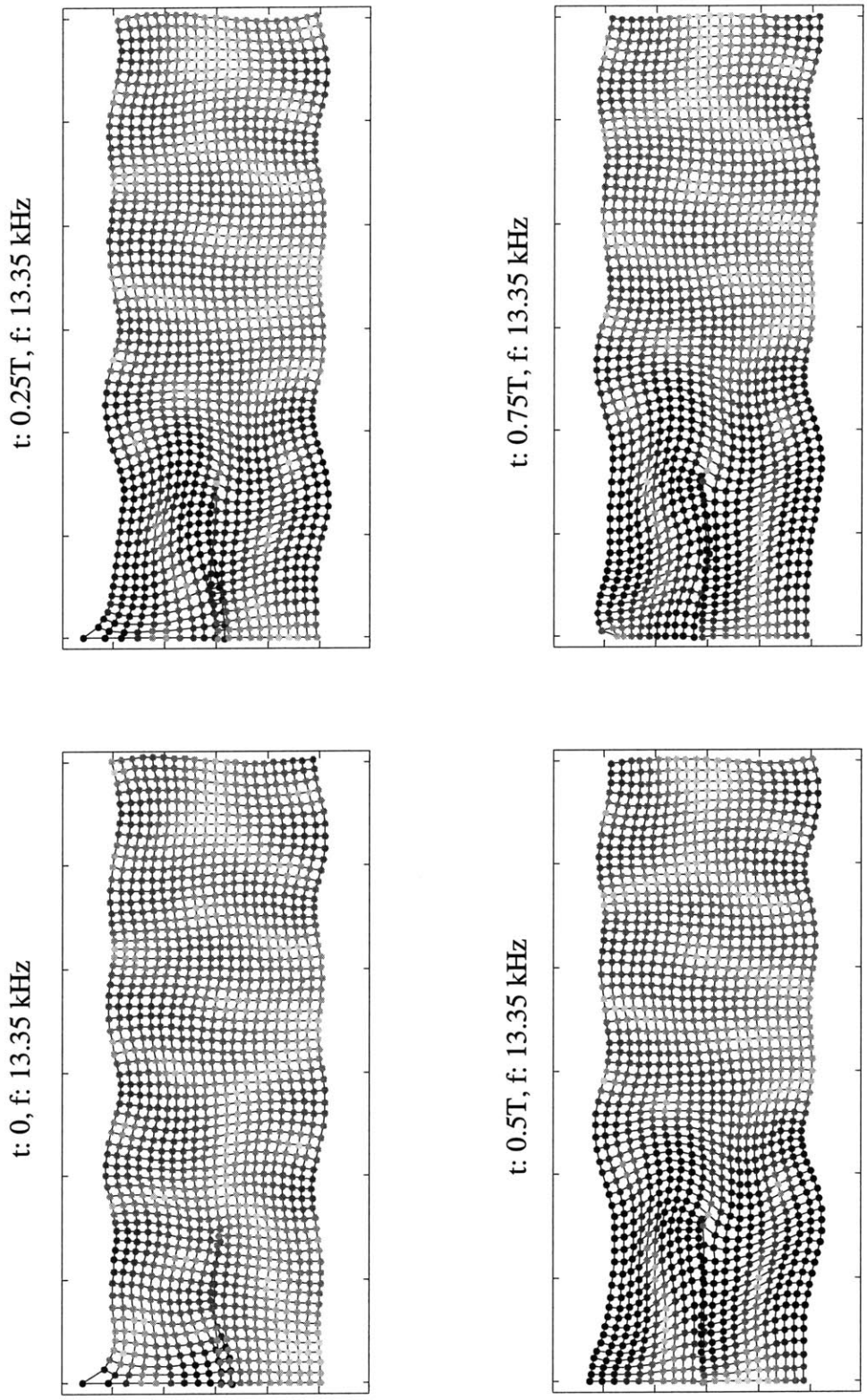

Figure 4-14: Minor resonance for center delamination

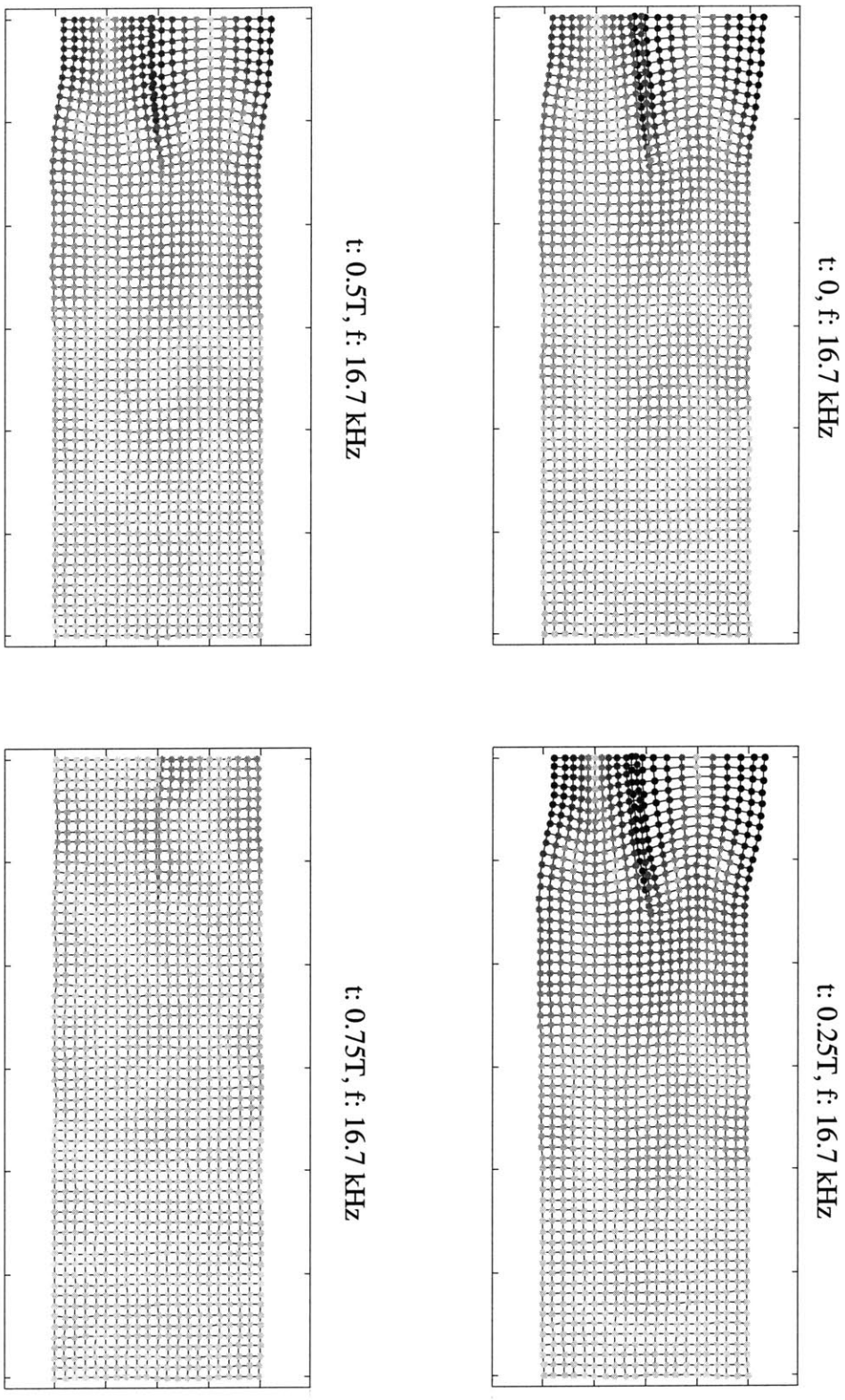

Figure 4-15: Full-thickness second resonance in plate with center delamination

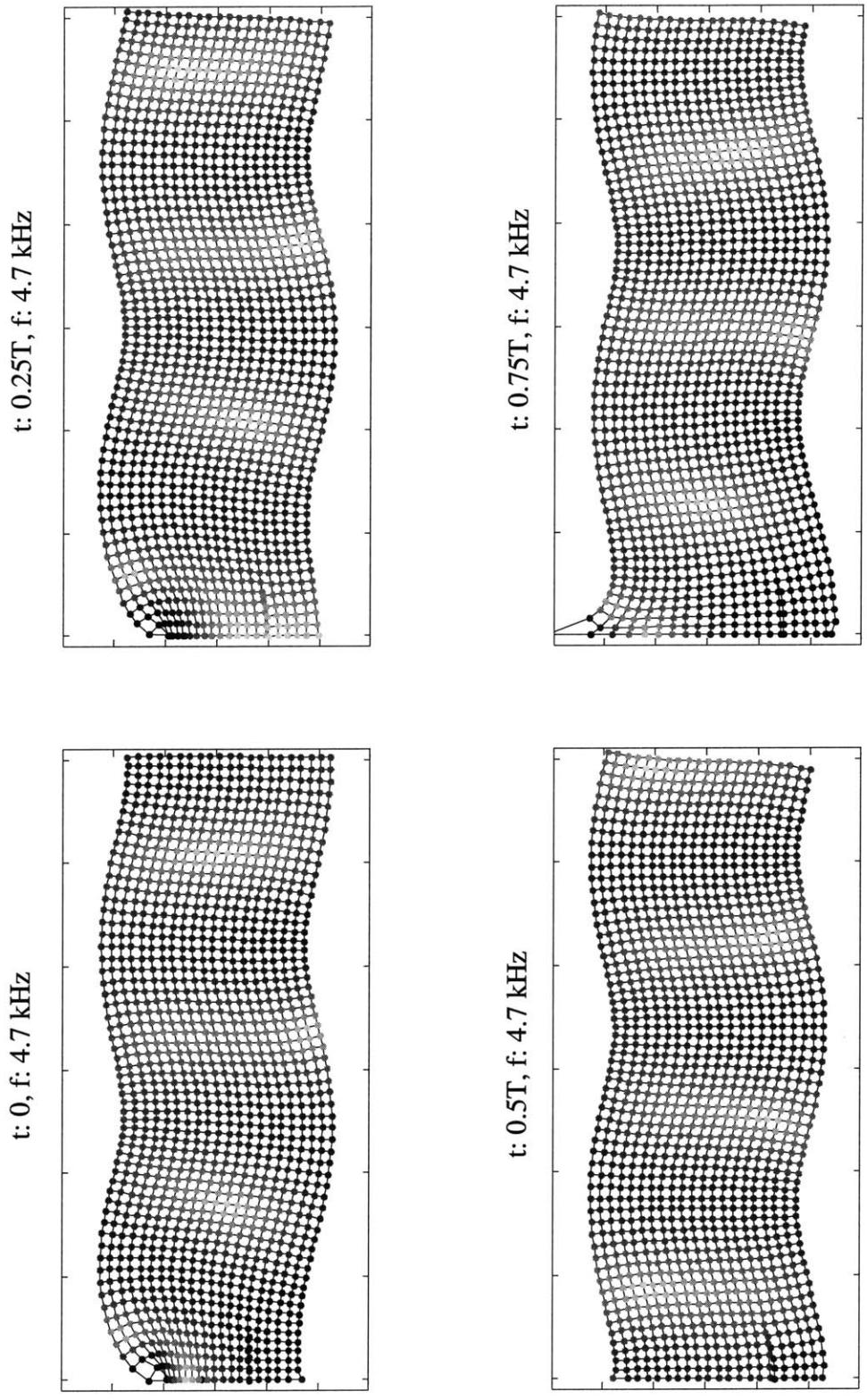

Figure 4-16: Bending mode for delamination in bottom half of plate

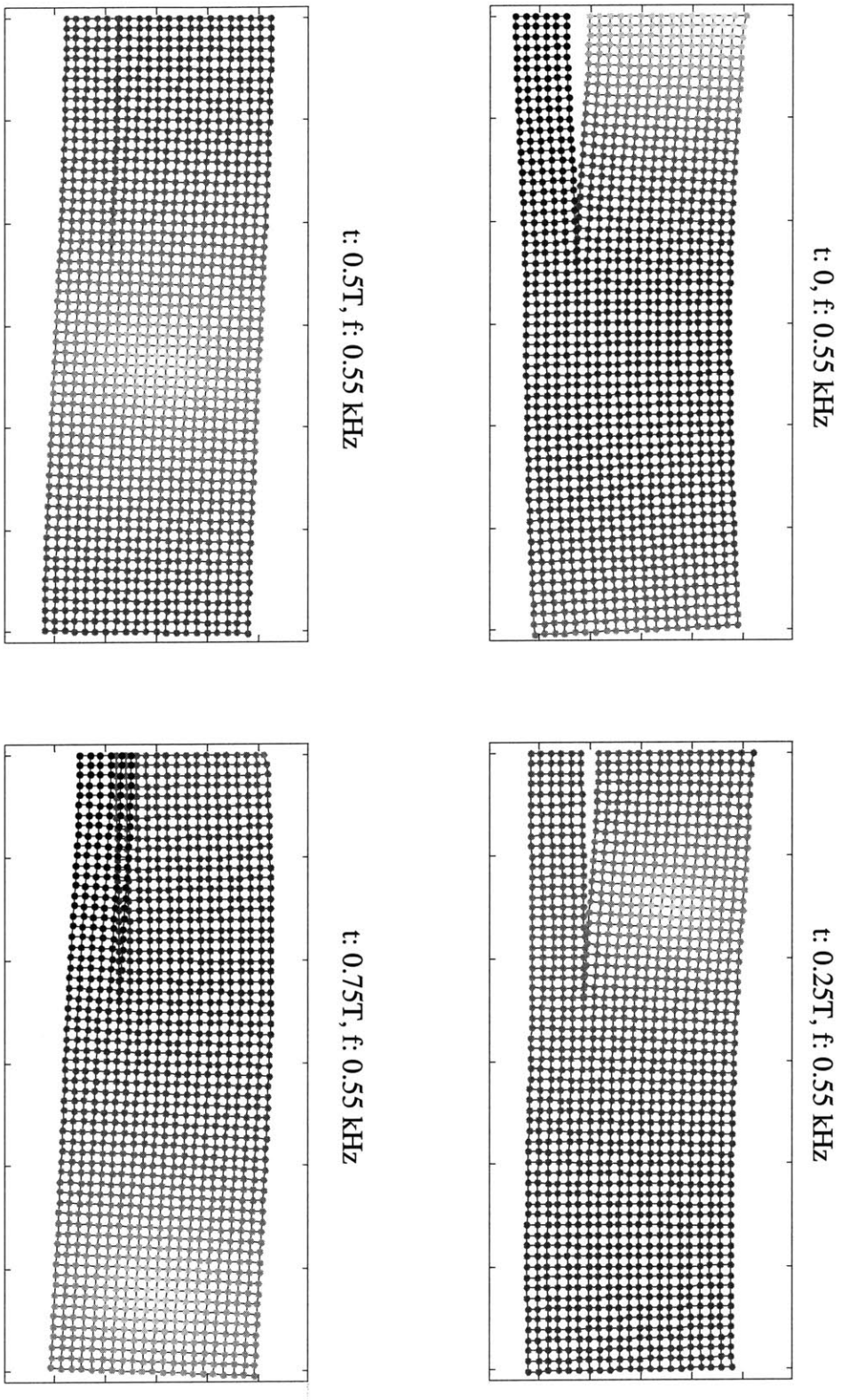

Figure 4-17: Low frequency bending mode for deep delamination

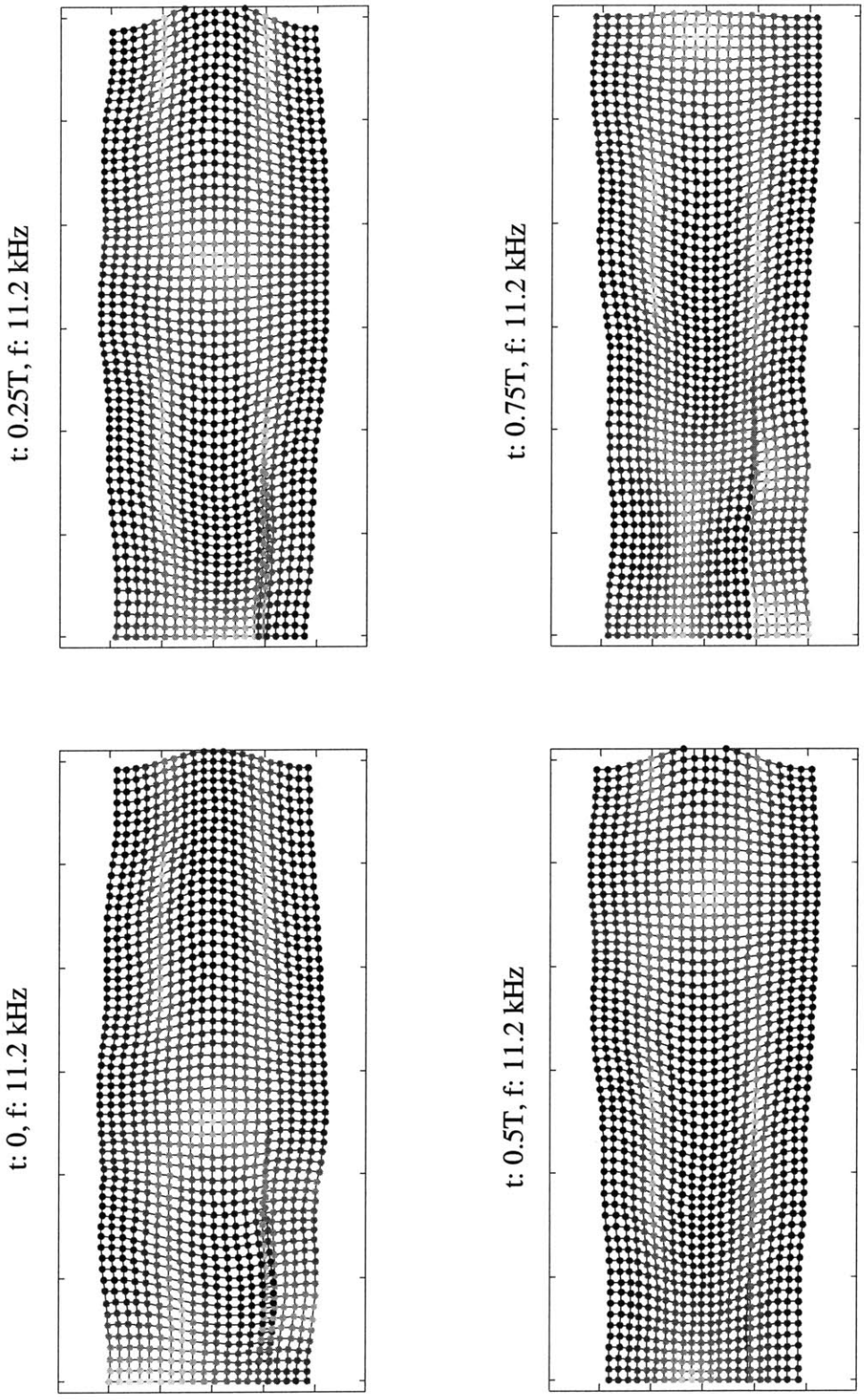

Figure 4-18: First echo for 0.15 m. deep delamination

Chapter 5 :

Spectral Analysis

Introduction

The non-destructive evaluation (NDE) of plate-like structures such as concrete walls and slabs is a lengthy and complicated process. Existing NDE methods such as sounding and the Impact Echo Method rely on very simple models of the response to transient loadings, and this simplification imposes limitations in their ability to detect defects in the structures. These conventional methods provide information only about a limited area in the vicinity of the testing location, and their performance depends significantly on the depth of the imperfections. Because these structures usually extend over large areas, proper assessment via conventional NDE methods requires a large number of testing points.

When plate-like structures are subjected to transient loading, the boundaries and material transitions act as wave-guides. Thus, a proper analysis of the propagation of elastic waves within plates requires elaborate mathematical models. The Normal Modes Method is one such mathematical tool, which provides rich insights into the propagation of waves in wave-guides. In a normal modes solution, we express the dynamic response at an arbitrary point in a plate by appropriate superposition of evanescent and propagating wave modes. The level of participation of the different modes varies with the location and spatial distribution of the loading, but also with the presence of imperfections or delaminations in the plate. Thus, the decomposition of the measured field into modes can provide us with important information about the presence of imperfections in the plate.

The inversion and separation of a propagating field into its constituent modes, and the estimation of the relative strengths of each of these, can be accomplished by means of an array of sensors. By combining and weighting adequately the output of the different sensors, we can extract the signals that travel through the array at certain speeds while canceling the wave components that travel at other speeds. In this way, we can estimate the energy of the propagating field as a function of the frequency and wavenumber. The dominant propagating modes will reveal themselves in the form of strong accumulations of energy along so-called dispersion curves.

In this chapter, we investigate the impact that the presence of a crack bears on the propagating field in a plate. We model different crack conditions with the numerical tool described earlier in this work, and we use array processing techniques to study and separate the computed wave fields.

Arrays of Sensors as Spatial Filters

Assume that a non-dispersive plane wave of a certain phase velocity passages underneath an array of sensors placed in a homogeneous medium. Since the wave arrives at each sensor at times that depend on their position while the underlying wave motion remains identical, the signal will exhibit time delays that vary from sensor to sensor in proportion to the projection of the velocity vector onto the array. If we delay the output at each sensor in accord with its position and average all the time-shifted outputs, we recover the shape of the propagating signal. This simple process is called a *delay-sum beam-former*, also known as a *conventional linear array* (Figure 5-1).

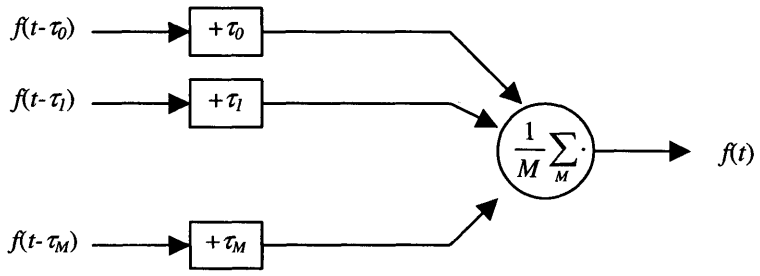

Figure 5-1: Delay-sum beam-former

Given a velocity of propagation of waves in the medium, plane waves propagating in different directions will exhibit different velocity components parallel to the array axis. For this reason, by applying adequate delays, we can constructively enhance the signal components that travel across the array in a certain direction (certain velocity) while reducing the effect of random noise or other signals arriving from different directions. In this fashion, the array works as a spatial filter that allows us to differentiate between the various plane-wave components in a propagating field. Moreover, from the definition of the wavenumber vector follows a direct relationship between the direction of propagation

and the component of the wavenumber parallel to the array, and separating between directions is actually the same as separating between wavenumbers.

Beam-Pattern

In the context of plane waves propagating in a locally homogeneous medium, we define the *beam-pattern* of the array as the frequency wavenumber response function versus the wavenumber (i.e. direction). The *beam-pattern* describes the response of the array to an arbitrary plane wave (Figure 5-2).

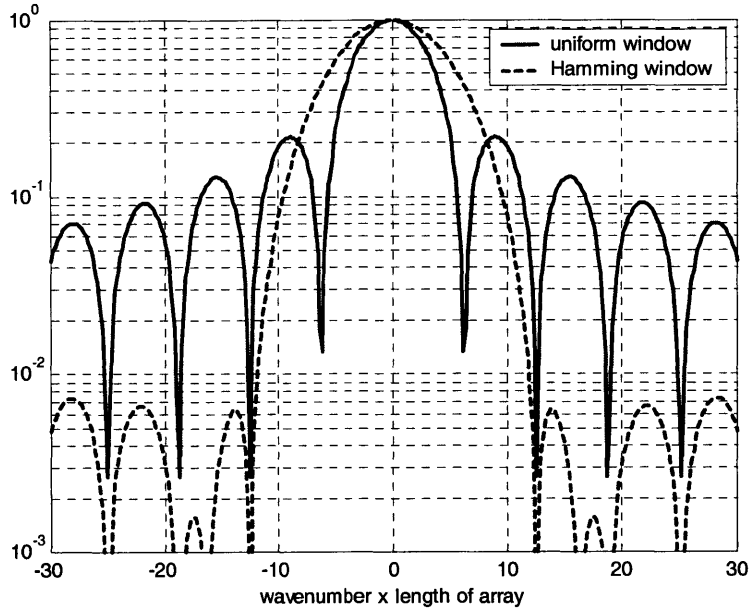

Figure 5-2: Beam-patterns for uniform and Hamming weightings (wavenumber measured relative to the target wavenumber)

Geometry constraints

Ideally, we want the response of the array to be 100% in the targeting direction and 0% otherwise. This is not practicable however, because the characteristics of the *beam-pattern* are largely influenced by the geometry of the array, which are in turn constrained by practical issues.

The *resolution of the array* is defined as the ability of the array to resolve two different plane waves. This characteristic is controlled by the width of the main lobe in the *beam-pattern*, which in turn depends on the total length of the array (Figure 5-2). In the same way that the total duration of a time series in a *Frequency Spectral Analysis* controls the resolution (i.e. frequency step) in the frequency domain, the total length of the array controls the resolution (i.e. wavenumber step) of the array in the wavenumber domain.

On the other hand, the minimum distance between sensors defines the maximum wavenumber that the array will be able to distinguish; this distance should be at most half the shortest wavelength in the wave field to prevent aliasing of large wavenumber components into small ones. For low frequencies, the dispersion relation of the medium will ensure that there are no components at large wavenumbers; for large frequencies, the propagating waves at large wavenumbers could appear aliased in the low wavenumbers and the minimum-distance-between-sensors constraint does apply.

Spectral weighting

There are numerous practical issues that constrain the total length and the number of sensors in the array, such as space availability, electronic equipment and ultimately cost. By applying different weights to the outputs of the different sensors, the *weighting process* tries to optimize the properties of the *beam-former* for a given geometry.

A traditional approach in the selection of these weights is to use classical windows from *Frequency Spectral Analysis*, drawing on the existing parallelism between frequency spectra and wavenumber spectra. The properties of different windows have been the subject of comprehensive research and it is available and well documented (see Harris[34] for an excellent review).

Frequency-Wavenumber Spectral Estimation

By exploiting its capabilities as a spatial filter, we can use an array of sensors to estimate the frequency-wavenumber power spectral density (PSD) of the wave field in a plate, that is, to estimate the strength of the different plane waves components of the propagating

field as a function of frequency and wavenumber (i.e. direction), and to identify the principal wave components.

Conventional Spectral Estimation

In the conventional approach, we estimate the PSD as

$$\hat{P}(f,k)=\frac{1}{M^2}\sum_{j,l=1}^{M} w_j w_l^* \hat{r}_{jl}(f)e^{ik(x_j-x_l)} \tag{5.1}$$

In this equation, we assume the array to be parallel to the axis x, M is the number of sensors, w_j and w_l are the weights corresponding to the j^{th} and l^{th} sensors, * represents the complex conjugate, and the $\hat{r}_{jl}$ are the components of the estimated covariance matrix $\hat{R}$ (cross power spectral density).

Denoting the Fourier Transform of the output of the j^{th} sensor as S_j, the simplest estimate of $\hat{r}_{jl}$ is

$$\hat{f}_{jl}(f)=S_j(f)S_l^*(f) \tag{5.2}$$

In equation (5.1), the delay corresponding to the targeting (scanning) direction is introduced by the exponential term. For narrowband processes, the application of this phase shift is practically the same as applying the delay in the time domain. For broadband signals, on the other hand, this equivalence does not hold, so we must introduce the time shift at the time we estimate $\hat{R}$.

Maximum-Likelihood Method (MLM)

When targeting in one direction, we would like the array to have a zero response at the direction of other interfering plane waves (a value of zero in the beam-former for the direction of the interferences) so these interferences do not contaminate the estimate in the target direction.

If we know the interfering directions, it is always possible to apply sensor weights such that the array response to the interfering waves is minimized; this modification however

may have a negative impact in other wavenumber regions, but as far as we are certain that no components are propagating in these other regions, this should not concern us. With a conventional array, however, the *beam-former* is fixed a priori by the geometry of the array and the selected *spectral weights*. So, as we aim towards one of the components, the array response in the direction of the interfering components will be given by the difference in directions between the interference and the target. This is the main drawback of the conventional approach.

The way out of this problem is to use high-resolution methods or adaptive methods, which attempt to estimate the strength of the signal at the targeted wavenumber while minimizing the effects of interferences and noise. At each targeting direction, the adaptive methods adjust the weights in accord to the whole propagating field so as to minimize the array response to the field components propagating in other directions than the target one.

First reported by Capon[35], the MLM algorithm estimates the signal strength at the desired wavenumber while optimally minimizing any noise field (signals at wavenumbers other than the desired one are treated like noise). Capon applied this method to large-aperture seismic arrays. Since then the MLM has been applied to sonic velocity logging[36], common-midpoint reflection data[37] and marine array refraction data[38].

The MLM chooses the weighting vector $\mathbf{w}$ so as to minimize the beam energy $\mathbf{w}^{+}\hat{R}\mathbf{w}$ subject to the constraint $\mathbf{w}^{+}\mathbf{e}=1$. In these expressions $\hat{R}$ is the estimated covariance matrix, $\mathbf{e}=\left\{e^{ikx_1}, e^{ikx_2}...e^{ikx_M}\right\}^{T}$ represents the ideal plane wave corresponding to the target direction and the + sign denotes the conjugate-transposed vector. The purpose of the constraint is to scale the processing gain for each direction-of-search to unity. The weightings adapt to the data through $\hat{R}$.

The solution of the optimization problem gives the weighting vector

$$\mathbf{w}=\hat{R}^{-1}\mathbf{e}/\mathbf{e}^{+}\hat{R}^{-1}\mathbf{e} \tag{5.3}$$

Substitution of these weights into (5.1) gives the MLM estimate for the PSD

$$\hat{P}(f,k)=\left[\mathbf{e}^{+}\hat{R}^{-1}\mathbf{e}\right]^{-1} \tag{5.4}$$

Estimation of the covariance matrix

The estimation of the covariance matrix from the data is a critical step. The first step in this estimation consists in computing the Fourier Transform at the output of the sensors, and there are two issues that require special consideration here.

First, as noted before, a simple phase shift is not enough to introduce a delay in a broadband signal; instead, we introduce the delay in the time series itself and compute the transform of the time-shifted series. Because the series is sampled, we introduce only discrete values of time-shifts. Then, we pre-multiply the Fourier Transform by an exponential to restore the phase modified by this time shifting operation. And, in the beam-forming step (when we combine the output of the various sensors) we can steer continuously around the phase velocity values corresponding to the discrete time shifts as if dealing with a narrowband process. Second, to improve the main lobe and side lobe properties of the transformation, it is possible and recommendable to apply some time windowing. With these two considerations, the final expression for the Fourier Transform is

$$S_j(f)=e^{-\mathrm{i}2\pi f\tau_j}\int_T^{T+T_w} w(t-T)\,x_j(t+\tau_j)e^{-\mathrm{i}2\pi f t}dt \tag{5.5}$$

In this expression, $w(t)$ is the time window of width T_w, and the leading exponential factor is used to restore the phase to the time shifted integrand.

In addition to time shifting and windowing, there are two additional modifications we introduce in the computation of $\hat{R}$. First, we normalize the covariance matrix

$$\tilde{R}(f,T,S)=\left\{\prod_{j=1}^{M}\hat{r}_{jj}(f,T,S)\right\}^{1/M}\left[\frac{\hat{r}_{ij}(f,T,S)}{\hat{r}_{ii}^{1/2}(f,T,S)\hat{r}_{jj}^{1/2}(f,T,S)}\right] \tag{5.6}$$

Second, we add a small amount of white noise to stabilize the covariance matrix, so that it is always invertible

$$\tilde{\tilde{R}} = \tilde{R} + \varepsilon I \tag{5.7}$$

where ε is a small percentage of $\left\{\prod_{j=1}^{M} \hat{r}_{jj}(f,T,S)\right\}^{1/M}$ and I is the identity matrix.

Frequency-wavenumber spectral estimation in plates

In this section, we combine the modeling tool developed in the first part of this work and the Spectral Analysis techniques described in this chapter to study the effects of cracks in the propagation of waves in plates. Using the 2D numerical tool, we compute the displacements at an array of points on the surface of both cracked and uncracked plates. We then use various combinations of these outputs to estimate the propagating field. Finally we study the impact of different cracks on the propagating field.

Table 3 collects the principal parameters used in the numerical modeling, and Table 4 shows some relevant information about the array processing.

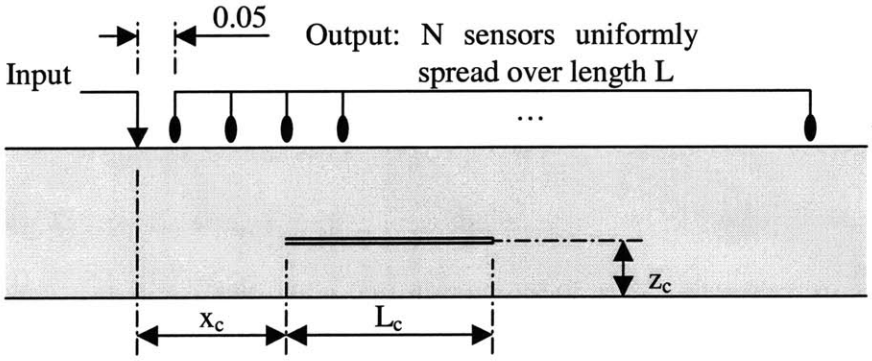

Figure 5-3: Physical description of numerical experiment

Table 3: Modeling parameters

Frequency range:	0-100 kHz (1025 frequency points)
Frequency step:	0.09765625 kHz
Imaginary component of frequency:	0.05 kHz
Discretization:	160 quadratic layers
Plate Thickness:	0.2 m
Density:	1
Shear velocity:	2.0 m/ms
Poisson's Ratio:	0.25
Damping:	0.1 %
Boundary conditions:	Free-Free
Length of Boundary Elements:	0.0015625 m
Force shaping	Time differentiate of Gaussian pulse
Fourier Transform of input	$e^{-iT\omega}\frac{i\omega}{\sqrt{2\pi}}e^{-\frac{1}{2}\left(\frac{\omega}{S}\right)^2}$, S=125, T=1/25

Table 4: Array-processing parameters

Duration of time series	5.12 ms
Time window shape:	Kaiser-Bessel window
Time window width	2.56 ms
Overlapping	50 %
Frequency range:	0-50 kHz
Frequency step:	0.390625 kHz
Velocity step	0.1 m/ms
Spatial window (only conventional array)	Blackman-Harris

Modes in the plate

First, we present the dispersion curves for the plate, computed via the TLM (Figure 5-4). These curves describe the relation frequency-wavenumber (or phase velocity) for the different propagating modes in the plate and tell us for every frequency which modes propagate and at which phase velocity.

The propagating field in the plate will be a linear combination of the modes corresponding to these curves, and the mayor components (modes) will appear in our array analysis as regions of large energy content aligned with the corresponding dispersion curve. Superimposing these curves on top of the PSD estimate, we are able to infer which modes are predominant in the response of the plate.

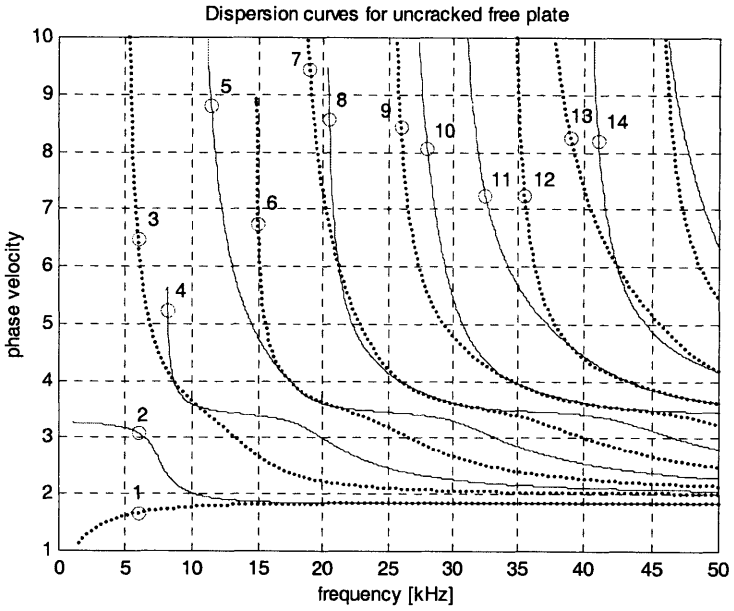

Figure 5-4: Dispersion curves in homogeneous free plate

Each dispersion curve is associated with a modal shape, or mode. These modal shapes describe through-the-thickness motion profiles that propagate along the axis of the plate with frequency and phase speed given by the dispersion curves.

We show in Figure 5-5 and Figure 5-6 the shear and normal stresses corresponding to the first fourteen modes at the locations marked in the dispersion curves in Figure 5-4.

Information regarding the level of stresses at the depth of the crack is of interest to understand the response of a delaminated plate.

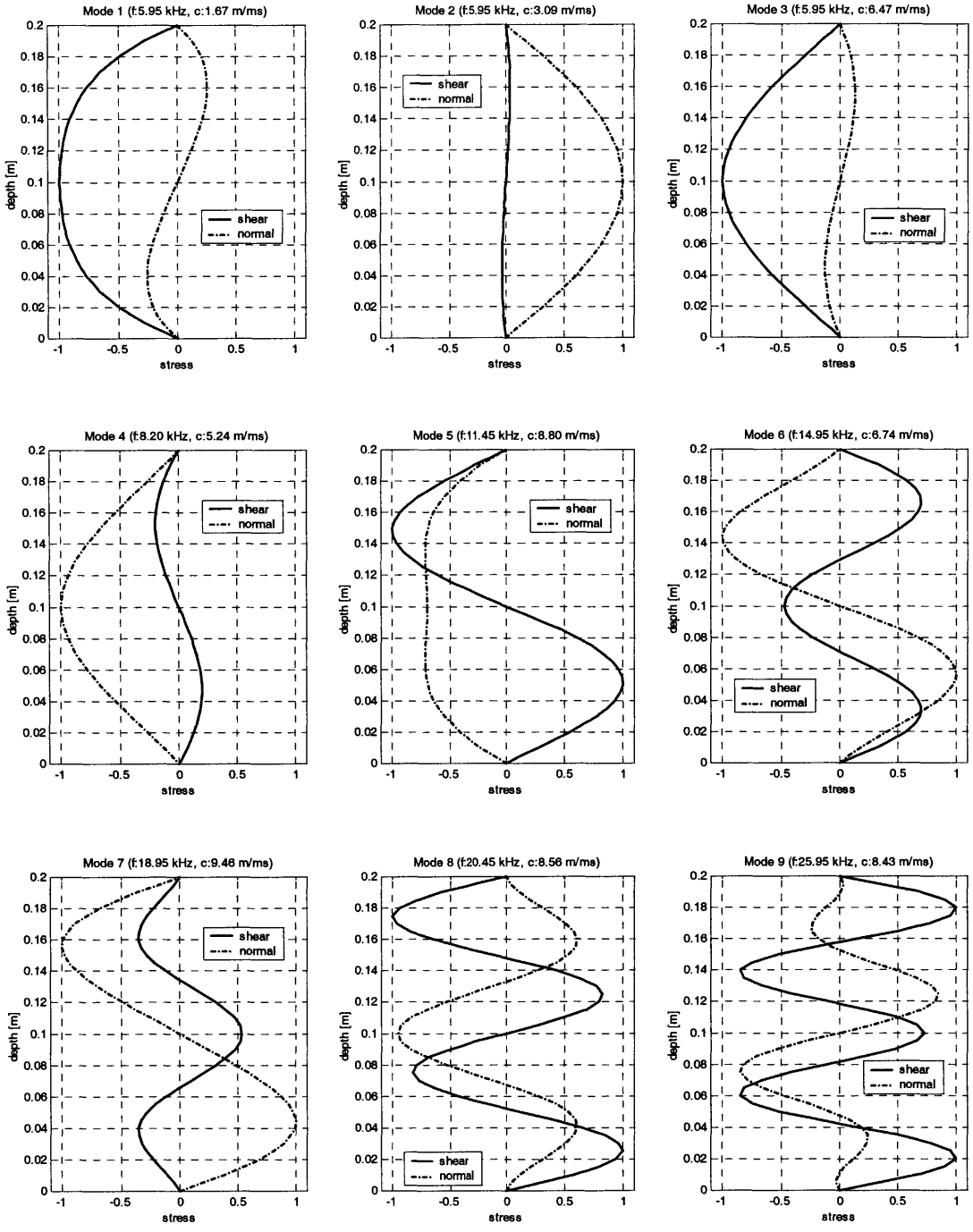

Figure 5-5: First nine modes of homogeneous plate

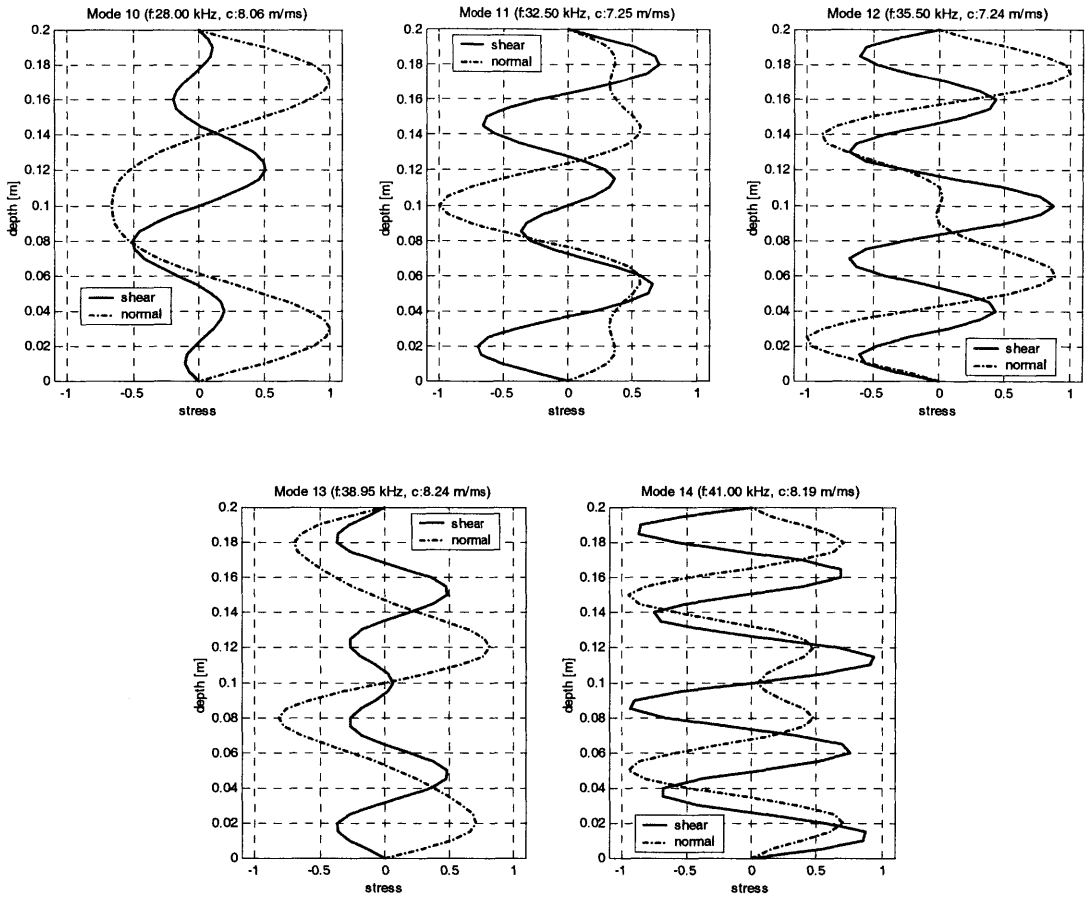

Figure 5-6: Modes ten to fourteen of homogeneous plate

Time histories

Next, we present some *waterfall* plots with the time histories computed at 64 sensors spaced uniformly between the epicentral distances of 5 cm. and 201.875 cm.

The response at any point in the surface of the plate is a combination of direct waves and reflected waves. Direct waves are those that travel in a straight path from the source to the output point, and reflected waves are those who reach the output point after one, two or several reflections on the boundaries of the plate.

There are three direct waves, one dilatational, one distorsional and one surface wave which is confined only to the surface and does not propagate into the body of the plate. The dilatational wave is the fastest and thus the first one to arrive to the output; however, the vertical motion for points on the surface due to this wave is very small and often

negligible. The distortional and the surface wave propagate at similar velocity and except for very large epicentral distances, they overlap in time. The surface wave causes the largest vertical motions for points on the surface. On the one hand, it captures the largest share of energy for vertical impacts on the surface (e.g. 67% for elastic half space with 0.25 Poisson's ratio[39]); on the other hand, it attenuates slower than the body waves as it is confined to the surface. In the waterfalls in Figure 5-7 to Figure 5-10, the arrival of the surface wave at the different sensors appear aligned along a straight line as the most noticeable arrival in these time series. The presence of the crack for Figure 5-8 to Figure 5-10 affects only slightly the surface wave.

The reflected waves make up the rest of the response at the surface. For points close to the source, the direct waves arrive before the reflection, as they follow a shorter path. As the epicentral distance increases the high velocity of dilatational waves offset the difference in path length and for large epicentral distances, there are reflections that arrive before the surface wave. In Figure 5-7 to Figure 5-10, we can see these early arrivals. For the closest sensor, the surface wave is the first noticeable arrival. As distance increases, the first reflection of the dilatational waves arrives in advance of the surface wave. For the furthest sensors, there are several reflections arriving before the surface wave.

We can also observe in these waterfalls several coherent arrivals after the surface wave. These arrivals are affected by delaminations. Thus, the response of the delaminated plate in Figure 5-8 looks very similar to that of the undamaged plate in Figure 5-7. However, closely inspection shows that the arrivals following the surface wave in these figures occur at different times. In addition, we can observe on the bottom series (sensors close to the source) of Figure 5-7 to Figure 5-10 simultaneous arrivals due to vertical dilatational reflections from the opposite surface of the plate.

For the plate without a delamination (Figure 5-7), these coherent arrivals are always tilted to the right (propagating away from the source). In the delaminated plates, there are also arrivals tilted to the right (propagating towards the source) due to waves back scattered from the crack. These are most noticeable in Figure 5-9.

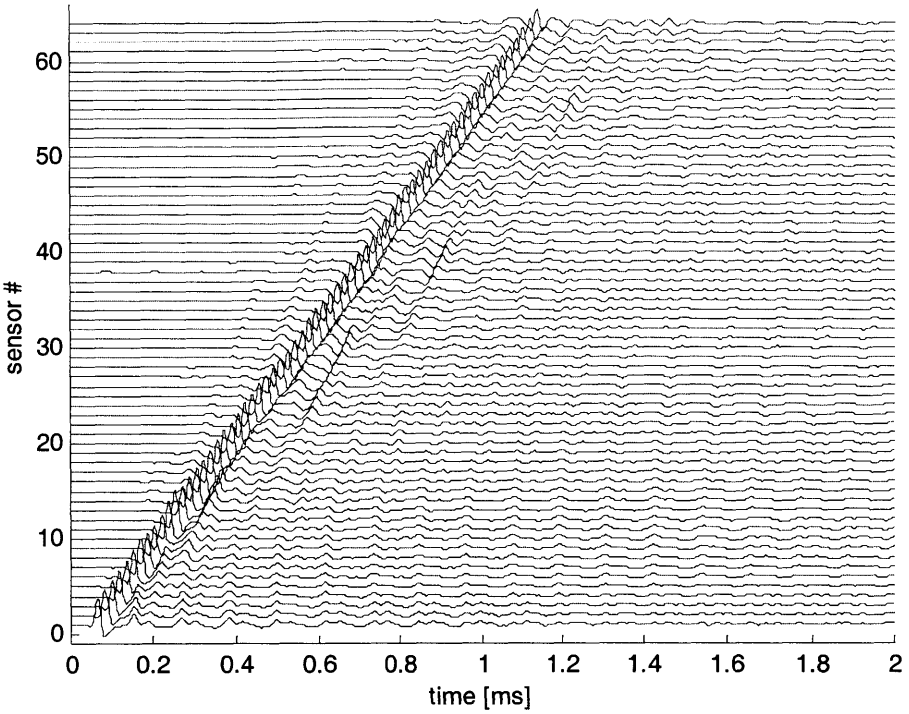

Figure 5-7: Time series in plate with no delamination

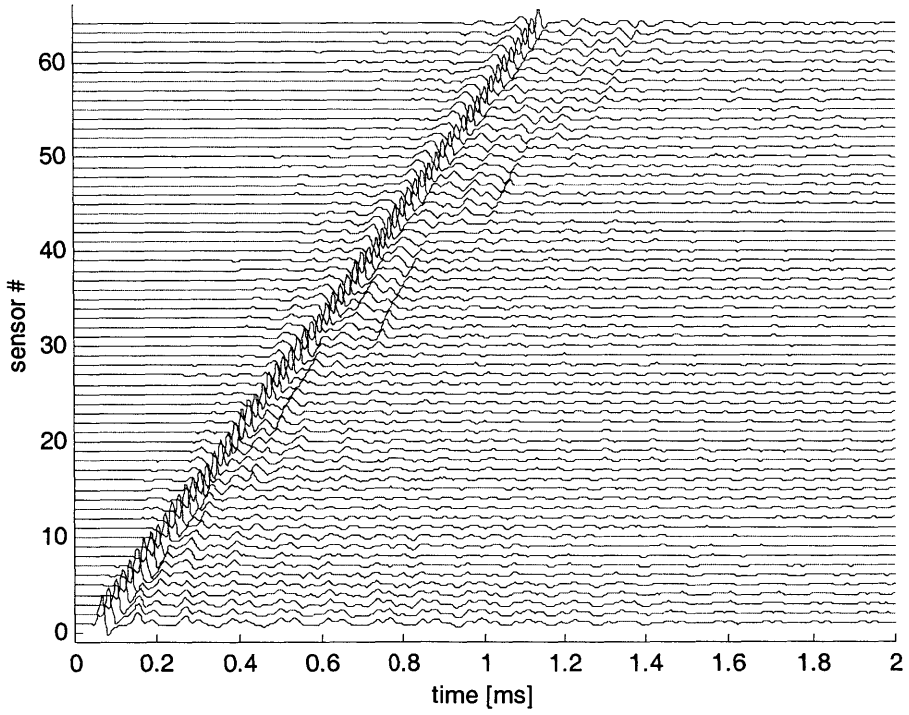

Figure 5-8: Time series for middle delamination (x_c: 0.3, z_c: 0.1, L_c: 0.2)

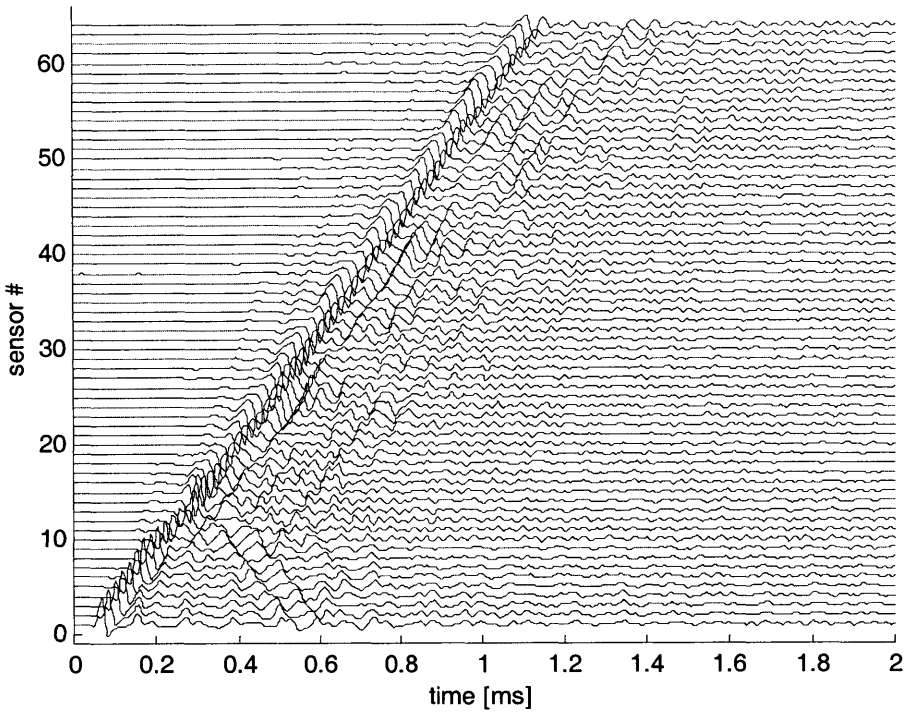

Figure 5-9: Time series for shallow delamination (x_c: 0.3, z_c: 0.15, L_c: 0.15)

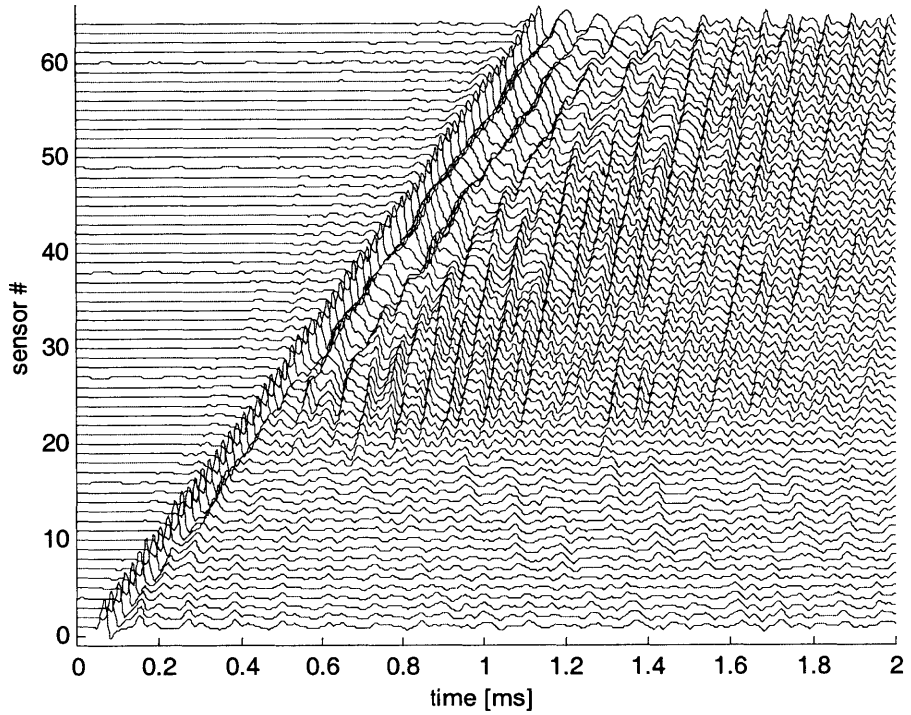

Figure 5-10: Time series for deep delamination (x_c: 0.5, z_c: 0.05, L_c: 0.3)

Plate without crack

The first model we consider is that of a plate without a crack. We use this model to study how the geometry of the array (total length and spacing between sensors) affects its performance, and to compare the two approaches to estimate the PSD: the conventional and the MLM.

We consider in our analysis arrays of two different lengths: one and two meters. For a conventional array, we can estimate its resolution in terms of phase velocity as

$$\Delta c = c^2 \, BW_{NN} / (2\omega L) \tag{5.8}$$

where c and ω are the phase velocity and frequency at the point where we estimate the PSD, BW_{NN} is the width of the main lobe of the beam-pattern and L is the total length of the array.

Consider the point of coordinates (15 kHz, 3 m/ms). Reading the value of BW_{NN} in Figure 5-2 (approximately 24) and substituting into (5.8), the one-meter array gives a resolution of 1.15 m/ms and the two-meter array half this value. Therefore, the short array would not be able to resolve modes three and four (see Figure 5-4) at 15 kHz, and the two-meter long array will barely do it. Testing for different locations, we conclude that the one-meter conventional array does not provide enough resolution for meaningful results, and the two-meter array constitutes just a small improvement. Figure 5-11 to Figure 5-14 further confirm these fact. In addition, we would like the waves to propagate all the length of the array, and given the material damping in concrete and the geometric dispersion of the propagating waves, two meters is already quite a long array.

On the other hand, the MLM provides a much higher resolution regardless of the length of the array; the MLM estimates of the PSD show large concentrations of energy tightly packed around the dispersion curves (Figure 5-15 to Figure 5-18). For the short array, the concentration is slightly more smeared than for the long array, but the resolution is still very good. With this type of analysis and for a distance-between-sensors of 6.25 cm (Figure 5-16 and Figure 5-18), we can clearly see some aliasing at the top right corner.

This tells us that 35 kHz is about as far as we can go with 6.25 cm. between-sensors in the spectral analysis of these plates.

The slight discontinuities along horizontal lines that we can see in all eight estimates are due to the discrete time shifts applied when estimating the covariance.

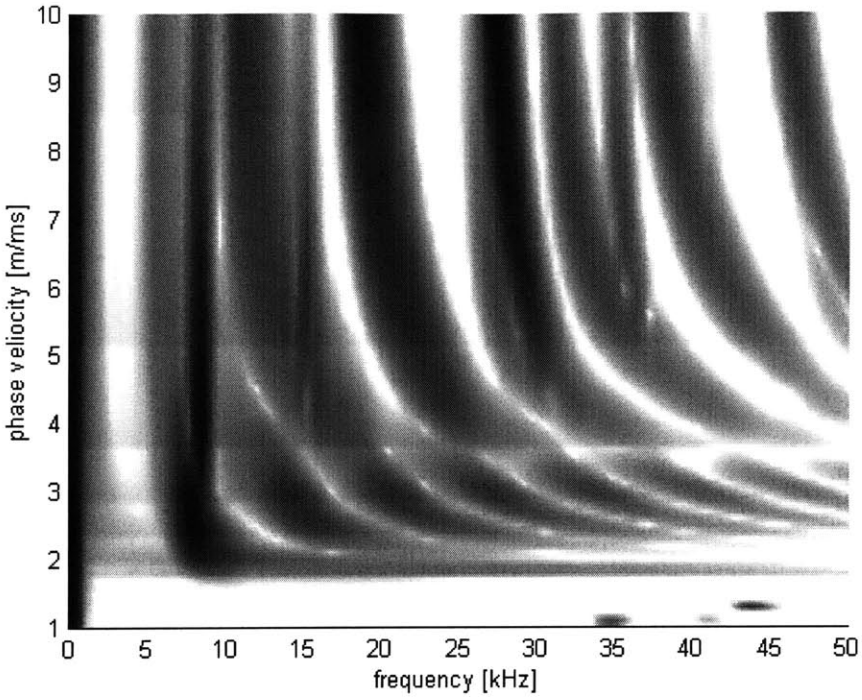

Figure 5-11: PSD for undamaged plate (64-sensor 2-m long array)

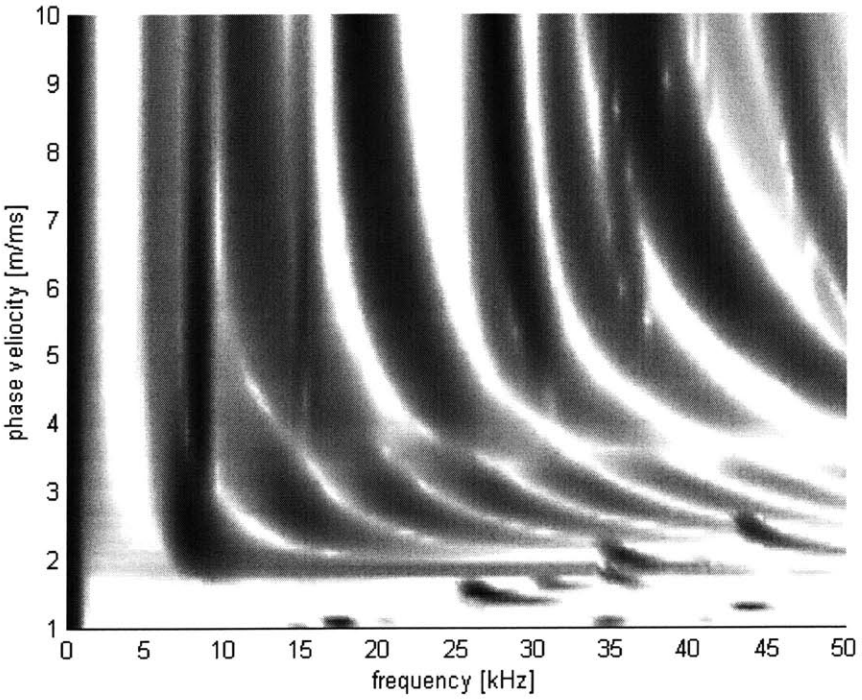

Figure 5-12: PSD for undamaged plate (32-sensor 2-m long array)

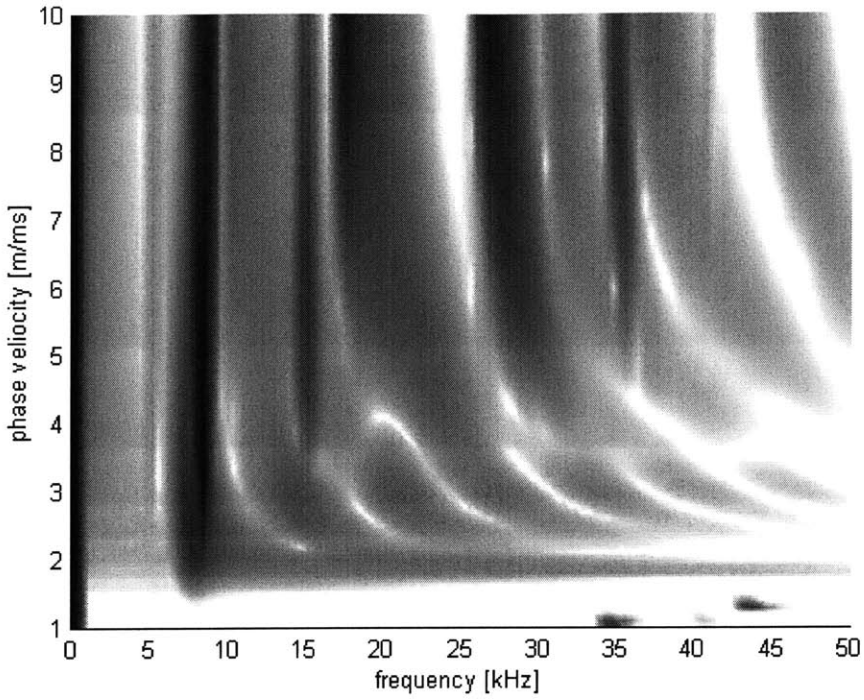

Figure 5-13: PSD for undamaged plate (32-sensor 1-m long array)

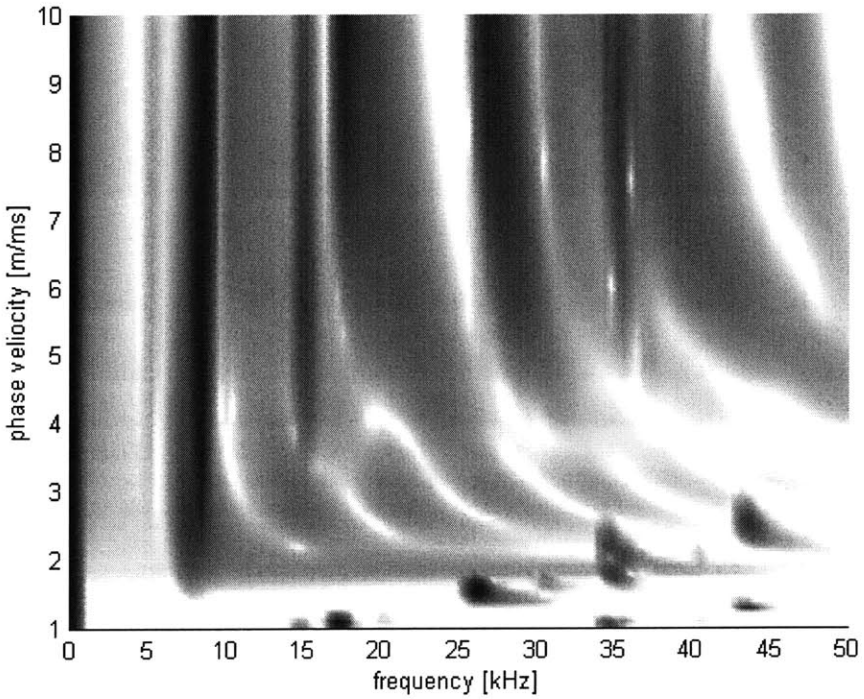

Figure 5-14: PSD for undamaged plate (16-sensor 1-m long array)

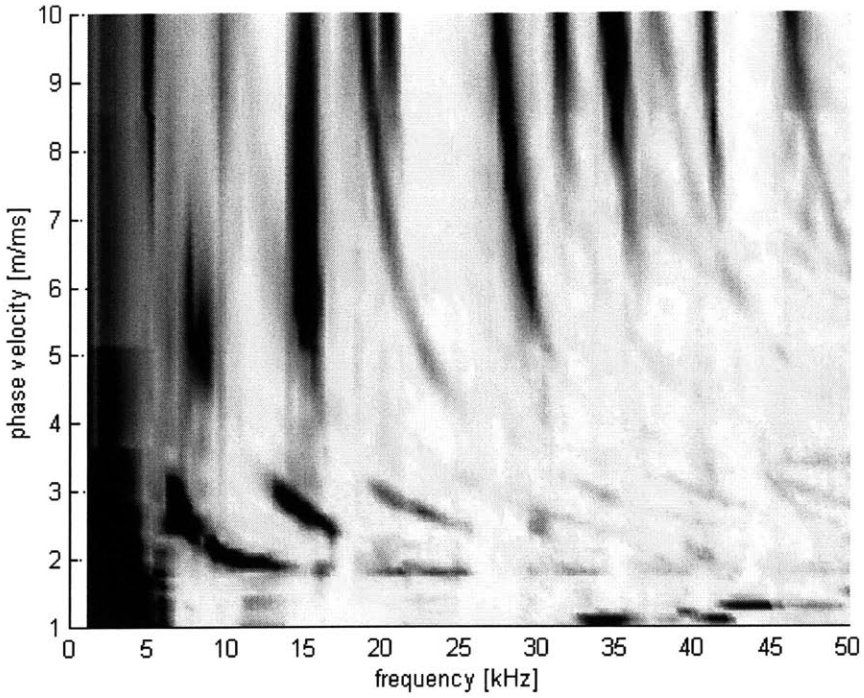

Figure 5-15: MLM estimate for undamaged plate (64-sensor 2-m long array)

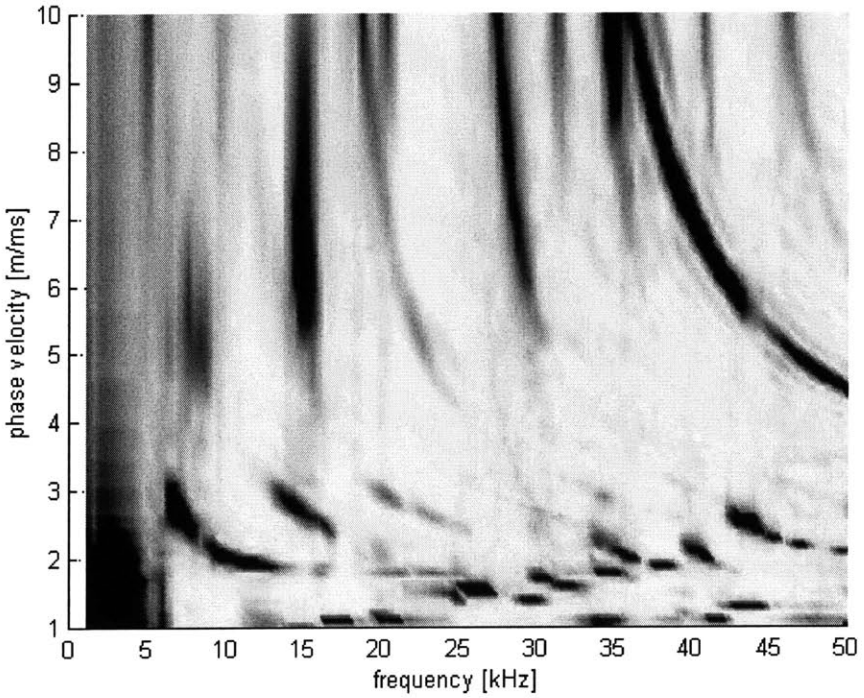

Figure 5-16: MLM estimate for undamaged plate (32-sensor 2-m long array)

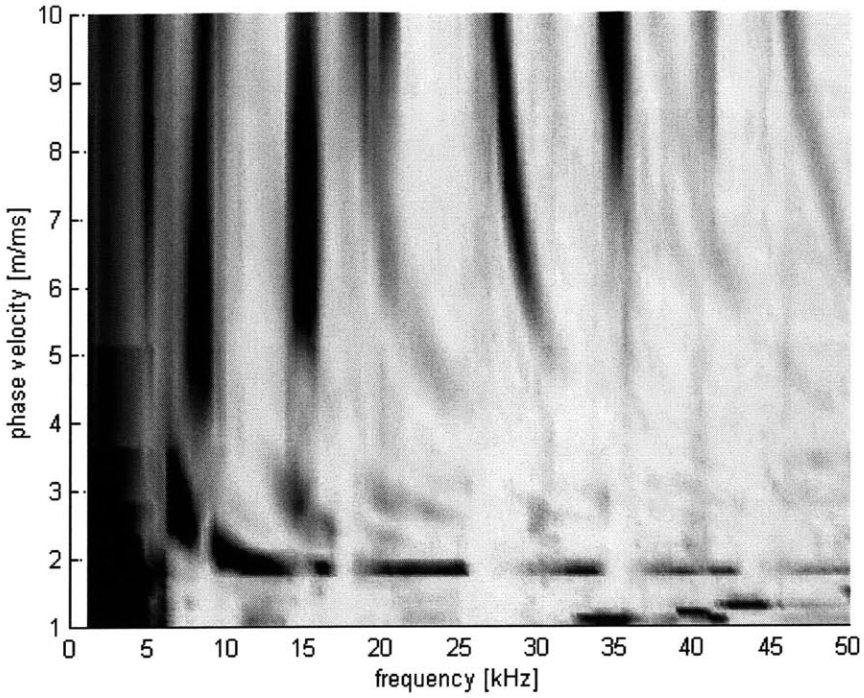

Figure 5-17: MLM estimate for undamaged plate (32-sensor 1-m long array)

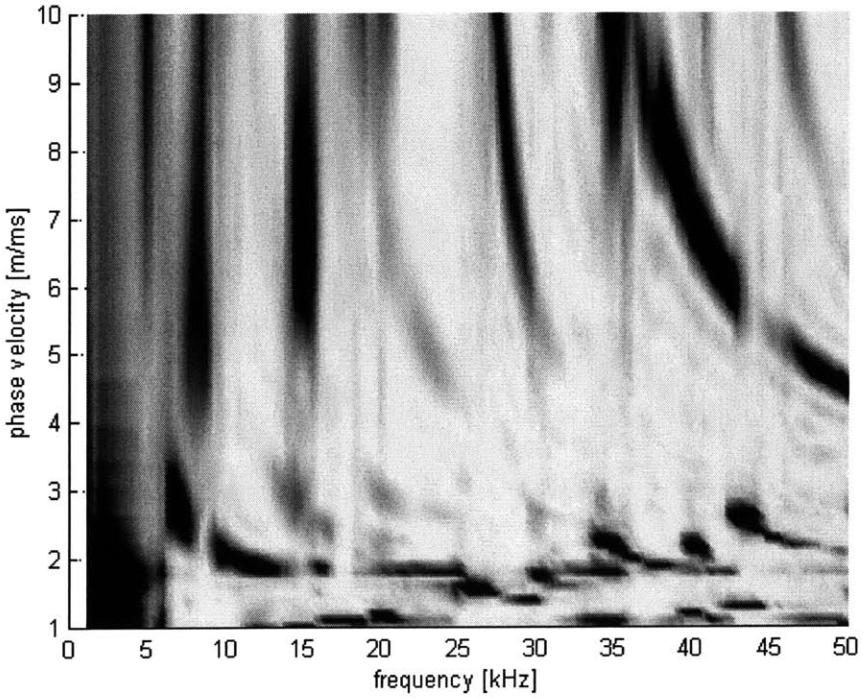

Figure 5-18: MLM estimate for undamaged plate (16-sensor 1-m long array)

Plates with cracks

Our aim in this chapter is to better understand what impact the presence of a crack has on the propagating field in a plate. To this effect, we analyze models with cracks of different size (L_C), distance to the impact source (x_C) and depth (z_C) (Figure 5-3). With the numerical time series obtained from these models, we estimate the PSD using various combinations of sensors (various lengths and number of sensors).

The first clear conclusion concerns the array processing itself. For several cases, we try both the conventional method and the MLM, and find that the MLM shows consistently better performance.

Our analyses clearly indicate that the presence of a crack elicits mode conversion in the plate: on the one hand, it excites modes that would otherwise not have been excited in absence of the crack; conversely, the crack can diminish the relative strength of otherwise strong modes.

This mode conversion is most clear when we superimpose the theoretical modes on the PSD of the plate with and without crack. Figure 5-19 to Figure 5-22 clearly show how the presence of a crack 0.15 m below the surface excites the fifth and the eighth mode, which can hardly been seen in the response of the undamaged plate. Furthermore, for cracks larger than a minimum threshold, the mode conversion takes place in all the cases tested, but the affected modes vary with the location of the crack.

In addition to this easily identifiable result, when a crack is present the high values on the PSD estimates are more disperse; that is, they are not as tightly located around the dispersion curves as for the uncracked plates. This spreading however is not very significant, and difficult to characterize in an accurate manner. This result is most likely due to the ability of the array to resolve the propagating waves rather than to the propagating field itself.

We model cracks of 5, 10, 15, 20 and 30 cm. In all cases, the size of the crack plays a mayor role on how strong the mode conversion is. For small crack sizes of 5 and 10 cm, less or equal than half the thickness of the plate, the PSD estimates show minor evidence

of mode conversion (Figure 5-19); under real testing conditions, these minor changes should prove hard to identify because of extraneous noises. The mode conversion for the larger sizes, 15cm or more, is a predominant trait in the PSD estimates and can be easily recognized. Furthermore, the larger the crack, the stronger the mode conversion is (Figure 5-20 and Figure 5-21).

The PSD estimates do not show much sensitivity to changes in the distance from the source to the crack (Figure 5-21 to Figure 5-24). There are however two additional aspects to consider here: First, because the wave attenuates as it propagates, as the distance increases, the scattered field gets weaker and therefore harder to identify, much more so if real noise is present. Second, the location of the crack relative to the array matters. As the source-crack distance increases, the number of sensors beyond the crack diminishes. As we explain below, this affects the detectability of the crack on the PSD.

The depth of the crack plays a major role in which modes are affected by the mode conversion. In total, we model four different depths: 2, 5, 10 and 15 cm. measured from the bottom of the plate. The modes excited changed depending on whether the crack depth was 2, 5 or 10 cm (Figure 5-26, Figure 5-25, Figure 5-24). On the other hand, the PSD for cracks 5 cm deep (15 cm from the bottom) were very similar to those for cracks 15 cm deep (5 cm from the bottom) (Figure 5-21 and Figure 5-25). Given the symmetry properties of the modes, this similarity seems reasonable.

It is remarkable how a crack at a depth of 90 % the thickness of the plate can have a significant impact on the propagating field, and can be easily detected using array analysis (Figure 5-26).

With regard to the distance source-crack, if we focus our attention on the scattered field propagating away from the source, as this distance increases and the number of sensors beyond the crack diminishes, so it does the impact of the crack on the total output of the array. Therefore, it becomes harder to identify the crack in the PSD estimates.

One way around this problem, for cracks beyond half the length of the array is to look at the back-scattered field, the field propagating from the crack back to the source after being scattered by it. For a plate without a crack the MLM estimate of the back-scattered

field does not show any major propagating mode (Figure 5-27); this result is expected, because lacking a crack all the energy in the plate propagates away from the source. Conversely, if there is a crack present at a reasonable distance, say > 50 cm, the array unmistakably captures the back-scattered field (Figure 5-28).

In the analysis of an undamaged plate, we are certain that the energy propagates from the source outwards. Therefore, we should only concern ourselves with aliasing due to high frequency-high wavenumber components from the direct field. The same holds true for cracks close to the source, as the back-scattered field does affect only a minor fraction of the sensors.

On the other hand, when focusing the array towards the back-scattered field, the direct field is present in the input to the sensors, and depending on the design of the array, it may appear aliased into the PSD estimate. For instance, Figure 5-29 shows the back-scattered field for an undamaged plate as estimated with a 16-sensor 1m long array. In this figure, we can clearly see two aliases of the first and second mode of the direct field (note that the first two modes overlap over a significant part of the frequency range).

Therefore, despite the fact that it is easy to identify the aliases on the PSD estimates, we should pay special attention to aliasing effects when looking at the backscattered field.

Cracks far from the source can also cause some minor aliasing in the estimates of the direct field.

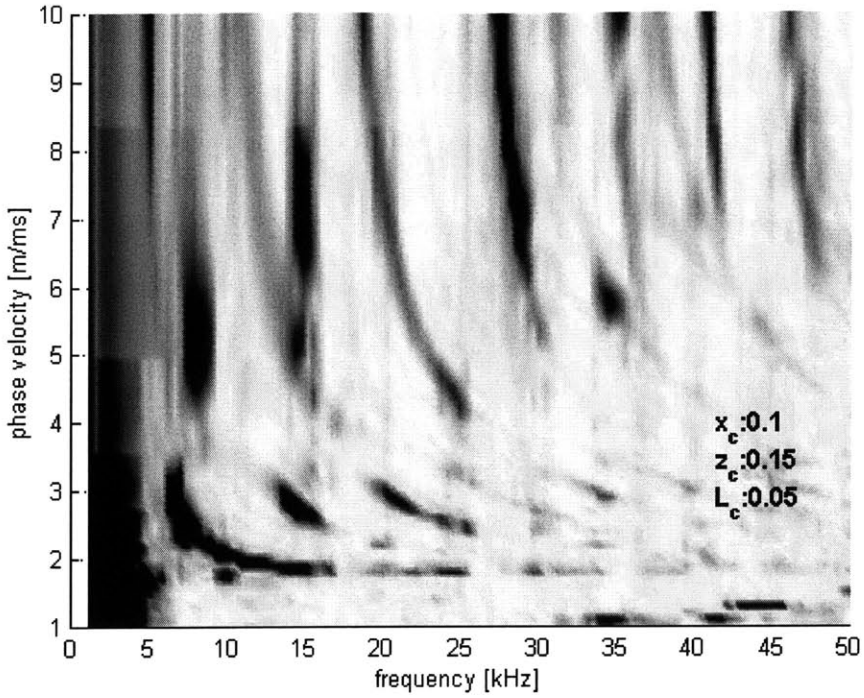

Figure 5-19: MLM estimate with small crack (64-sensor 2-m long array)

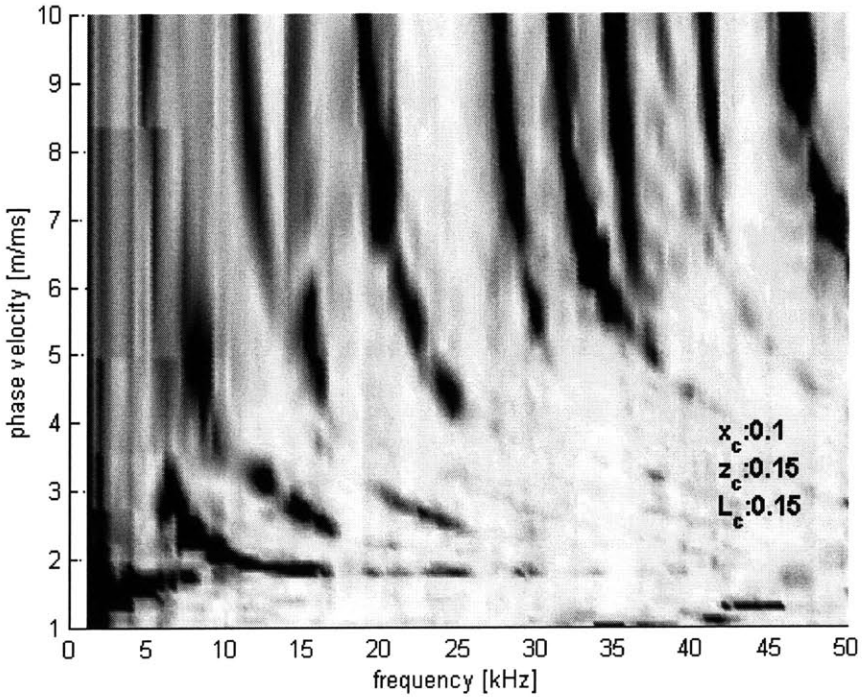

Figure 5-20: MLM estimate with medium crack (64-sensor 2-m long array)

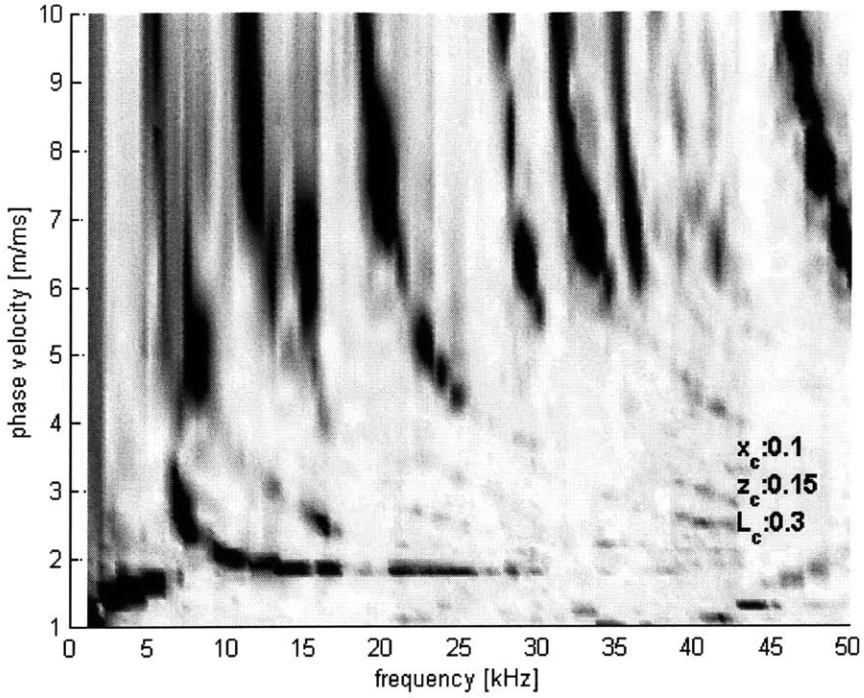

Figure 5-21: MLM estimate with large crack (64-sensor 2-m long array)

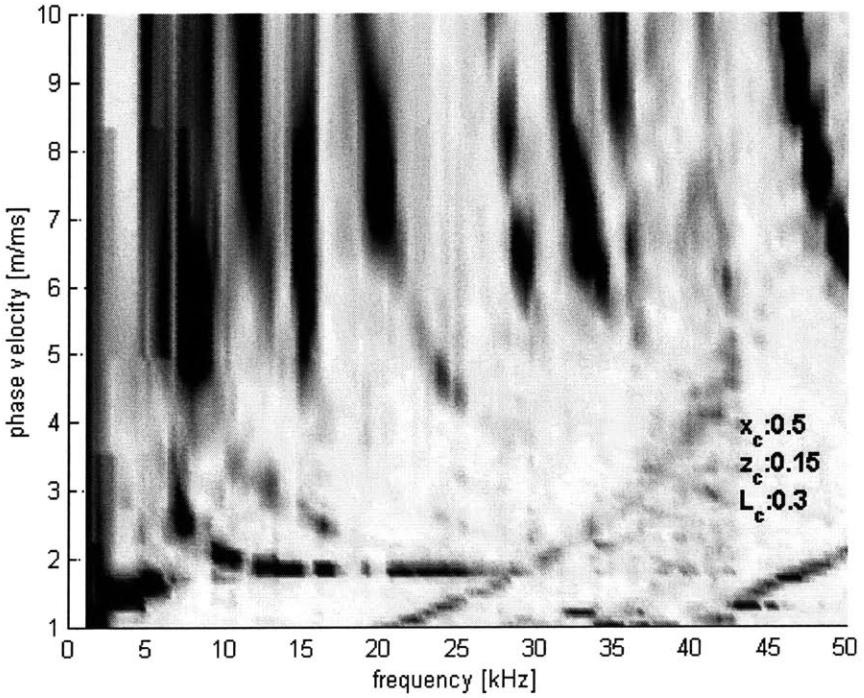

Figure 5-22: MLM estimate with far crack (64-sensor 2-m long array)

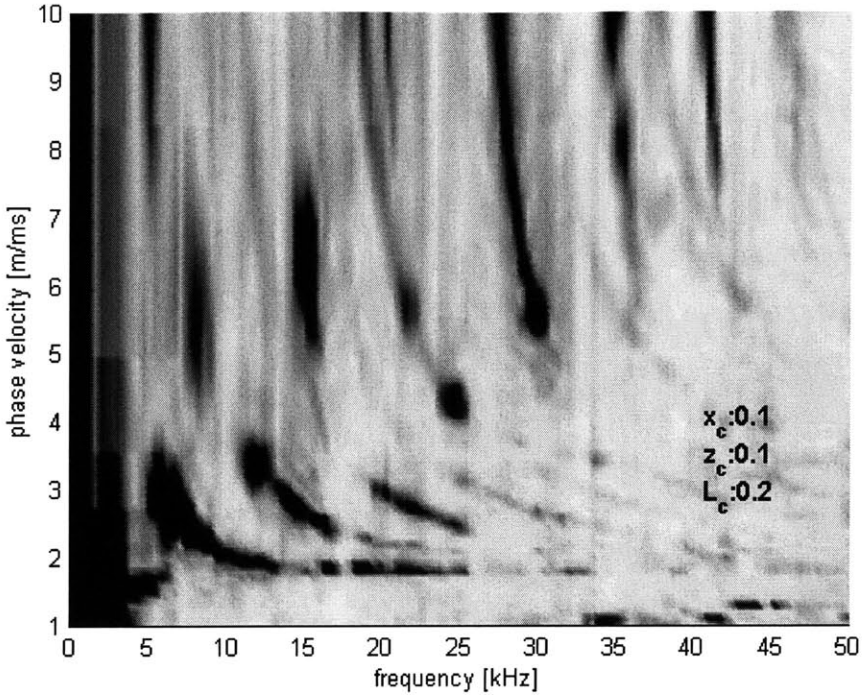

Figure 5-23: MLM estimate with near crack (64-sensor 2-m long array)

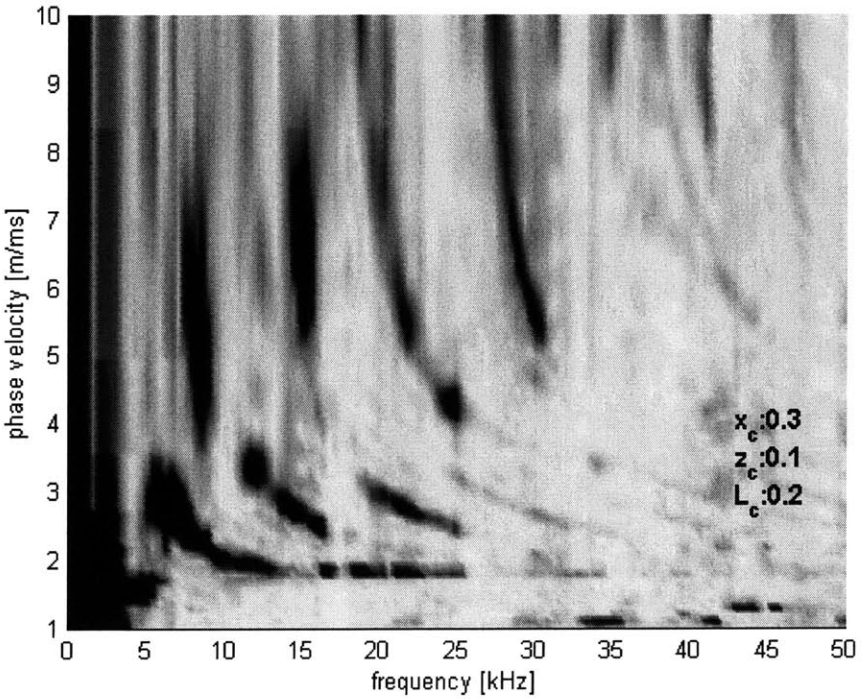

Figure 5-24: MLM estimate with far crack (64-sensor 2-m long array)

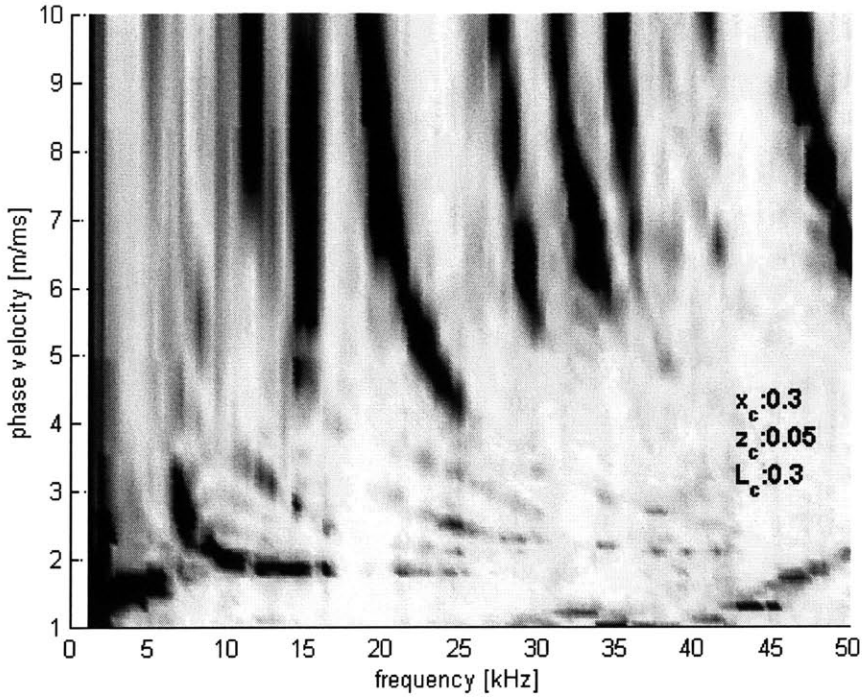

Figure 5-25: MLM estimate with deep crack (64-sensor 2-m long array)

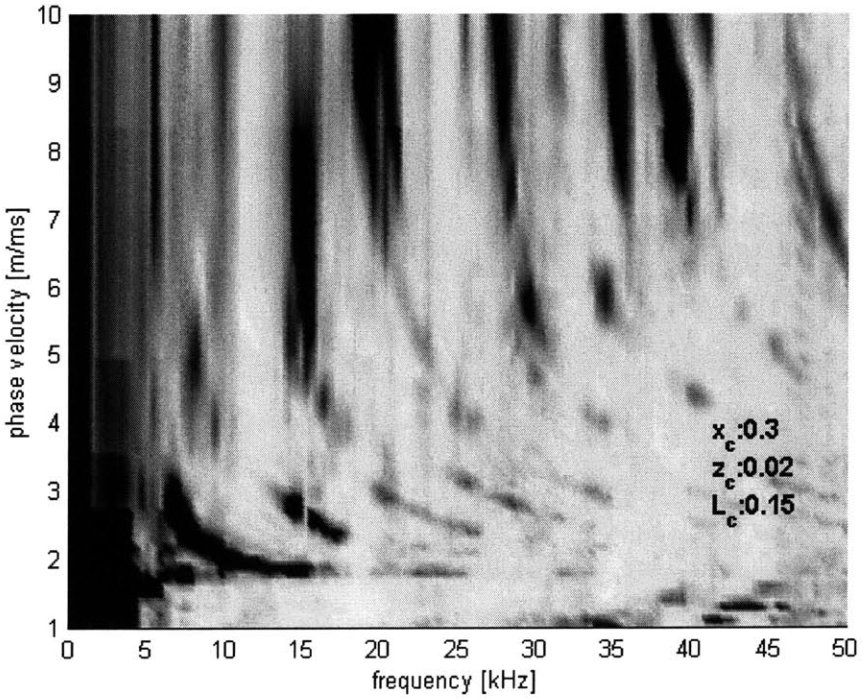

Figure 5-26: MLM estimate with deep crack (64-sensor 2-m long array)

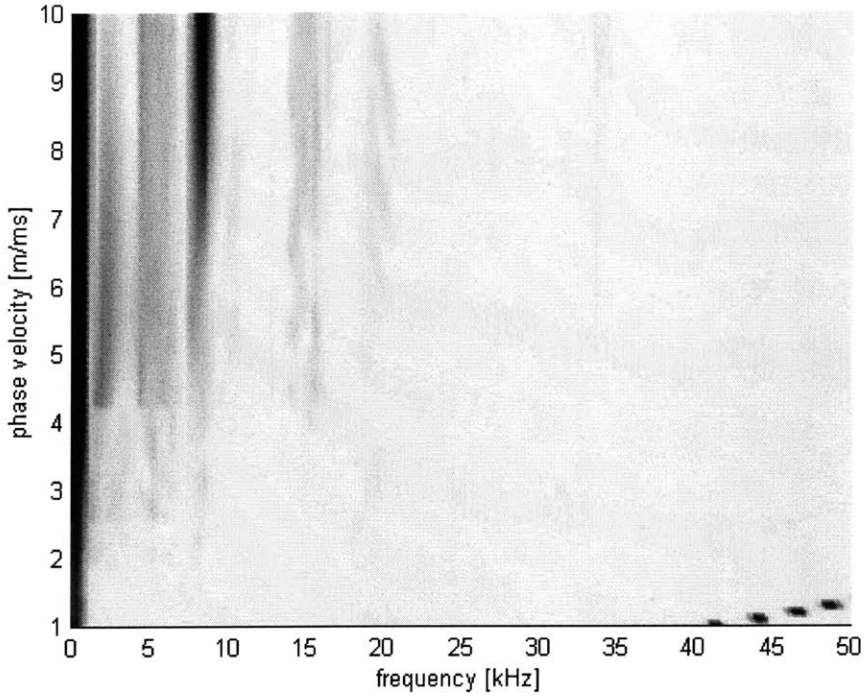

Figure 5-27: Back-scattered field with no crack (128-sensor 2-m long array, MLM)

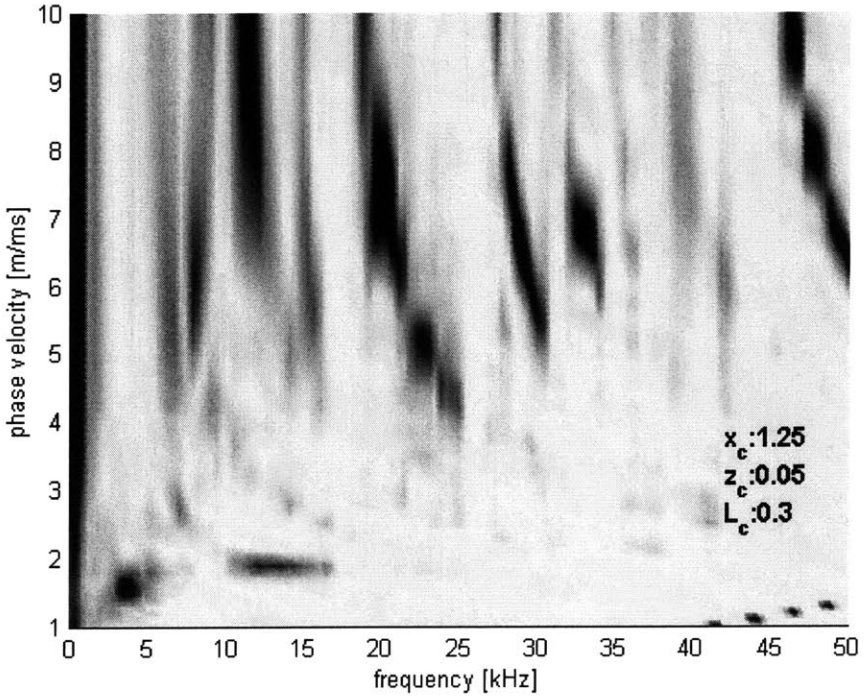

Figure 5-28: Back-scattered field with crack (128-sensor 2-m long array, MLM)

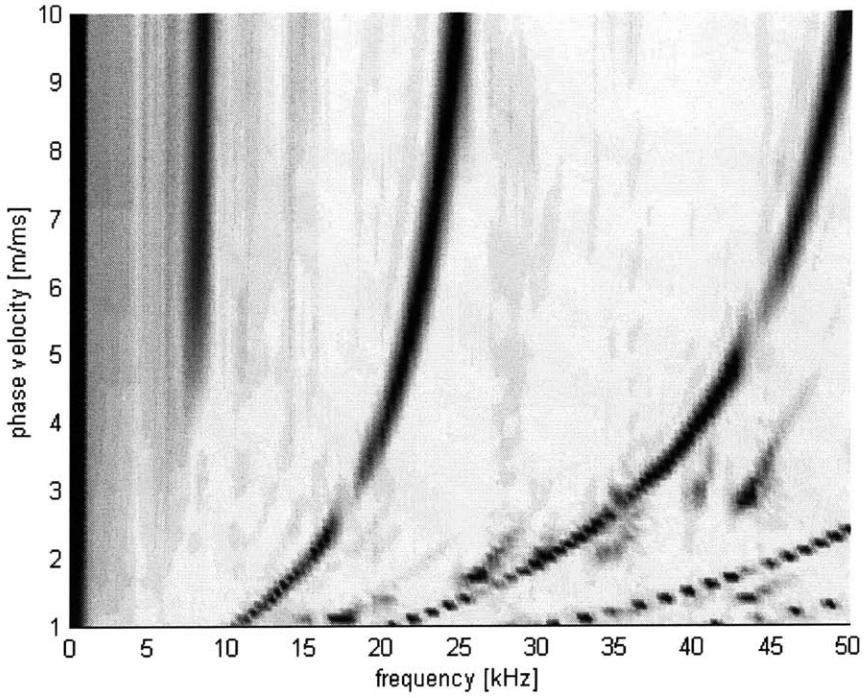

Figure 5-29: Back-scattered field with no crack (16-sensor 1-m long array, MLM)

Chapter 6 :

Numerical Inversion of the W-K Solutions

Introduction

Most well known methods for the study of elastic waves in layered media, excluding the Thin-Layer Method, rely on numerical integration to accomplish the inverse Fourier transformation over wavenumbers. This transformation usually involves complicated improper integrals of the form $\int_0^\infty F(x)\cdot\varphi(r\cdot x)\cdot dx$, in which the complex-valued kernel of these integrals, $F(x)$, represents the flexibility function for the medium at a given frequency. These oscillatory functions often contain sharp peaks elicited by resonances that take place at the characteristic wavenumbers of the normal modes, and their tails usually decay only slowly to infinity (particularly when the source and the receiver are placed at the same elevation in the medium). Thus, these conditions introduce a host of problems that must be resolved for an accurate computation of the improper integrals to be accomplished.

Because the Discrete Fourier Transform uses constant wavenumber steps, it has serious limitations in modeling sharply peaked kernels and rapidly oscillating functions. Numerical integration, on the other hand, allows for tight sampling in the vicinity of the peaks and coarser sampling in the smooth regions away from such peaks. Adaptive integration, however, still requires extensive sampling of the kernels, which involves considerable computational effort. In addition, the highly oscillatory characteristics of $\varphi(r\cdot x)$ call for special integration methods.

To complicate matters further, it is difficult to define adequately the required tolerance without an a priori knowledge of the solution, and an understanding of the shape of the integrands in wavenumber space. For this reason, an alternative method of numerical integration over wavenumbers is taken up in the sections that follow.

Numerical inversion of the transfer function of the single degree of freedom (SDOF) system

The frequency response of a SDOF is a simple function that exhibits a sharp localized peak and is smooth otherwise. Thus, we can use the SDOF as a yardstick to assess the difficulties that can arise in the numerical evaluation of wavenumber integrals for plates.

Our objective here is to compute

$$h(t)=\int_{-\infty}^{\infty} H(f)e^{i2\pi f t}df=\int_{-\infty}^{\infty}\left[1-(f/f_n)^2+i2\xi(f/f_n)\right]^{-1}e^{i2\pi f t}df \tag{6.1}$$

where f_n and ξ are respectively the natural frequency and the damping of the SDOF.

Applying the symmetry properties of the transfer function, the integral can be further transform into

$$h(t)=2\int_0^{\infty}\left[H_R(f)\cos(2\pi f t)-H_I(f)\sin(2\pi f t)\right]df \tag{6.2}$$

where $H_R(f)$ and $H_I(f)$ are the real and imaginary part of the transfer function. We are left thus with two similar real integrals, which we will attempt to compute numerically.

The numerical evaluation of these integrals presents three main obstacles: the oscillatory behavior of the integrand due to the trigonometric function, the highly non-linear behavior of the transfer function in the proximity of the natural frequency, and the infinite extension of the integration interval. In addition, we must bear in mind that for wave problems in layered media what really makes a solution expensive is the cost of evaluating function values in the frequency-wavenumber space. Hence, we should strive to minimize the number of points needed to evaluate these integrals.

As a preliminary step, we divide the complete interval into two intervals separated by a frequency f_o that lies well above the natural frequency. Beyond this value, the transfer function decreases steadily and monotonically to zero. Thus, in the first interval we have the problem of non-linear behavior, and in the second one, the extension to infinity. In

addition, both exhibit the oscillatory problem. Depending on the smoothness of the integrand, further subdivision is required for each interval.

The Clenshaw-Curtis quadrature[40]

A usual approach to approximating numerically the integral of a function $F(x)$ over certain interval, consist in interpolating the function at some points x_0, x_1... within the interval of integration by a polynomial of class P_n. Because of this approximation, the integral transforms into a sum of simple integrals that can be treated analytically. The final expression after evaluating the integrals, which is often referred to as a *quadrature sum*, has the form

$$\int_a^b F(x)\,dx \approx \sum_{j=0}^{N} w_j\, F(x_j) \tag{6.3}$$

where x_0, x_1... and w_0, w_1... are, respectively, the abscissas of the interpolation points and the weights applied at these points.

In general, a *quadrature* provides $2N$ degrees of freedom, namely the choice of the abscissas and that of the weights. However, for a given set of abscissas, it is always possible to find weights such that the quadrature has a degree of precision N, i.e. that is exact for any polynomial of degree $\leq N$. *Quadratures* constructed according to this principle are said to be *interpolatory*, and our interest is usually restricted to this choice. The various *interpolatory quadrature rules* available differ in their choices of abscissas and in the family of approximating polynomials.

Clenshaw and Curtis suggested approximating the integrand $F(x)$ by a truncated series of Chebyshev polynomials. It can be shown that if $f(x)$ is continuous and bounded in the interval $[-1,1]$, then it may be approximated as a convergent series of the form

$$f(x) = \frac{1}{2}\cdot a_0 \cdot T_0(x) + \sum_{n=1}^{\infty} a_n \cdot T_n(x) \tag{6.4}$$

In this expression, T_0, T_1... is the family of *Chebyshev* polynomials and a_0, a_1... are constants given by the following expression

$$a_n = \frac{2}{\pi}\int_{-1}^{1}\frac{f(x)T_n(x)}{\sqrt{1-x^2}}dx = \frac{2}{\pi}\int_0^{\pi} f(\cos\theta)\cos(n\theta)\,d\theta \tag{6.5}$$

The sequence a_0, a_1... usually decreases very fast, and the *Chebyshev* approximation up to the term in N, is a polynomial of degree N or less which is very close to the optimal approximation in the sense that it has the smallest maximum deviation from the true function.

For a general type of function, the constants cannot be evaluated in closed form; instead, they are approximated applying a trapezoidal rule. The final expression for the *Chebyshev* approximation is

$$f(x) \approx \sum_{n=0}^{N}{}''\alpha_n T_n(x) = \frac{1}{2}\alpha_0 T_0(x) + \sum_{n=1}^{N-1}\alpha_n T_n(x) + \frac{1}{2}\alpha_N T_N(x) \tag{6.6}$$

$$\alpha_n = (2/N)\sum_{j=0}^{N}{}''f(x_j)T_n(x_j) = \sum_{j=0}^{N}{}''f\left[\cos(\pi j/N)\right]\cos(\pi jn/N) \tag{6.7}$$

Replacing the integrand on the left hand side of (6.3) with this expansion and integrating term by term, we obtain a new *Chebyshev* expansion

$$\int_{-1}^{x} f(x)\,dx = \sum_{n=0}^{N+1} A_n T_n(x) \tag{6.8}$$

$$\begin{gathered} A_n = (\alpha_{n-1} - \alpha_{n+1})/(2n) \qquad N > n > 0 \\ A_N = \alpha_{N-1}/(2N) \\ A_{N+1} = \alpha_N/\left[4(N+1)\right] \\ A_0 = \sum_{n=1}^{N+1}(-1)^{n+1} A_n \end{gathered} \tag{6.9}$$

The evaluation of this series for $x = 1$ gives the approximation of the integral over the whole interval.

Use of the *Chebyshev* approximation has one additional appeal in the fact that the samples can be reused; that is, given an estimate of the integral with N points, we can improve this estimate by adding N new points to the existing ones. Thus, to find an estimate with $2N$ points, we do not need to waste the N previous samples. This also applies to the modified version of the Clenshaw-Curtis quadrature that follows.

Integration of rapidly oscillatory functions

Because of the oscillatory term, the integrand of a Fourier Integral Transform does not generally resemble a low-degree polynomial, especially for high values of the arguments of the oscillatory terms. For standard quadrature rules to yield good numerical accuracy, it is necessary to partition the whole interval of integration into numerous small sub-intervals, within which a dense set of integration points is used. Furthermore, because we may be interested in the response at different times (different degrees of oscillation), the sampling at one time may not be adequate for other times. Being, as we are, interested in minimizing the number of samples required from the transfer function, we need an alternative.

Piessens and his co-workers suggest a modified Clenshaw-Curtis algorithm to evaluate integrals of the form

$$\int_a^b F(x)\varphi(x)\,dx \tag{6.10}$$

where only $F(x)$, the transfer function in our case, is approximated with *Chebyshev* polynomials, and $\varphi(x)$ is a function with some special behavior, either singular or trigonometric, e.g. $\varphi(x)=\cos(k\cdot x)$. Xu and Mal[41] apply this approach to compute wavenumber integrals, as follows.

Making a variable change such that the interval of integration extends from ∓ 1, and expanding the real part of the transfer function, the first integral in (6.2) transforms into

$$\int_a^b H_R(f)\cos(r f)\,df = A\,\mathrm{Re}\left[e^{irB}\sum_{m=0}^{N} C_m I_m(rA)\right] \tag{6.11}$$

In this equation, $r=2\pi t$, $A=(b-a)/2$, $B=(a+b)/2$, $x=A\cdot z+B$, C_m are the *Chebyshev* coefficients that result from the expansion of H_R, and I_m are the modified moments of the exponential function with respect to the *Chebyshev* polynomials

$$\begin{aligned} C_m &= (2/N)\sum_{k=0}^{N}{}'' H_{Rk}\cos(mk\pi/N) \\ I_m &= \int_{-1}^{1} T_m(z)e^{irAz}dz \end{aligned} \tag{6.12}$$

The first three modified moments are

$$\begin{aligned} I_0(x) &= 2\sin x/x \\ I_1(x) &= 2(\cos x-\sin x/x)/(ix) \\ I_2(x) &= 2\sin x/x+8(\cos x-\sin x/x)/(x^2) \end{aligned} \tag{6.13}$$

Higher modified moments can be computed with the following recurrence law (Xu & Mal)

$$\begin{aligned} I_{m+1}(x) &= \frac{i2(m+1)}{x}I_m(x)+\frac{(m+1)}{(m-1)}I_{m-1}(x)-\frac{4\sin x}{x(m-1)} && m \text{ odd} \\ I_{m+1}(x) &= \frac{i2(m+1)}{x}I_m(x)+\frac{(m+1)}{(m-1)}I_{m-1}(x)+\frac{4i\cos x}{x(m-1)} && m \text{ even} \end{aligned} \tag{6.14}$$

The same procedure can be used for the integral involving the sine.

Xu and Mal make two warnings concerning this method. First, for very low values of the product *rA* (either very small intervals or small values of *r* or both) the recurrence for the moments gives numerical precision problems. Under these circumstances, we can use the original *Clenshaw-Curtis method*, as the function behavior within the integration interval will be only slightly oscillatory. Because of the negligible oscillatory behavior, the data points to approximate the integrand in the Xu&Mal quadrature are the same as those for the *Clenshaw-Curtis* method and these samples could be reused for larger values of *rA*. Second, for large values of *N*, numerical problems are also likely to occur. Thus, in practice we must define the intervals of integration such that we obtain good

approximations without exceeding a defined maximum number of points. Xu and Mal suggest $N_{max} = 32$.

Integration around a singularity

It is the second warning of Xu & Mal that concern us here. In the proximity of the natural frequencies, the behavior of the transfer function is non-linear and requires tight sampling for a reasonable approximation. Because the reason for this behavior is the existence of poles near the natural frequencies, say at the complex point $z_n = f_n + i\xi$, we would expect that if we multiply the transfer function, $H(f)$, by a factor $(f - z_n)$, a locally smooth function should result. In practice, even a rough approximation to z_n should also lead to a smooth function.

In the light of this observation, we propose here an alternative approach to evaluate the Integral Transform in the proximity of the pole. Instead of isolating the oscillatory term and approximating $H(f)$, we isolate the singularity, find a rough approximation for the pole and approximate $G(f) = H(f)(f - z_n)\cos(r f)$. Figure 6-1 compares both approaches for the same number of sample points: direct approximation of $H(f)$ and approximation of $H(f)(f - z_n)$ with further division by $(f - z_n)$. The modified approximation scheme is unmistakably better, and thus integration with the new approach should converge faster.

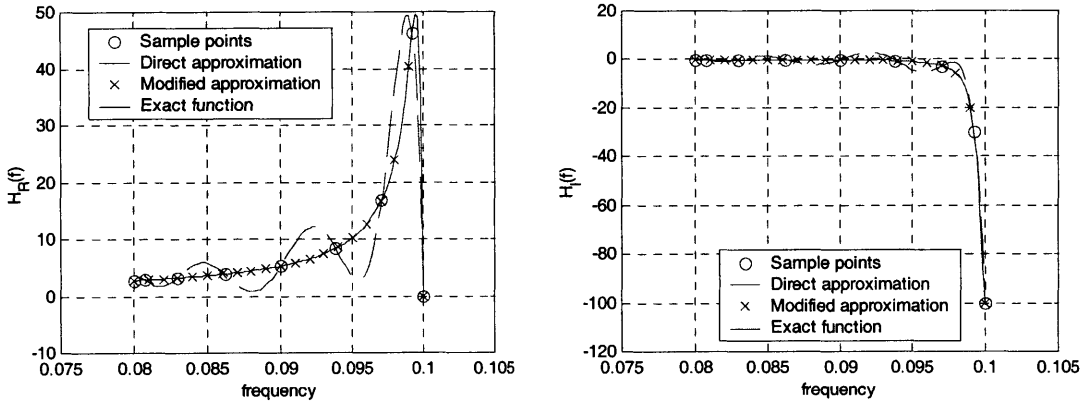

Figure 6-1: Best fit to SDOF transfer function to the left of pole

For the first integral in (6.2), we have

$$\begin{aligned}\int_a^b \mathrm{Re}\{H(f)\}\cos(rf)\,df &= \int_{-1}^{1} \mathrm{Re}\{G(z)/[z-(R+\mathrm{i}I)]\}\,dz \\ &= \int_{-1}^{1} \frac{\mathrm{Re}\{G(z)\}(z-R)}{\left[(z-R)^2+I^2\right]}dz - \int_{-1}^{1} \frac{\mathrm{Im}\{G(z)\}I}{\left[(z-R)^2+I^2\right]}dz\end{aligned} \tag{6.15}$$

where $G(z)=H(z)\cos[k(Az+B)](Az+B-f_n-\mathrm{i}\xi)$, $R=(f_n-B)/A$, $I=\xi/A$, and A and B are as defined above.

The new modified moments with respect to the *Chebyshev* polynomials are then

$$\begin{aligned}I_0^s &= \int_{-1}^{1} \frac{dz}{(z-R)^2+I^2} = \frac{1}{I}\left[\arctan\left(\frac{1-R}{I}\right)-\arctan\left(\frac{-1-R}{I}\right)\right] \\ I_1^s &= \int_{-1}^{1} \frac{z\,dz}{(z-R)^2+I^2} = \frac{1}{2}\left[\ln\left[(1-R)^2+I^2\right]-\ln\left[(1+R)^2+I^2\right]\right]+RI_0^s\end{aligned} \tag{6.16}$$

$$\begin{aligned}I_m^s &= 2/(m-1)+2RI_{m-1}-(R^2+I^2)I_{m-2} && m \text{ even} \\ I_m^s &= 2RI_{m-1}-(R^2+I^2)I_{m-2} && m \text{ odd}\end{aligned} \tag{6.17}$$

Because the oscillatory part has been included within the function to be approximated, the length of interval considered in the proximity of the pole should constitute just a fraction of a whole period. However, except for highly oscillatory integrands (very large times), the non-linear behavior of the transfer function will be far more constraining.

A still unresolved question concerns the estimation of the pole location. The location of the natural frequencies will depend on the physical description of the problem considered, and their estimation requires considerations beyond the scope of this report. Nonetheless, if we know the approximate location of the natural frequency, estimating the imaginary part by fitting two points close to the singularity with the function $K/(f-z_n)$ yields estimates good enough for our purposes (where K is a complex constant). Also, as minor errors in the pole estimation may lead to slopes discontinuity

for $G(z)$ at the natural frequency, it is recommended to consider different integration intervals on either side of the natural frequency.

Numerical Example

To illustrate the concepts elaborated in the preceding, we use the *quadrature rules* presented earlier to evaluate numerically the response of a SDOF whit natural frequency $f_n = 0.1$ and 0.5 % damping.

For this example, we start by assuming the location of the pole unknown and proceed to estimate it. Starting with the values of the transfer function at f=0.05 and f=0.075, we find the exact pole after one iteration. Next, we define two subintervals, one to each side of the pole, whose width is four times the damping. In addition, we define two subintervals to complete the range from f=0 to f=0.2. We consider two more subintervals from f=0.2 to f=2, and we neglect the integral from this last value up to infinity. Within each subinterval, we apply a suitable integration rule with an initial value $N = 2$, and keep on doubling the value of N, up to the maximum value $N_{\max} = 32$, until the desired accuracy is attained. For the first four subintervals, those surrounding the pole, we use the quadrature rule proposed here; for the last two we use the Xu & Mal approach. Within each subinterval, we estimate the error for the approximation of order N as the difference between this approximation and the one of order $N/2$. When this estimate is less than the selected tolerance of 10^{-5}, the approximation of order N is taken as the result and we move to the next interval.

The next figure shows the sparse sampling required around the pole and the time history computed numerically for the first one-and-a-half cycle.

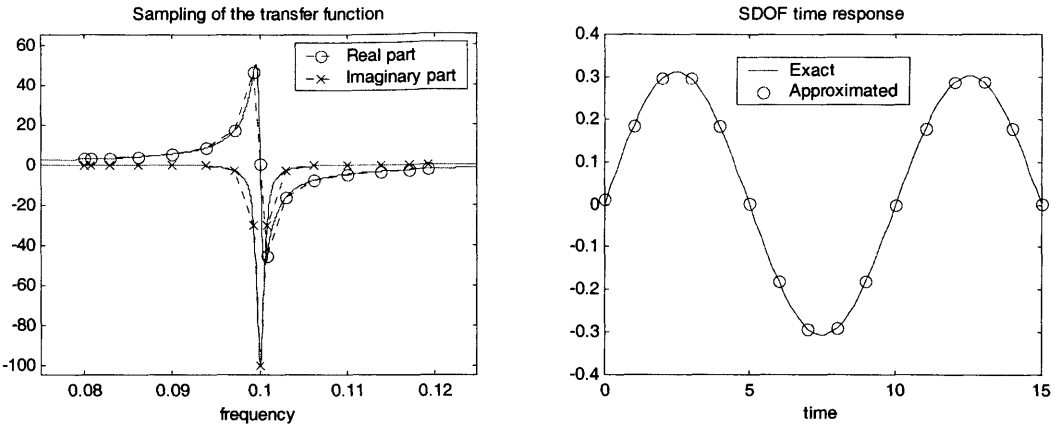

Figure 6-2: Numerical inversion of the SDOF

Two-step inversion of transformed solutions for plates

Given a Thin-Layer model of a plate containing N plane-strain modes, every component of its dynamic flexibility matrix in the transformed domain may be expressed as a linear combination of the form[42]

$$f_{mn} = \sum_{l=1}^{N} \frac{a_l k + b_l}{k^2 - k_l^2} \qquad n,m = 1,2 \ldots N \tag{6.18}$$

We could argue that in the limit, as we increase the number of layers, we recover the continuous system, in which case the values k_1, k_2... become the exact poles of the system and the sum extents over infinitely many modes (i.e. both propagating as well as evanescent modes).

In general, the poles will be close either to the real axis or to the imaginary axis. The latter decay fast with distance, and except for points close to the source, they exert little influence on the plate's response. The poles close to the real axis, on the other hand, constitute the so-called propagating modes, which control most of the response and cause the sharp peaks in the integrand.

In the light of the above, we propose here a two-step strategy to evaluate the numerical inversion of the plate response. In the first step, we use curve-fitting techniques to

estimate the propagating poles and locally approximate the transfer function; then, we invert analytically the approximated poles, and compute a first estimate of the time response as the sum of these inverse transforms. For good pole estimates, the residual left after subtracting the approximated functions should be smooth and very small overall. Thus, except at short epicentral distances, this first estimate should already be very close to the true solution. However, for short epicentral distances or for great accuracy, a second step may be applied where the residual is numerically inverted using *quadrature rules* for oscillatory functions, such as the ones mentioned previously.

The first step generally requires evaluating the transfer function at a reduced number of points; the sharp behavior of the transfer function at the poles provides for a fast fitting process, especially for systems with little damping. As a result, the first clear advantage of this approach is that it provides a very good estimate of the response of the plate after the first step with just a small number of points on the transfer function.

There are three additional advantages. First, the information regarding the poles can be very useful to pre-divide the whole integration interval for the second step, should this be required. Second, the estimate of the response after the first step can help to define more sensibly the required tolerance of the *quadrature*. Finally, because the size of the tail of the residual is significantly smaller than that of the original transfer function, we should be able to interrupt the quadrature at a lower value of the integration variable.

Linear estimation of the poles

The shape of the flexibility function in the proximity of a propagating pole is primarily controlled by the pole itself, while distant poles add just a small contribution. The closer the distant poles are to the real axis (the less damping), the smaller their cross-influence. Thus, we may approximate the flexibility function in the proximity of pole n with a function of the form

$$f(k)=\frac{a_n+\mathrm{i}\,b_n k}{(k-z_n)(k+z_n)}+R_n(k) \tag{6.19}$$

where a_n and b_n are some unknown real numbers, and the function $R_n(k)$ is the result of subtracting the first pole from the original function. We can repeat this process with all the propagating poles and we obtain

$$f(k)=\sum_l \frac{a_l+\mathrm{i}b_l}{(k-\hat{z}_l)\cdot(k+\hat{z}_l)}+R(k) \tag{6.20}$$

Despite its simple appearance, use of equation (6.20) to fit the actual transfer function, where the residual $R(k)$ is some low-degree polynomial, yields non-linear curve-fitting problem, with the non-linearity coming from the residual function, when multiplied by the poles. Given its small value, we may however neglect the residual in a first approach and thus transform the problem into the following, easier and faster-to-solve, linear problem

$$\begin{bmatrix}\mathrm{Re}(f)\\ \mathrm{Im}(f)\end{bmatrix}k^2=\begin{bmatrix}\mathrm{Re}(f) & -2\mathrm{Im}(f)k & 1 & 0\\ \mathrm{Im}(f) & 2\mathrm{Re}(f)k & 0 & 1\end{bmatrix}\begin{bmatrix}\mathrm{Re}(z_l)^2-\mathrm{Im}(z_l)^2\\ \mathrm{Re}(z_l)\mathrm{Im}(z_l)\\ a_l\\ b_l\end{bmatrix} \tag{6.21}$$

Alternatively, we can assume a local behavior for the flexibility function

$$f(k)=\sum_l \frac{a_l+\mathrm{i}b_l+(c_l+\mathrm{i}d_l)k^2}{(k-\hat{z}_l)\cdot(k+\hat{z}_l)} \tag{6.22}$$

and the corresponding linear equation

$$\begin{bmatrix}\mathrm{Re}(f)\\ \mathrm{Im}(f)\end{bmatrix}k^2=\begin{bmatrix}\mathrm{Re}(f) & -2\mathrm{Im}(f)k & 1 & 0 & k^2 & 0\\ \mathrm{Im}(f) & 2\mathrm{Re}(f)k & 0 & 1 & 0 & k^2\end{bmatrix}\begin{bmatrix}\mathrm{Re}(z_l)^2-\mathrm{Im}(z_l)^2\\ \mathrm{Re}(z_l)\mathrm{Im}(z_l)\\ a_l\\ b_l\\ c_l\\ d_l\end{bmatrix} \tag{6.23}$$

Equation (6.23) usually provides a more stable estimation process.

To estimate the poles, we start with two (or three) points in a rough vicinity of a pole and compute a better estimate with equation (6.21) (or (6.23)). We repeat this process until the improvement between two consecutive estimates is below a defined threshold. In addition, once we stop the iteration, we may use the last three or four estimates to make a best fit in the least square sense.

Residual pole

After removal of all propagating poles, the residual that is left exhibits an overall smooth behavior whose maximum value occurs typically at very low wavenumbers. This is consistent with the existence of a pole that is mainly purely imaginary. While we can attempt to integrate this residual directly, an even better strategy is to assume an imaginary pole and estimate it as if it were a propagating pole. The residual left after removing this imaginary pole is still much smaller than the previous one.

Example

Let us consider a free plate subjected to an anti-plane source on its surface. We can then estimate the response at various points on the surface using solely the first step of the approach above, that is, using only the propagating poles and the imaginary pole.

We consider two cases with the same frequency of 5.5 times the principal resonance of the plate and different damping. The estimate for the low damping (0.05 %) is almost exact, and thus it would not be necessary to integrate the residual except at very small epicentral distances. The estimate for the second case is not as good, because the overlapping of the first two poles introduces confounding effects that make their estimation tricky.

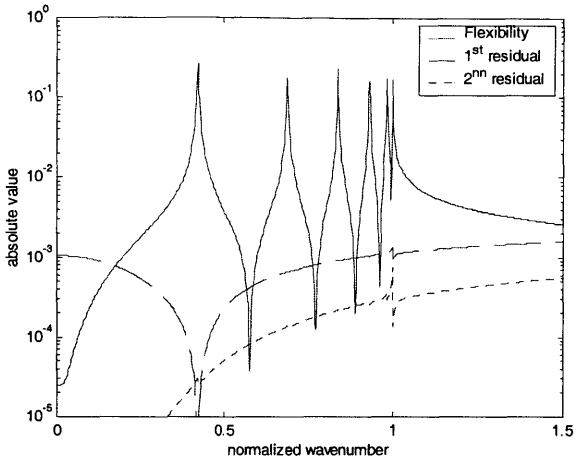

Figure 6-3: Flexibility and residuals for 0.05% damping

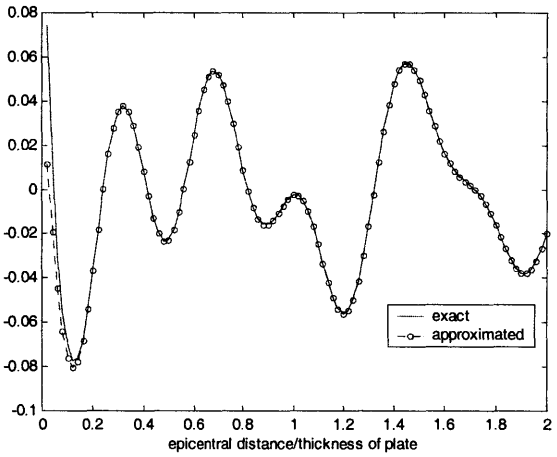

Figure 6-4: Real part of response for 0.05% damping

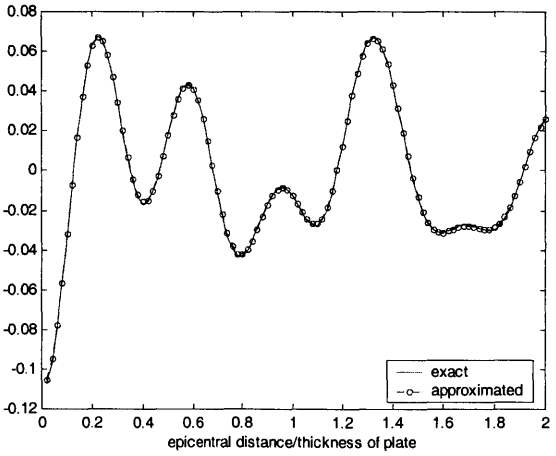

Figure 6-5: Imaginary part of response for 0.05% damping

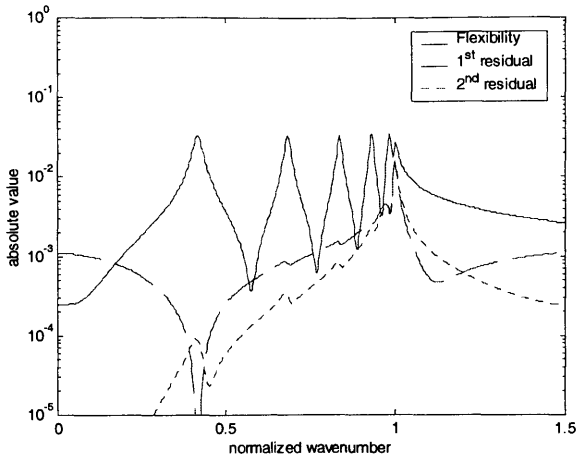

Figure 6-6: Flexibility and residuals for 0.5% damping

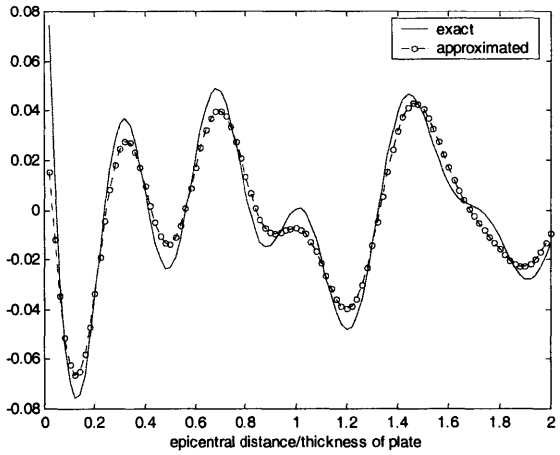

Figure 6-7: Real part of response for 0.5% damping

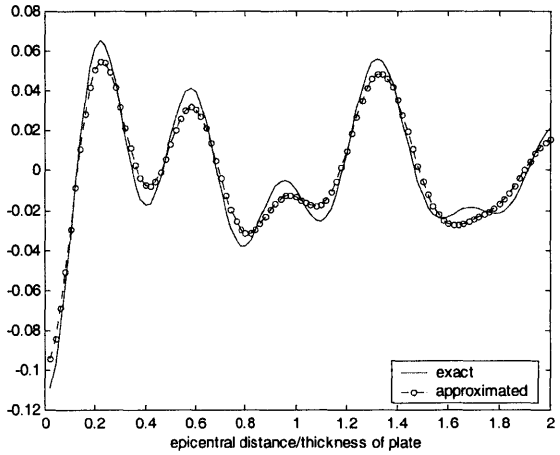

Figure 6-8: Imaginary part of response for 0.5% damping

Conclusions

The complex dynamic response of layered plates is a major obstacle in the development of acoustic NDE techniques.

In understanding and deciphering such response, the accessibility of efficient forward modeling tools can be of crucial value to the analyst. However, standard numerical tools run into important limitations when used to model delaminations in layered plates. The FEM and FDM suffer of important deficiencies when applied to unbounded domains, and require special formulations. The BEM is best suited for unbounded domains, but run into important inefficiencies in heterogeneous domains, such as layered media. In addition, the standard formulation of the BEM degenerates for crack problems.

In the first chapter of this thesis, we present the Traction Boundary Element Equation (TBEM) that is a modified BEM formulation capable of dealing with the scattering due to cracks of zero thickness. The stress fundamental solutions for the full homogeneous space due to line-loads and line-dipoles are the conventional building blocks to study cracks in unbounded media via the TBEM. We present these fundamental solutions for the plain strain cases and propose a simple indirect approach for the analytical evaluation of the hyper-singular integrals that occur in the application of the TBEM. The existence of these integrals is a major obstacle for the proliferation in the use of the TBEM in the engineering practice, and the introduction of simple approaches to their evaluation should always be welcome. We test satisfactorily the adequacy of the TBEM and the hyper-singular integrals evaluation by studying the scattering of plane waves by a Griffith crack and comparing with known analytical solutions.

The second chapter presents some simple solutions to waves propagating in plates. These serve as an introduction to the topic of waves in layered media, and their careful analysis presents some interesting insight about the near field behavior and its convergence for both displacements and stresses. We reflect here on these convergence issues, and propose some acceleration techniques. Though of not much practical interest, the fundamental solutions presented in this chapter can be easily combined with the TBEM to study scattering problems.

In the third chapter of the thesis, we introduce the Thin-Layer Method (TLM), which is a powerful tool for the analysis of waves in layered media. It has already been shown elsewhere the high effectiveness of the TLM to analyze the propagation of waves in layered media. We focus here in the particular aspects regarding with its application to the TBEM: the near field and the computation of stresses. First, we perform various convergence analyses, in which we compare linear vs. quadratic layers and the consistent stresses in the TLM (based on equilibrium), with those obtained by differentiation from the TLM displacements. As expected, the quadratic interpolation gives better results than the linear one for equal total number of degrees of freedom. On the other hand, the consistent stresses are significantly superior to the no-consistent ones, obtaining a degree of accuracy close to that of the displacements for the same total number of degrees of freedom. This interesting result further validates the use of the TLM with the TBEM. Paradoxically, the TLM shows even a faster convergence rate than the continuous modal solutions presented in the previous chapter for the representation of the near field stresses. This can be explained however by the fact that the TLM accepts discontinuities at the thin-layers interfaces, while the modal solutions not. In summary, the performed analyses confirm the adequacy of the TLM as a source of fundamental solutions for the application of Boundary Integral Methods to layered media.

In the next two chapters, we turn our attention to the more practical problem of detecting delaminations in plates. We use the model developed in the previous chapters to simulate plates with different cracks, and with these synthetics, we test different approaches to detect delaminations.

The two most common NDE techniques in concrete plates, sounding and impact-echo, are based in simplifications of the frequency response of delaminated plates when excited on top of the delamination. To better assess the capabilities and limitations of these two methods, we make in the fourth chapter a parametric analysis of this response for cracks of various depths and sizes. Our study shows the large influence of the drum modes (low frequency bending modes) in the response of shallow delaminations, and how the energy in these modes is trapped in the delamination, it does not flow away from it. In addition,

we show that the drum modes carry valuable information about the size of the delaminations.

The analysis with regard to the impact-echo is inconclusive. A significant number of times, the echoes due to delaminations are hard to identify or not present at all. In general, the delamination must be of considerable size (1.5 or 2 times larger than the thickness of the plate at least) to produce a noticeable resonance related to its depth. For very deep cracks, the delamination and the full-thickness resonance overlap. In real test under these conditions, we would most likely see just one peak shifted to the right of the full-thickness frequency. Moreover, sometimes we can still see the full thickness resonance regardless of the crack.

In summary, the response in the low frequency range is the safest bet to detect and estimate shallow cracks. On the other hand, the impact-echo would allow us to identify deep rather large delaminations or thickness-loss over large areas.

In the fifth chapter, we approach the problem of detecting delaminations in plates from a different and somehow new perspective. In this chapter, we use arrays of sensors to decompose the response into the wave-guide modes in the plate and study how delaminations affect the contribution of these modes. These approach present two clear advantages, it allows the scanning of large areas with just one experiments and the underlying mathematical model (modal response of plates) is not a gross local simplification of the plate, but applicable overall and accurate. In the downside, the experimental layout and required signal processing is more involved.

In this chapter, we show the significant impact that a delamination can have on the modes and how the size and depth of the crack modifies this impact. We also show that this approach can detect both far and deep delaminations. Finally, we suggest a procedure to estimate the location of the crack along the axis of the plate.

This novel approach can be very useful for the detection and estimation of cracks, especially when combined with a powerful and efficient forward modeling tool, such as the one developed in this thesis.

References

[1] Cruse, T. A. (1987): *Boundary Element Analysis in Computational Fracture Mechanic*, Dordrecht: Kluwer Academic Publishers

[2] Lachat, J. C. and Watson, J. O. (1976): "Effective Numerical Treatment of Boundary Integral Equations: A formulation for Three-Dimensional Elastostatics", *International Journal for Numerical Methods in Engineering*, Vol. 10, pp. 25-37

[3] Sládek, V. and Sládek, J. (1984): "Transient Elastodynamics Three-Dimensional Problems in Cracked Bodies", *App. math. Modeling*, Vol. 8, pp. 2-10

[4] Sládek, V. and Sládek, J. (1987): "A Boundary Integral Equation Method for Dynamic Crack Problems", *Engineering Fracture Mechanics*, Vol. 27, No. 3, pp. 269-277

[5] Takakuda, K. (1983): "Diffraction of Plane Harmonic Waves by Cracks", *Bulletin of the JSME*, Vol. 26, No. 214, pp. 487-493

[6] Niwa, Y. and Hirose, S.: "Application of the BEM to Elastodynamics in a Three-Dimensional Half Space", *Recent Applications in Computational Mechanics*, D. L. Karabalis (ed.), New York: ASCE, pp. 1-15

[7] Kausel, E. (1981): "An Explicit Solution for the Green's Functions for Dynamic Loads in Layered Media", *M.I.T. Research Report R81.13,* No. 699, Department of Civil Engineering, MIT, Cambridge, MA 02139

[8] Kausel, E. and Peek, R. (1982): "Boundary Integral Method for Stratified Soils", *M.I.T. Research Report R82.50*, No. 746, Department of Civil Engineering, MIT, Cambridge, MA 02139

[9] Eringen, A. C. and Suhubi, E. S. (1975): *Elastodynamics, Vol. 2. Linear Theory*, New York: Academic Press

[10] Paris, F. and Cañas, J. (1997): *Boundary Element Method: Fundamentals and Applications*, Oxford University Press

[11] Wheeler, L. T. and Sternberg, E. (1968): "Some Theorems in Classical Elastodynamics", *Arch. Rational Mech. Anal*, Vol. 31, pp. 51-90

[12] Guiggiani, M. (1998): "Formulation and Numerical Treatment of Boundary Integral Equations with Hypersingular Kernels", *Singular Integrals in Boundary Element Methods*, Computational Mechanics Publications, Southampton (UK) & Boston (USA)

[13] Manolis, G. D. and Beskos, D. E. (1988): *Boundary Element Methods in Elastodynamics*, London: Unwin Hyman

[14] Richardson, J. D. and Cruse, T. A.(1998): "Singular Integrals and their Treatment in Crack Problems", *Singular Integrals in Boundary Element Methods*, Computational Mechanics Publications, Southampton (UK) & Boston (USA)

[15] Mal, A. K. (1970): "Interaction of Elastic Waves with a Griffith Crack", *International Journal of Engineering Science*, Vol. 8, pp. 763-776

[16] Tadeu, A. J. B., Santos, P. F. A. and Kausel, E. (1999): "Closed-form Integration of Singular Terms for Constant, Linear and Quadratic Boundary Elements Part 1: SH Wave Propagation", *Engineering Analysis with Boundary Elements*, Vol. 23, pp. 671-681

[17] Tadeu, A. J. B., Santos, P. F. A. and Kausel, E. (1999): "Closed-form Integration of Singular Terms for Constant, Linear and Quadratic Boundary Elements Part 2: SV-P Wave Propagation", *Engineering Analysis with Boundary Elements*, Vol. 23, pp. 757-768

[18] Kausel, E. (1999): "Dynamic Point Sources in Laminated Media via the Thin-Layer Method" *International Journal of Solids and Structures*, Vol. 36

[19] Abramowitz, M. and Stegun, I. A. (1964): *Handbook of Mathematical Functions*, Dover, New York

[20] Kausel, E. and Roesset, J. M. (1992): "Frequency Domain Analysis of Undamped Systems", *Journal of Engineering Mechanics*, Vol. 118, No. 4, pp. 721-734

[21] Graff, K. F. (1975): *Wave Motion in Elastic Solids*, Dover Publication, Inc., New York

[22] Thomson, W. T. (1950): "Transmission of Elastic Waves Through a Stratified Solid", *Journal of Applied Physics*, Vol. 21, pp. 89-93

[23] Haskell, N. A. (1953): "The Dispersion of Surface Waves in Multilayered Media", *Bulletin of the Seismological Society of America*, Vol. 43, pp. 17-34

[24] Kausel, E. and Roesset, J. M. (1981): "Stiffness Matrices for Layered Soils", *Bulletin of the Seismological Society of America*, Vol. 71, No. 6, pp. 1743-1761

[25] Jensen, F. B., Kuperman, W. A., Porter, M. B., Schmidt, H. (1994): *Computational Ocean Acoustics*, AIP series in Modern Acoustics and Signal Processing, AIP press, New York

[26] Kausel, E. (1981): "An Explicit Solution for the Green Functions for Dynamic Loads in Layered Media", *MIT Research Report R81-13*, Department of Civil Engineering, MIT, Cambridge, MA 02139

[27] Waas, G. (1972): *Linear Two-Dimensional Analysis of Soil Dynamic Problems in Semi-Infinite Layer Media*, PhD Thesis, University of California, Berkeley

[28] Kausel, E. (1994): "Thin Layer Method: Formulation in the Time Domain", *International Journal for Numerical Methods in Engineering*, Vol. 37, pp. 927-941

[29] Kausel, E. (1998): "The Thin-Layer Method in Seismology and Earthquake Engineering", *Wave Motion Problems in Earthquake Engineering*, Computational Mechanics Publications, Southampton (UK)

[30] Sansalone, M. and Carino, N. J. (1989): "Finite Element Studies of the Impact-Echo Response of Layered Plates Containing Flaws", *International Advances in Non Destructive Testing*, Vol. 15, No. 1, pp. 313-336

[31] Sansalone, M. & Carino, N. J. (1989): "Detecting Delaminations in Concrete Slabs with and without Overlays Using the Impact-Echo Method", *ACI Materials Journal*, Vol. 86, No. 2, pp. 175-184

[32] Sack, D. A. & Olson, L. D. (1994): "In-situ Nondestructive Testing of Buried Precast Concrete Pipe", *Infrastructure: New Materials and Methods of Repair, Proceedings of the Materials Engineering Conference*, No 804, ASCE, New York, pp. 499-507

[33] Toutanji, H. (2000): "Ultrasonic Wave Velocity Signal Interpretation of Simulated Concrete Bridge Decks", *Materials & Structures*, Vol. 33, pp. 207-215

[34] Harris, F. J. (1978): "On the Use of Windows for Harmonic Analysis with the Discrete Fourier Transform", *Proceedings of the IEEE*, Vol. 66, No. 1, pp. 51-83

[35] Capon, J. (1969): "High Resolution Frequency-Wavenumber Spectrum Analysis", *Proceedings of the IEEE*, Vol. 57, No. 8, pp. 1408-1418

[36] Hsu, K. and Baggeroer, A. B. (1986): "Application of the Maximum-Likelihood Method (MLM) for Sonic Velocity Logging", *Geophysics*, Vol. 51, No. 3, pp. 780-787

[37] Leverette, S. J.: *Data Adaptive velocity/depth Spectra Estimation in Seismic Wide Angle Reflection Analysis*, PhD Thesis, Joint program in Ocean Engineering, MIT and Woods Hole Oceanographic Institution

[38] Baggeroer, A. B. and Falconer, R. (1982): "Array Refraction Profiles and Crustal Models of the Canada Basin", *Journal of Geophysics Research*, Vol. 87, pp. 5461-5476

[39] Woods, R. D. (1968): "Screening of Surface Waves in Soils", *Journal of Soil Mech. Found. Div.*, Vol. 94, pp. 951-979

[40] Clenshaw, C. W. and Curtis, A. R. (1960): "A Method for Numerical Integration on an Automatic Computer", *Numerical Mathematics*, Vol. 2, pp. 197-205

[41] Xu, P. and Mal, A. K. (1985): "An adaptive Integration Scheme for Irregularly Oscillatory Functions", *Wave Motion*, Vol. 7, pp. 235-243

[42] Kausel, E. and Peek, R. (1982): "Dynamic Loads in the Exterior of a Layered Stratum: an Explicit Solution", *Bulletin of the Seismological Society of America*, Vol. 72, pp. 1459-1481